Optical Variability of the Blazar 2007 + 777

V. S. Bychkova[1], N. S. Kardashev[1], V. V. Vlasyuk[2], and O. I. Spiridonova[2]

[1]*Astro Space Center, Lebedev Physical Institute, ul. Profsoyuznaya 84/32, Moscow, 117997 Russia*
[2]*Special Astrophysical Observatory, Russian Academy of Sciences, pos. Nizhniĭ Arkhyz,*
Karachaĭ-Cherkessia, Russia
Received March 8, 2002; in final form, May 23, 2002

Abstract—We present the results of optical monitoring of the blazar $2007 + 777$ on the 60-cm Zeiss-600 reflector of the Special Astrophysical Observatory of the Russian Academy of Sciences. Light curves in the B and V bands obtained from August 8, 2000, through May 25, 2001, reveal variability with characteristic time scales from 10 to 40 days. © *2003 MAIK "Nauka/Interperiodica".*

1. INTRODUCTION

Variability of extragalactic radio sources was first discovered by Sholomitskiĭ [1, 2]). Since then, radio variations have been observed in many active galactic nuclei. Over the last decade, rapid flux variations have been detected in a number of objects in all observed spectal bands, most of them flat-spectrum quasars and BL Lac objects [3, 4]. The characteristic variation time scales are on the order of a day, but more rapid variations are also observed on time scales of hours or even minutes [3, 5].

Rapid variability in BL Lac objects is observed at gamma-ray energies [6], as well as in the radio and optical [3, 4]. Monitoring reveals variability on long time scales as well [7, 8]. The most rapid variations have been observed on time scales of less than one hour [5]. In the radio, there is sometimes a dependence of the variability amplitude on the observing frequency [9].

Simultaneous radio and optical [10, 11] and optical and γ-ray [3, 12] observations have been carried out in a number of studies. Correlations between radio and optical variability have been detected in several objects. The best studied source for which such correlations have been detected is the blazar S5 0716+714 [11].

Our understanding of the nature of this phenomenon remains incomplete. If the variabiity is due to processes occurring within the object itself, a substantial fraction of its energy is radiated from a small volume (with a diameter less than one light day), requiring extreme conditions in the source. However, variations of the observed flux could also be due to external mechanisms, such as interstellar scattering and microlensing.

Explanations of radio variability of extragalactic radio sources as a consequence of scattering on inhomogeneities in the interstellar plasma have been considered by Rickett [13] and Shapirovskaya [14, 15]. This model can explain much of the observed behavior; however, variability observed at the shortest radio (e.g., millimeter) wavelengths and correlations between radio and optical variations must have another origin [3].

A third mechanism is microlensing by multiple objects close to the line of sight, which gives rise to flux variations and deviations in the apparent position of the source [3]. Distant quasars can be gravitationally lensed not only by galaxies but also by individual stars [16]. The variations in the flux and apparent position of the source depend on the masses, numbers, and motions of the lensing objects and are independent of observing wavelength.

Optical observations could be key to understanding these phenomena, since the presence of optical variability and correlations with variability in the radio would indicate an internal mechanism for rapid variability.

The radio source $2007 + 777$ is a blazar with a virtually lineless optical continuum. Its redshift, $z = 0.342$, was determined from the weak forbidden lines [OIII] $\lambda\lambda$ 4959, 5007 and [OII] λ 3727 [17]. VLBI observations show a multi-component core–jet structure [18–20]. Radio flux variability has been detected at various frequencies [4, 10, 21, 22]. The object has been observed at multiple epochs with X-ray (0.1–3.5 keV) satellites [23–25]; however, no X-ray variability has been detected. Synchronous observations in May 1989 in the radio (6 and 11 cm at time intervals of four hours) and the optical (in the R band at time intervals of the order of a day) over ten days did not
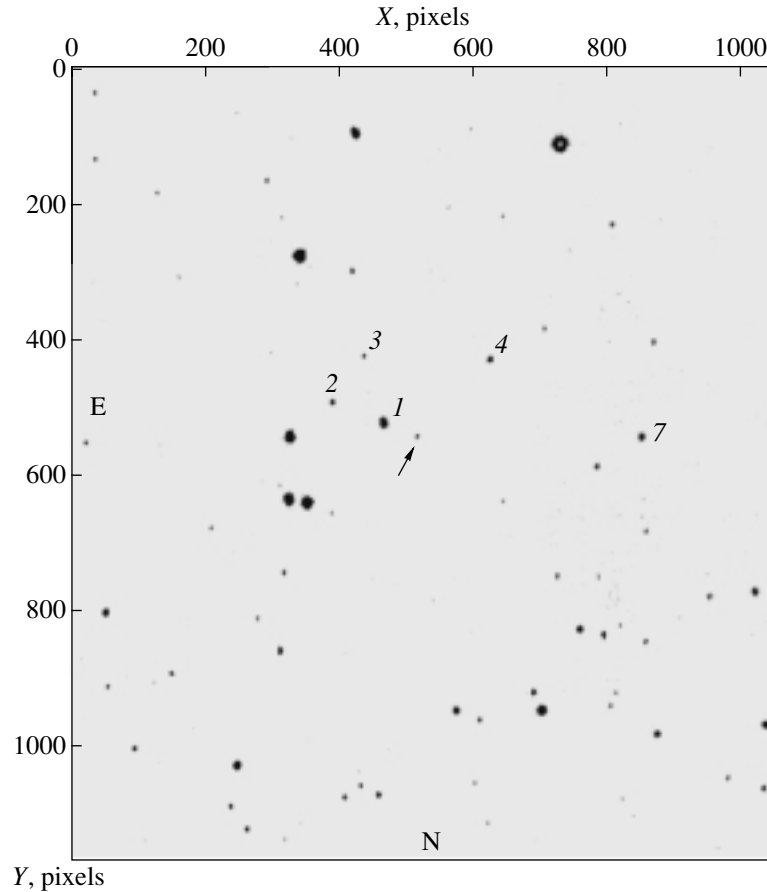
Fig. 1. The vicinity of the blazar $2007 + 777$. Estimates of the magnitudes of the indicated control stars are given in Table 1.

show appreciable variability [22]. Simultaneous observations at several frequencies in the radio, at 11.5, 25, and 60 μm using ISO in the infrared, and in the R band in the optical were obtained over 20 days in 1997 [10]. Weak variability in all bands on time scales exceeding a day was detected.

Long-term optical monitoring observations have not yet been carried out. In 1996, Heidt and Wagner [26] published the results of optical observations of 2007+777 obtained over two nights, which indicated weak variability on time scales exceeding three days.

2. OBSERVATIONS

Our photometric observations of $2007 + 777$ were conducted using an automated photometer with offset guiding mounted at the Cassegrain focus of the 60-cm Zeiss-600 telescope of the Special Astrophysical Observatory of the Russian Academy of Sciences. The photometric complex included a low-noise 1040×1160 CCD detector cooled with liquid nitrogen. The scale of the images was $0.45''$/pixel, with

a field of view of $7.5' \times 8.5'$. The possibility of maintaining the guiding over long times enabled us to obtain direct exposures to 22^m and perform photometry to $18^m - 19^m$, with an accuracy of 0.05^m for $30 - 40$ minute exposures.

We reduced the photometric data using software developed at the Special Astrophysical Observatory by one of the authors [27]. The observations were carried out in the B and R bands from August 2000 through June 2001. The exposure times were $2 - 10$ minutes, and the seeing was $2'' - 3''$. We obtained exposures of the early-morning and twilight skies for the purpose of flat-fielding, as well as bias and dark frames.

Reference standards in the field were identified to enable the acquisition of long series of photometric monitoring data for $2007 + 777$. The photometric standard NGC 7006, which is separated from $2007 + 777$ by a small zenith distance, was exposed successively with $2007 + 777$ in the BVR bands (observation date JD 2451919). The photometric tie was checked by observing the galaxy NGC 7469 with known BVR magnitudes on the same night. The consistency of the measurements within the errors

Table 1. Reference stars in the field of 2007+777: coordinates and BVR magnitudes with their errors

Star number	RA (2000)	Dec (2000)	B Error	V Error	R Error
1	$20^h05^m38.4^s$	$+77°52'33.3''$	14.18 0.01	13.51 0.02	13.18 0.02
2	20 05 49.8	+77 52 21.3	17.25 0.03	16.37 0.02	15.86 0.02
3	20 05 42.9	+77 51 49.1	18.02 0.04	17.03 0.02	16.55 0.02
4	20 05 15.4	+77 51 50.9	16.77 0.01	15.80 0.01	15.23 0.01
7	20 05 43.0	+77 52 42.2	16.16 0.03	15.45 0.03	14.92 0.02

$(0.03^m$ in R and 0.05^m in $B)$ enabled a photometric tie to the reference stars in the field of $2007 + 777$. All the reference objects measured are marked with numbers in the photograph of the field shown in Fig. 1. We selected stars 1, 2, 3, 4, and 7 as the main reference stars near $2007 + 777$. The parameters of these stars are listed in Table 1.

3. ANALYSIS

Our R and B photometric observations were carried out over a period of ten months, on $2-8$ nights each month, with $3-40$ measurements on each night. To search for short-timescale variability (on time scales from 10 min to several hours), we constructed light curves of the target and control stars for the seven nights during which the largest number of observations were made (from 15 to 40 measurements per night).

We estimated the significance of variability using the quantity

$$K = \sigma/\sigma_{\text{mean}},$$

where σ is the rms normal deviation of the observed brightnesses from their mean value for an individual night and σ_{mean} is the mean error in the observed brightnesses. The higher K, the more significant the variability. The results are presented in Table 2.

We found $K \sim 1$ for three of the seven nights we selected, and for one of the nights, $K \sim 1.5$. Probable intraday variability was observed only on January 30, 2001, when $K = 2.4$. There was suspected variability on January 8, 2001 ($K = 1.9$), since individual observations on that night show deviations exceeding 3σ. No short-timescale variability was observed on October 25, 2000.

Figure 2 presents the R light curves for two nights: October 25, 2000, when K was minimum (Fig. 2a) and January 30, 2001, when K was maximum (Fig. 2b). The horizontal axis plots the time in hours. For comparison, we also show fluctuations in the amplitude of control star 3, plotted above the light curve for $2007 + 777$. The vertical bars show the

rms measurement errors $(\pm 1\sigma)$ relative to the mean amplitudes each night for the blazar and control star.

We can see in Fig. 2 that deviations rarely exceed 3σ, suggesting an absence of appreciable variability on short time scales (from 10 min to $3-4$ hours). There was no significant trend over the course of a single observing night. Thus, we detected no significant variability on time scales from 10 min to 3 hours during the period of our observations.

Various attempts to carry out optical monitoring of $2007 + 777$ over several days with time resolutions shorter than a day are described in the literature [10, 22, 26]. Weak variability was detected in one of three cases [26]; however, it was not possible to derive a characteristic time scale for the brightness variations due limitations imposed by the observing conditions and the random character of the observations.

Figure 3 presents the complete B (Fig. 3a) and R (Fig. 3b) light curves of the blazar over the entire period of our observations, from August 8, 2000 through May 25, 2001. The horizontal axis plots the observing dates (JD-2451750). The mean brightness for each night is given. The upper part of each panel shows the corresponding light curve for control star 3, whose brightness was closest to that of $2007 + 777$. For ease of viewing, the control-star magnitudes have been

Table 2. Estimated significance of intraday variability $K = \sigma/\sigma_{\text{mean}}$ on seven nights

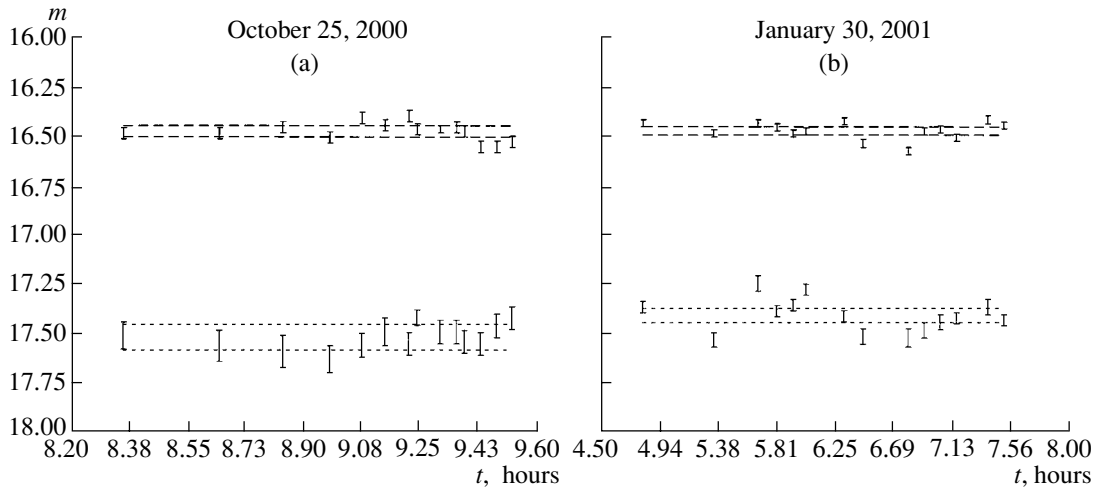| Observing date	K
October 7, 2000	1.1
October 23, 2000	1.1
October 25, 2000	0.9
January 8, 2001	1.9
January 30, 2001	2.4
February 9, 2001	1.5
February 10, 2001	1.8

Fig. 2. Photometric R light curves of the blazar $2007 + 777$ and control star 3 on two nights. The light curves of the blazar are below those of the control star.
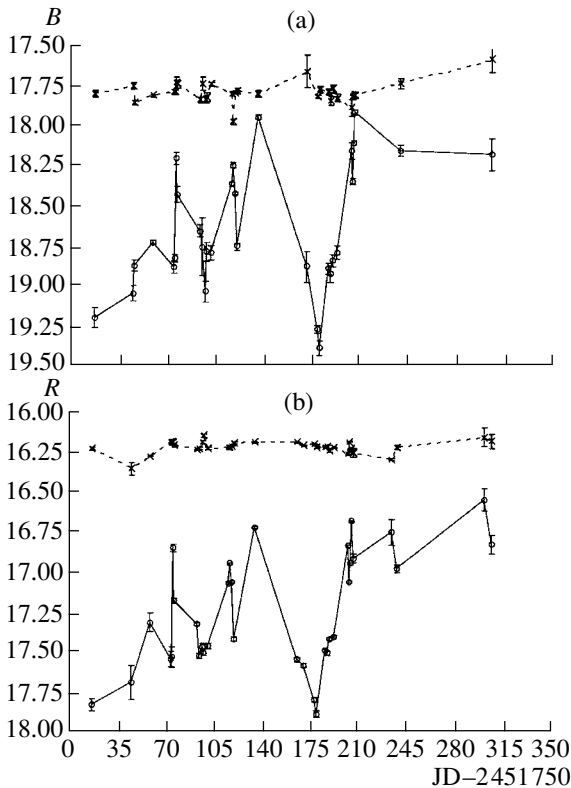

Fig. 3. Light curves of the blazar $2007 + 777$ in the (a) B and (b) R bands over the entire period of our observations (solid lines with points). The dashed lines with crosses in the upper part of each panel show the light curves for control star 3. The figure shows the mean brightnesses for each night.

shifted upward by 0.25^m. We can see brightness variations with amplitudes up to 1.5^m over several dozen nights in Fig. 3. There is a significant correlation between the variations in the B and R bands. On average, the object is 1.5^m brighter in R than in B.

The blazar displays irregular variability, and is usually located near its maximum brightness level. The dips in brightness are Algol-like, with broad, deep decreases with amplitudes of $0.5^m-1.5^m$ lasting $30-40$ days alternating with shallower, narrower decreases with amplitudes less than 0.5^m lasting $10-20$ days. The deepest minimum, corresponding to a brightness decrease by 1.2^m, was observed on JD $2451890-2451960$.

There is a significant trend in the form of a systematic increase in the brightness by, on average, 1^m over the year, indicating long-term variability. The light curve shows that the blazar undergoes long-term variability on time scales exceeding two years, superimposed with more rapid fluctuations on time scales from 10 to 40 days.

A number of blazars have recently been monitored in the optical at several Italian observatories. Detailed R light curves covering several months have been obtained for some of these sources. The light curve of PKS $0422 + 004$ [28] shows Algol-like variability over 150 days, with alternating broad, deep and shallow, narrow dips in brightness. Raiteri *et al.* [29] analyze the optical light curves of eight BL Lac objects, five of which show similar variability on time scales of 100 to 200 days. The best-studied representative of this class of object, S5 $0716 + 714$ [30], also displayed alternating brightness minima over 200 days of observations. This same pattern is observed for another prominent blazar, S4 $0954 + 65$ [31]. The light curves of all these sources show trends that are indicative of long-term variability superimposed with shorter time-scale flares.

4. ACKNOWLEDGMENTS

REFERENCES

1. G. B. Sholomitskiĭ, Astron. Zh. **9**, 516 (1965).
2. G. B. Sholomitskiĭ, Astron. Tsirk., No. 359 (1966).
3. S. J. Wagner and A. Witzel, Ann. Rev. Astron. Astrophys. **33**, 163 (1995).
4. A. Quirrenbach, A. Witzel, T. P. Krichbaum, *et al.*, Astron. Astrophys. **258**, 279 (1992).
5. J. Dennett-Thorpe and A. G. de Bruyn, Astrophys. J. **529**, L65 (2000).
6. C. Von Montigny, D. L. Bertsch, J. Chiang, *et al.*, Astrophys. J. **440**, 525 (1995).
7. G. E. Romero, J. A. Combi, and F. R. Colomb, Astron. Astrophys. **288**, 731 (1994).
8. G. M. Raiteri, M. Villata, H. D. Aller, *et al.*, Astron. Astrophys. **377**, 396 (2001).
9. T. P. Krichbaum, A. Quirrenbach, and A. Witzel, *Variability of Blazars* (Cambridge Univ. Press, Cambridge, 1992), p. 331.
10. B. Peng, A. Kraus, *et al.*, Astron. Astrophys. **353**, 937 (2000).
11. A. Quirrenbach, A. Witzel, S. Wagner, *et al.*, Astrophys. J. **372**, L71 (1991).
12. R. C. Hartman, J. R. Webb, A. P. Marscher, *et al.*, Astrophys. J. **461**, 698 (1996).
13. B. J. Rickett, Ann. Rev. Astron. Astrophys. **28**, 561 (1990).
14. N. Ya. Shapirovskaya, Astron. Zh. **55**, 953 (1978) [Sov. Astron. **22**, 544 (1978)].
15. N. Ya. Shapirovskaya, Pis'ma Astron. Zh. **11**, 686 (1985) [Sov. Astron. Lett. **11**, 289 (1985)].
16. P. Schneider and A. Weiss, Astron. Astrophys. **171**, 49 (1987).
17. M. Stickel, J. N. Fried, and H. Kuhr, Astron. Astrophys., Suppl. Ser. **80**, 103 (1989).
18. A. Eckart, A. Witzel, *et al.*, Astron. Astrophys., Suppl. Ser. **67**, 121 (1987).
19. A. Witzel, C. J. Schalinski, K. J. Johnston, *et al.*, Astron. Astrophys. **206**, 245 (1988).
20. D. C. Gabuzda, C. M. Mullan, T. V. Cawthorne, *et al.*, Astrophys. J. **435**, 140 (1994).
21. D. C. Heeschen, T. Krichbaum, C. J. Schalinski, and A. Witzel, Astron. J. **94**, 1493 (1987).
22. S. Wagner, F. Sánchez-Pons, A. Quirrenbach, and A. Witzel, Astron. Astrophys. **235**, L1 (1990).
23. D. M. Worrall and B. J. Wilkes, Astrophys. J. **360**, 396 (1990).
24. P. Ciliegi, L. Bassani, and E. Caroli, Astrophys. J., Suppl. Ser. **85**, 111 (1993).
25. C. M. Urry, R. M. Sambruna, and D. M. Worrall, *et al.*, Astrophys. J. **463**, 424 (1996).
26. J. Heidt and S. J. Wagner, Astron. Astrophys. **305**, 42 (1996).
27. V. V. Vlasyuk, Astrofiz. Issled., Byull. SAO **36**, 107 (1993).
28. E. Massaro, R. Nesci, M. Maesano, *et al.*, Astron. Astrophys. **314**, 87 (1996).
29. C. M. Raiteri, M. Villata, G. De Francesco, *et al.*, Astron. Astrophys., Suppl. Ser. **132**, 361 (1998).
30. G. Ghisellini, M. Villata, C. M. Raiteri, *et al.*, Astron. Astrophys. **327**, 61 (1997).
31. C. M. Raiteri, M. Villata, G. Tosti, *et al.*, Astron. Astrophys. **352**, 19 (1999).

Translated by D. Gabuzda

Comparison Between Two- and Three-dimensional Modeling of the Structure of an Accretion Disk in a Binary System

M. V. Abakumov, S. I. Mukhin, Yu. P. Popov, and V. M. Chechetkin

Keldysh Institute of Applied Mathematics, Russian Academy of Sciences,
Miusskaya pl. 4, Moscow, 125047 Russia
Received March 10, 2002; in final form, June 26, 2002

Abstract—We compare two- and three-dimensional modeling of gas-dynamical processes in the accretion disk of a binary system. The origin of spiral waves and the loss of the angular momentum related to them are considered. It is concluded that a steady state of the disk cannot exist without taking into account the gas inflow from the donor star. © *2003 MAIK "Nauka/Interperiodica"*.

1. INTRODUCTION

The properties of accretion disks and gaseous formations around gravitating bodies are currently a topical problem in astrophysics. Such formations are especially characteristic of stellar binary systems, where, in many cases, processes in the disk specify the overall evolution of the binary. Particular attention has been given to mechanisms for the loss of angular momentum of the disk and the subsequent accretion, which considerably affect the observed radiation.

Along with analytical methods, mathematical modeling based on various physical models and computational procedures is currently widely used to study processes in accretion disks. For example, the computations carried out in [1−3] indicated the presence of spiral formations in the accretion disk of a binary system, interpreted as shock waves. It was suggested that these formations represent an important mechanism for the loss of angular momentum by the disk material.

The formation of the disk structure is modeled in [4−6], taking into account the mass transfer between the binary components. In these studies, the computational domain includes both binary components, so that a fairly small number of cells of the differential grid fall near the accreting star, where the disk is formed. For this reason, it is difficult to use these computations to resolve details of the spatial structure of the flows in the disk.

In [3, 7], the accretion disk is set aside as a separate element. In this case, it is possible to study in detail spatial formations in the disk originating under the action of the gravitational forces of both components and the rotation of the binary as a whole.

In our previous study [7], we carried out mathematical modeling of the processes in the accretion disk of a binary using a two-dimensional spatial approximation. The main subjects of the study were the possible existence of a steady state of the disk under the considered conditions, the disk's spatial structure, and mechanisms for the loss of angular momentum by the disk. We emphasized the selection of the initial state of the disk, which was assumed to be in equilibrium in the absence of the secondary. In this case, processes developing in the disk are due only to the rotation of the binary and the tidal influence of the gravitation of the secondary. In the computations, we varied the component mass ratio, form of the boundary conditions, and initial equilibrium configuration of the disk. To increase the reliability of the results and, in particular, to verify the viscosity patterns, we carried out the calculations using two different numerical methods: a modified Roe scheme [8] and the method of large particles [9].

Here, we continue our mathematical modeling of processes in an accretion disk begun in [7] in a three-dimensional approximation. In some astrophysical problems related to binaries, the performance of three-dimensional calculations reveals the formation of gas-dynamical flows that differ from those for the two-dimensional case both quantitatively and qualitatively [13]. Therefore, the prime objective of our study was to compare the results of the two-dimensional and three-dimensional computations, in order to evaluate the adequacy of the two-dimensional approach for the problem at hand.

2. THE MATHEMATICAL MODEL

We consider a system consisting of two stars with masses M and m rotating about the center of mass of the system with a constant angular velocity ω. Further, we call the star with mass M the primary
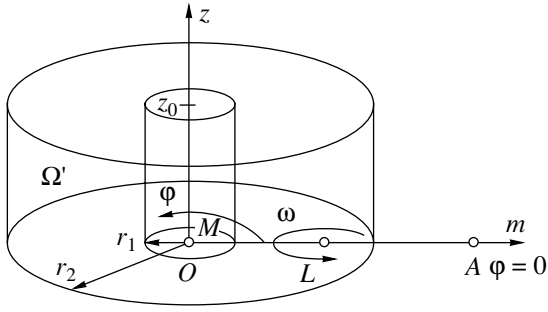
Fig. 1. The domain of the computations.

and the star with mass m the secondary, or donor, star (Fig. 1).

According to Kepler's third law, the distance A between the components is related to the angular velocity of the rotation of the system by the expression

$$\omega^2 A^3 = G(M + m), \qquad (2.1)$$

where G is the gravitational constant. The distance L between the primary and center of mass of the system is

$$L = Am/(M + m). \qquad (2.2)$$

We introduce a noninertial cylindrical coordinate system (r, φ, z) rotating with angular velocity ω, with its origin coinciding with the center of the primary and the $\varphi = 0$ axis passing through the secondary (Fig. 1).

We solve the problem within the domain $\Omega = (r_1 \le r \le r_2) \times (0 \le \varphi \le 2\pi) \times (-z_0 \le z \le z_0)$, which is essentially the space between two coaxial cylinders whose axis of rotation coincides with the z axis. The self-gravitation of the gas is not taken into account, since the mass of gas in the disk is assumed to be substantially smaller than the mass of the primary. The gas is compressible and ideal and is described by the system of three-dimensional gas-dynamical equations in Euler variables [10]

$$\frac{\partial(r\rho)}{\partial t} + \frac{\partial(r\rho u)}{\partial r} + \frac{1}{r}\frac{\partial(r\rho v)}{\partial \varphi} + \frac{\partial(r\rho w)}{\partial z} = 0, \quad (2.3)$$

$$\frac{\partial(r\rho u)}{\partial t} + \frac{\partial(r\rho u^2 + rp)}{\partial r} + \frac{1}{r}\frac{\partial(r\rho uv)}{\partial \varphi}$$

$$+ \frac{\partial(r\rho uw)}{\partial z} = p + \rho v^2 + r\rho \mathbf{F}_r,$$

$$\frac{\partial(r\rho v)}{\partial t} + \frac{\partial(r\rho vu)}{\partial r} + \frac{1}{r}\frac{\partial(r\rho v^2 + rp)}{\partial \varphi}$$

$$+ \frac{\partial(r\rho vw)}{\partial z} = -\rho uv + r\rho \mathbf{F}_\varphi,$$

$$\frac{\partial(r\rho w)}{\partial t} + \frac{\partial(r\rho wu)}{\partial r} + \frac{1}{r}\frac{\partial(r\rho wv)}{\partial \varphi}$$

$$+ \frac{\partial(r\rho w^2 + rp)}{\partial z} = r\rho \mathbf{F}_z,$$

$$\frac{\partial(r\rho e)}{\partial t} + \frac{\partial(r\rho uh)}{\partial r} + \frac{1}{r}\frac{\partial(r\rho vh)}{\partial \varphi}$$

$$+ \frac{\partial(r\rho wh)}{\partial z} = r\rho(\mathbf{F}, \mathbf{v}),$$

$$e = \varepsilon + u^2/2 + v^2/2 + w^2/2, \quad h = e + p/\rho$$

with the equation of state

$$p = (\gamma - 1)\rho\varepsilon.$$

Here, r is the radius, φ is the polar angle, t is time, ρ is the gas density, p is the pressure, ε is the specific internal energy, e is the total specific energy, γ is the adiabatic index, h is the total specific enthalpy, $\mathbf{v} = (u, v, w)^T$ is the gas velocity (with u, v, and w being the radial, azimuthal, and z components), and $\mathbf{F}$ is the total specific external force on a gas particle, with its components being $(\mathbf{F}_r, \mathbf{F}_\varphi, \mathbf{F}_z)$.

In dimensionless variables, the scaling factors were chosen as follows:

$$M = 10^{33} \text{ g}, \quad R = 7 \times 10^8 \text{ cm},$$

$$G = 6.67 \times 10^{-8} \text{ cm}^3\text{g}^{-1}\text{s}^{-2}.$$

With these variables, the components of the external force, which include the gravitational forces of both the primary and secondary, the centrifugal force, and the Coriolis force, are

$$\mathbf{F}_r = -\frac{r}{(r^2 + z^2)^{3/2}} \qquad (2.5)$$

$$+ \frac{md}{(d^2 + z^2)^{3/2}}\cos(\alpha + \varphi) - \omega^2 s\cos(\eta + \varphi) + 2\omega v,$$

$$\mathbf{F}_\varphi = -\frac{md}{(d^2 + z^2)^{3/2}}\sin(\alpha + \varphi)$$

$$+ \omega^2 s\sin(\eta + \varphi) - 2\omega u,$$

$$\mathbf{F}_z = -\frac{z}{(r^2 + z^2)^{3/2}} - \frac{mz}{(d^2 + z^2)^{3/2}},$$

$$d = \sqrt{r^2 + A^2 - 2Ar\cos\varphi}, \quad \sin\alpha = r\sin\varphi/d,$$

$$\cos\alpha = (A - r\cos\varphi)/d,$$

$$s = \sqrt{r^2 + L^2 - 2rL\cos\varphi}, \quad \sin\eta = r\sin\varphi/s,$$

$$\cos\eta = (L - r\cos\varphi)/s.$$

In the chosen coordinate system, the expressions for the forces do not depend on the solution or thereby, on the time, with the exception of the last term (containing the velocity), related to the Coriolis force.

As the initial data in the computations described below, we specified a steady-state gaseous configuration (in the absence of the secondary). This enabled us to exclude the influence of gas-dynamical processes due to the nonequilibrium nature of the initial state of
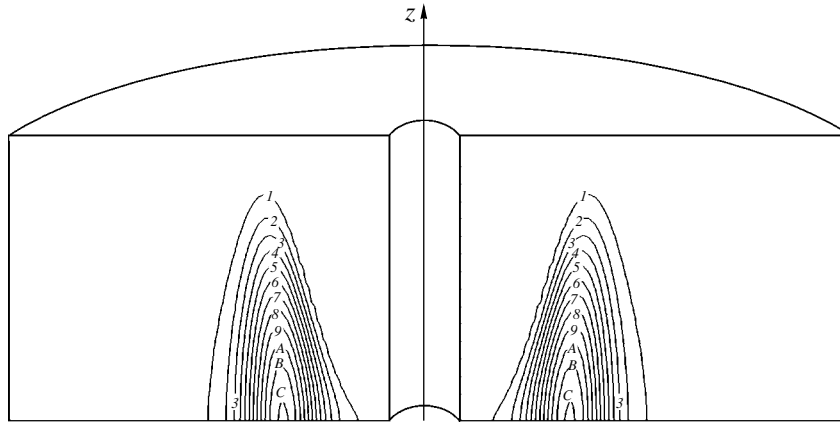
Fig. 2. The initial configuration of the disk: lines of equal density in the $\varphi = 0$ and $\varphi = \pi$ planes.
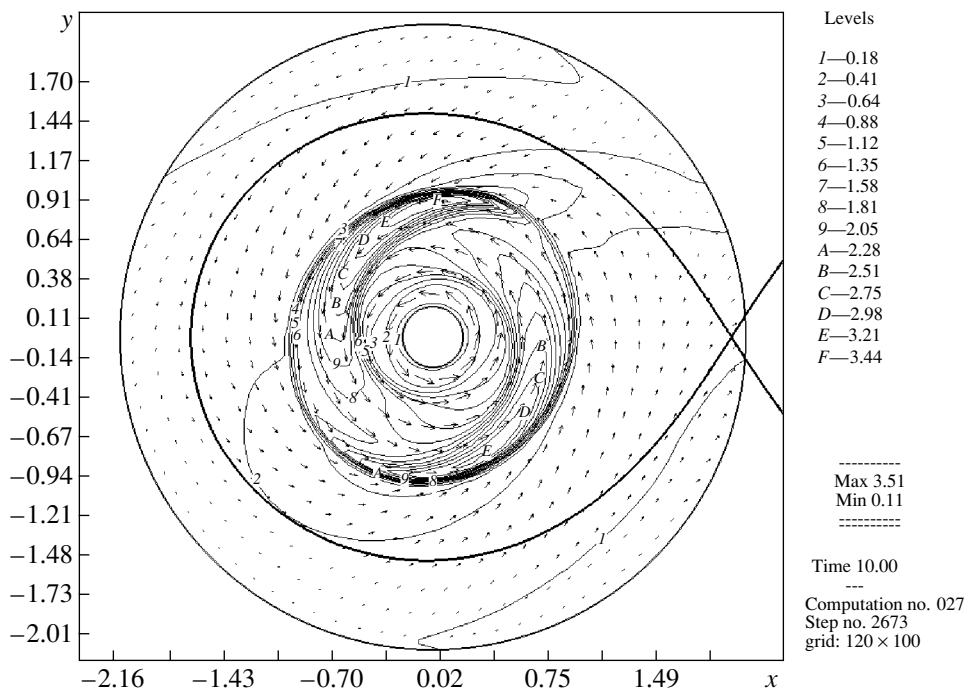

Fig. 3. Formation of spiral structure in a two-dimensional computation of the lines of equal density and velocity vectors.

the disk. In [11], we studied in detail possible equilibrium, cylindrically symmetrical configurations for gas rotating in the vicinity of a gravitating center whose pressure and density are related by the polytropic equation

$$p = k\rho^{\gamma}, \qquad k, \gamma = \text{const.}$$

In particular, we considered a class of equilibrium gas configurations with the boundary in the form

$$Z(r) = \pm\alpha r \exp(-\beta(r - r_0)^2) \qquad (\alpha,\ \beta,\ r_0 > 0) \tag{2.6}$$

and present formulas for equilibrium distributions of

functions of the velocity $v_{\varphi}(r, z)$ and density $\rho(r, z)$ of the gas.

Since the computations were carried out in dimensionless variables, the characteristic parameters of the gas in the disk are specified by scaling factors. For example, for the selected scaling factors, the characteristic gas temperature in the disk is of the order of 10^6 K.

In the described basic version of the computations, the distance between the binary components was taken to be $A = 4$, and the mass of the secondary, to be $m = 1$. One complete revolution of the binary occupies $T_s \approx 35$. The gas was assumed to be ideal,
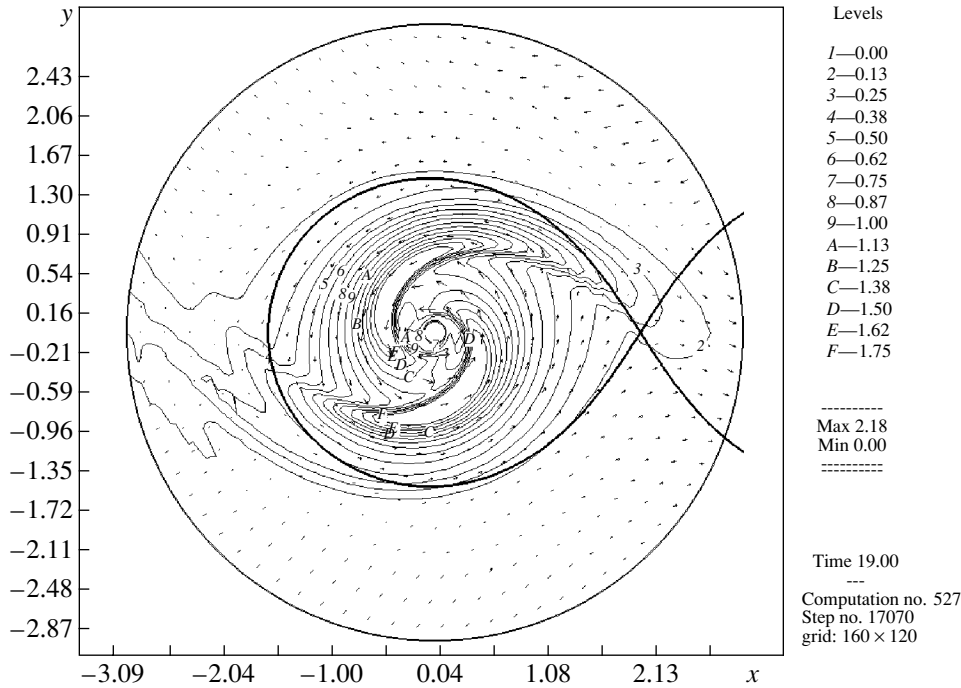
Fig. 4. Spiral structure of the disk in a two-dimensional computation of the lines of equal density and velocity vectors.

with the equation of state (2.4) and an adiabatic index $\gamma = 5/3$.

The parameters in (2.6) specifying the initial equilibrium configuration of the disk were taken to be $\alpha = 0.2$, $\beta = 9$, and $r_0 = 0.8$. With these parameters, the bulk of the gas mass is concentrated within the cylindrical region $0.5 < r < 1.1$, $-0.2 \leq z \leq 0.2$; the total mass of the disk is $M_{gas} \approx 0.1$, and one complete revolution of a gas particle in the equilibrium configuration occupies $T_1 \approx 0.6$ and $T_2 \approx 10$ at the inner and the outer edges of the disk, respectively (Fig. 2).

Due to the symmetry of the problem relative to the $z = 0$ plane, the computations were carried out within the domain $\Omega' = (r_1 \leq r \leq r_2) \times (0 \leq \varphi \leq 2\pi) \times (0 \leq z \leq z_0)$ (Fig. 1), with appropriate selection of the boundary conditions at the "bottom" boundary of the domain. On the remaining boundaries, we specified free boundary conditions of the form

$$\partial f / \partial r = 0 \quad (\partial f / \partial z = 0), \quad \text{where } f = r, u, v, w, e, \tag{2.7}$$

or the nonleakage condition

$$u = 0 (w = 0). \tag{2.8}$$

Depending on the version of the computations, the parameters of the domain were taken to be $r_1 = 0.2$, $r_2 = 1.4$ or $r_1 = 0.2$, $r_2 = 2.1$, with z_0 varied from 0.2 to 1. In the three-dimensional computations, the differential grid was made up of from $60 \times 40 \times 30$ to $120 \times 80 \times 60$ cells.

3. RESULTS OF TWO-DIMENSIONAL NUMERICAL COMPUTATIONS

Let us first briefly describe the results of the mathematical modeling of the processes in the disk obtained in [7] for the two-dimensional case. The system of equations is reduced from (2.3), (2.5) under the assumption that $v_z = 0$, $z = 0$, $\partial / \partial z = 0$ and is solved within an annulus with the radii r_1, r_2. The initial data are obtained from a three-dimensional configuration of the form (2.6) by averaging over z [11].

The calculations revealed certain general stages of the processes in the accretion disk. In the initial stage, the system of equations (2.3), (2.4) was solved in the absence of a secondary ($m = 0$). In this case, the initial equilibrium state of the gas (2.6) remains essentially unchanged, confirming its stationarity and indicating its stability. Further, to avoid sharp relaxation processes, the distance between the components was varied linearly from $10^3 A$ to A over a fairly short time interval $T_A = 4.5$. The system parameters and specific external force were varied in accordance with (2.1), (2.2), and (2.5). At this stage, the initial state of the gas in the disk also changed insignificantly.

In the next stage, under the action of the external-force field **F** and the gas kinetic-pressure force, the gas gradually acquires a positive radial component to its velocity, as a result of which a shock wave propagating in the peripheral zone of the computation
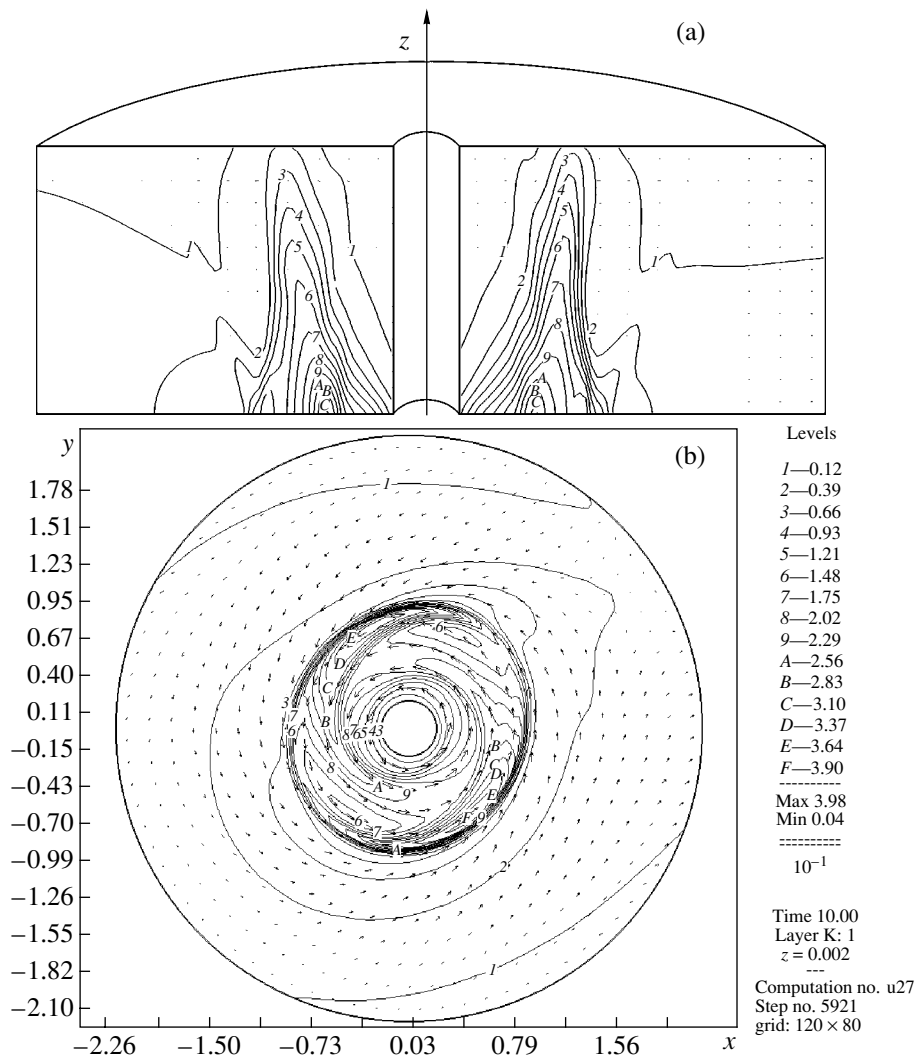
Fig. 5. Formation of spiral structure in the three-dimensional computations: lines of equal density and velocity vectors in the (a) $\varphi = 0$ and $\varphi = \pi$ planes and (b) in the $z = 0$ plane.

domain is formed. The shock front assumes an ellipsoidal shape, due to the polar-angle inhomogeneity of the components of the combined "perturbing" force (Fig. 3). At the same time, as occurs in a point explosion, a backflow of gas arises inside the rarefied zone. The figures present lines of equal density and velocity vectors of the gas.

On its way through the shock front, the gas virtually completely loses its radial velocity component. As a result, a new quasisteady state is formed behind the shock front, with spiral waves being an important element (Fig. 4; see also Fig. 6). This configuration remains qualitatively unchanged over times of the order of the rotational period of the binary, $T_s \approx 35$.

To analyze the spiral disk structures that form, we made a supplementary computation for the gas-particle trajectories. The transition of a particle through the spiral-wave front can result in either a decrease or increase of its angular momentum; in the latter case, the particle will move toward the outer edge of the disk. Based on this, we concluded that the accretion depends not only on the presence of the spiral waves but also on the overall superposition of the forces, including the pressure gradient.

The computations indicated that the described stages of formation of the spiral structure do not depend qualitatively on the component mass ratio or on the chosen initial configuration for the disk. Differences occur only in the time of formation of the spiral structures, their intensity, and the duration of the phase of quasisteady-state flow.

One of the aims of the modeling was to investigate the possibility of a steady state of the accretion disk in a binary. For this purpose, we carried out a set of computations within a region containing the Roche lobe of the primary and the Lagrange point L_1. In
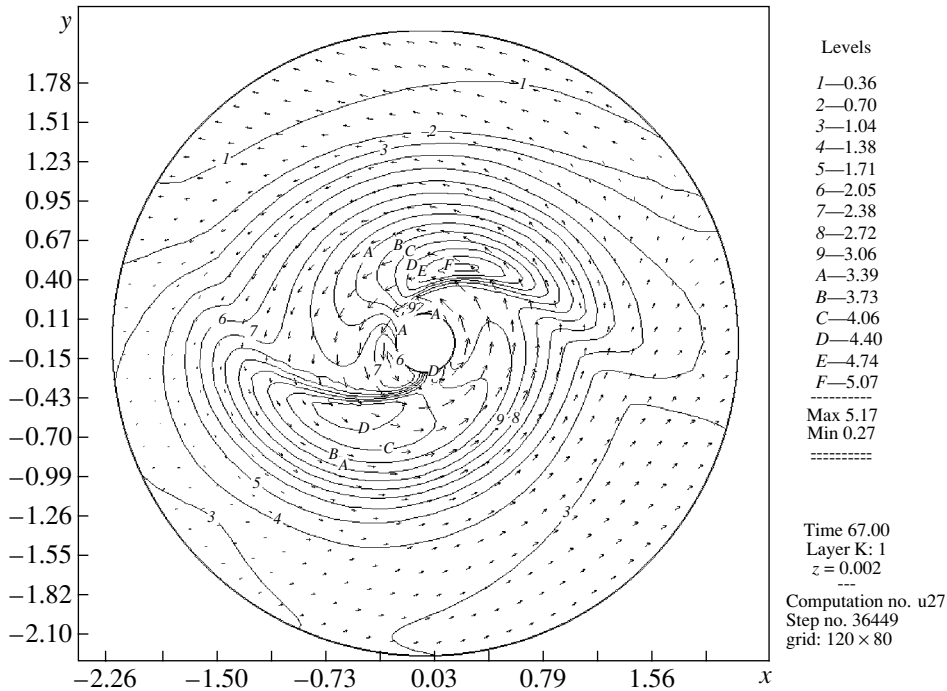
Fig. 6. Spiral structure of the disk in the three-dimensional computations: lines of equal density and velocity vectors in the $z = 0$ plane.

the case of the free boundary conditions (2.7), a two-arm spiral structure is established in the disk (Fig. 4), which remains qualitatively unchanged during an extended period on the order of $12T_s$. However, this structure is not steady-state, since the disk material flows outward both toward the inner boundary of the region (onto the primary) and toward the periphery of the region, primarily in the vicinity of the inner Lagrange point. The intensity of the spiral waves and the shape of the wave fronts vary with time.

Formally, a steady-state configuration of the disk can be obtained by selecting the nonleakage condition (2.8), avoiding the outflow of matter from the disk. In this case, a disk structure with spiral waves also forms; the very presence of such waves under these conditions casts some doubt on whether they are formed by shocks. The problem of the nature of these spiral waves has been studied in more detail in [12].

4. RESULTS OF THE THREE-DIMENSIONAL NUMERICAL COMPUTATIONS

Numerous studies (see, for example, [13]) note that substantial differences can appear between the results of two-dimensional and three-dimensional mathematical modeling in astrophysics. For this reason, it was important to carry out three-dimensional modeling of the processes in an accretion disk that

were completely analogous to the two-dimensional computations described above.

The same stages of evolution of the spiral disk structure are visible in the three-dimensional modeling as in the two-dimension case. Let us illustrate these stages using the example of the computations for equal masses of the secondary and primary ($m = 1$) and with the following parameters for the computation domain, which contains the Roche lobe of the primary and the Lagrange point L_1: $r_1 = 0.2$, $r_2 = 2.2$, and $z_0 = 0.2$. The differential grid used for these computations was made up of $120 \times 80 \times 60$ cells in the coordinates r, φ, and z.

We specified as the initial state of the gas the same equilibrium configuration in the absence of the secondary of the form (2.6), with $\alpha = 0.2$, $\beta = 9$, and $r_0 = 0.8$. For these parameters, the gas density differs from zero only in the part of the computation domain specified by the boundary equation (2.6). In accordance with the requirements of the computation technique, the "background" density and pressure in the rest of the domain were specified to be $\rho_b \approx 1 \times 10^{-6}$, $p_b \approx 1 \times 10^{-7}$, whereas the density and pressure in the equilibrium configuration were $\rho_0 \approx 1 \times 10^{-1}$, $p_0 \approx 1 \times 10^{-3}$, respectively. Free boundary conditions (2.7) were specified on the "lateral" boundaries of the computation domain while the nonleakage condition (2.8) was specified at the "upper" boundary, and conditions ensuring symmetry of
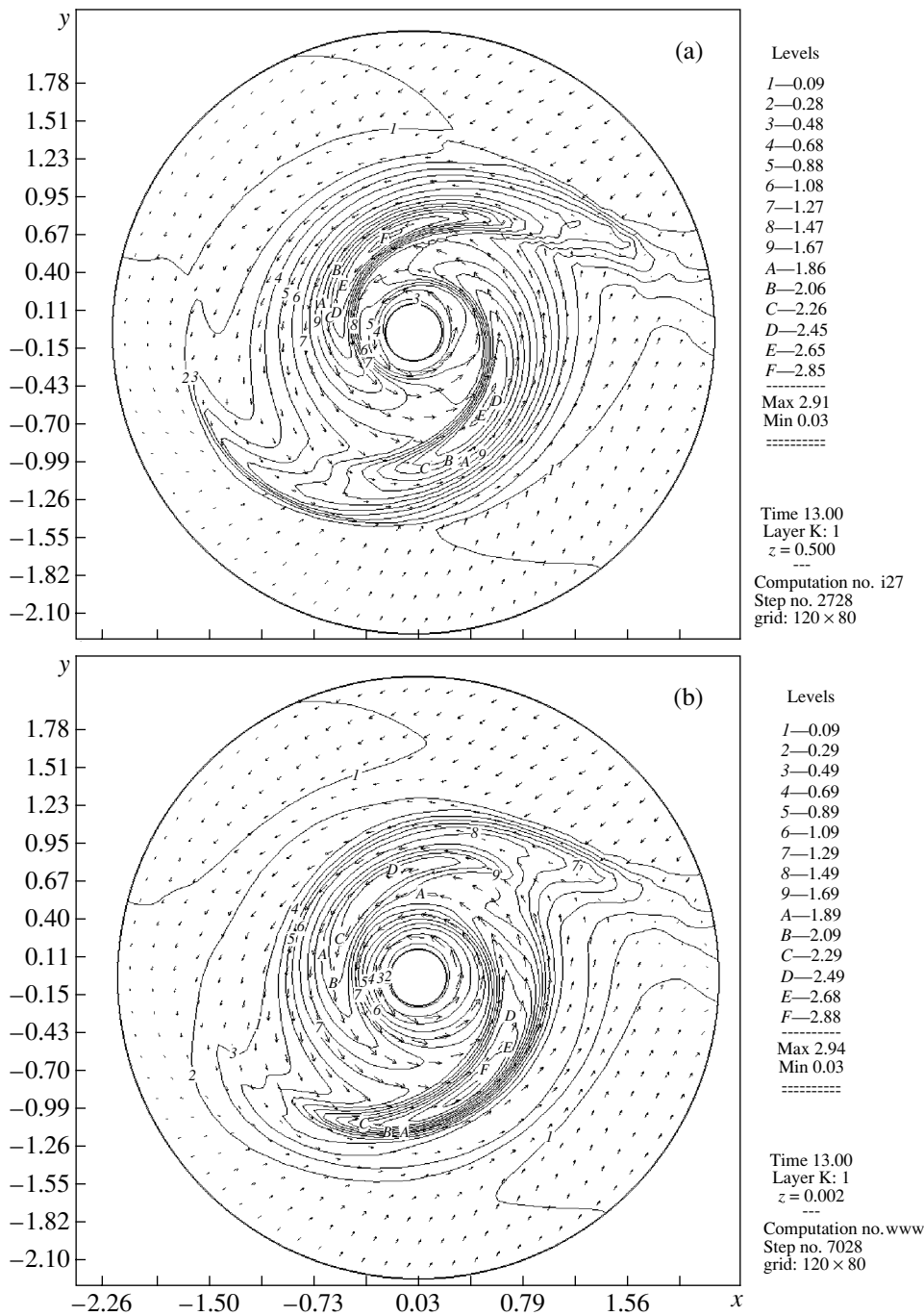
Fig. 7. (a) Spiral structure of the disk for the two-dimensional computations and (b) the averaged spiral structure of the disk for the three-dimensional calculations at the same moment in time. Lines of equal density and velocity vectors are shown.

the flow about the $z = 0$ plane were specified at the "lower" boundary, as was noted in Section 2.

As in the two-dimensional approximation, the action of external forces on a gas particle, specified by the conditions (2.1), (2.2), and (2.5), was gradually increased to the calculated value by linearly decreasing the distance between the components from $10^3 A$ to A over a time $T_A = 4.5$. The initial configuration

varies insignificantly over this time, confirming its equilibrium nature.

In the next stage, a radial shock is formed and propagates toward the periphery of the computation domain, gradually assuming an ellipsoidal shape due to the polar-angle inhomogeneity of the external force field (2.5). Behind the radial wave front, a new disk core is formed containing two pronounced spiral

structures. Note that the radial component of the gas velocity in the incipient core, as well as the z component, are negligible compared to the azimuthal (rotational) component. In this sense, the gas flow in the disk core can be considered quasisteady. Figures 5a and 5b illustrate these processes. They present lines of equal density and gas-velocity vectors in the $\varphi = 0$ ($\varphi = \pi$) and $z = 0$ planes of the computation domain, respectively.

The spiral structure of the disk is established after the radial wave leaves the computation domain and is similar to that observed in the two-dimensional modeling in the cross sections for fixed z. This structure of the disk does not vary qualitatively on time intervals from T_s to $2T_s$ (Fig. 6), depending on the version of the computations. In this sense, the observed flow can still be considered a quasiequilibrium configuration of the disk in the external force field specified by (2.5).

Thus, we note qualitative similarities between the two-dimensional and three-dimensional modeling at the stage of the formation of the quasiequilibrium spiral structure in the accretion disk. Since a quantitative comparison was also of interest, we compared the flow patterns for the same moment in time in the two-dimensional and three-dimensional computations. To this end, we averaged the three-dimensional configuration by integrating over the variable z and then represented the result in the form of density contours and velocity vectors within a two-dimensional ring-shaped domain in the same way as for the two-dimensional configuration. We can see from Fig. 7 that there is also a quantitative similarity between the results, since the corresponding contours refer to approximately the same density levels.

Note that the spiral structure resulting from the three-dimensional modeling is still non-steady-state, due to the fact that either inflow or outflow of the gas through the lateral boundaries of the computation domain can be allowed by the free boundary conditions (2.7). For this reason, the disk material flowing outward primarily in the vicinity of the Lagrange point L$_1$ leaves the computation domain, decreasing the mass of the disk and affecting the shape of the spiral waves. The conditions in the upper boundary of the computation domain also appreciably affect the flow. This represents an additional difference between the three-dimensional and two-dimensional computations, since there simply is no upper boundary in the latter. If free conditions are set at the upper boundary of the domain, the computations may indicate a fictitious inflow of mass through that boundary. The reason is that the $\mathbf{F}_z$ component of the external force specified by (2.5) has a fixed sign and specifies the direction of the force vector toward the equatorial plane $z = 0$. However, since the $\mathbf{F}_z$ component of the external force is inversely proportional to z^2, we

can chose a distance z_0 from the $z = 0$ plane to the upper boundary of the computation domain, as well as values for the background density and pressure ρ_b and p_b, such that any significant impact of this effect on the flow in the disk will be avoided.

Thus, the three-dimensional modeling likewise does not yield a steady-state configuration of the accretion disk in the considered formulation of the problem. As in the two-dimensional case, the mechanism for mass transfer between the accretion disk and the binary envelope in many respects specifies the processes occurring in the disk. In the simplest case, the total absence of mass transfer between the envelope and disk can be specified by specifying nonleakage conditions at all boundaries of the domain (2.8). In this case (in the same way as in the two-dimensional modeling), a steady-state flow with spiral waves can be obtained in the disk, though these waves are to some extent artificial.

5. CONCLUSION

We have compared mathematical modeling of processes in the accretion disk of a binary system in two-dimensional and three-dimensional approximations. Our comparison indicates that the three-dimensional and two-dimensional computations yield very similar results in our formulation of the problem, testifying to the adequacy of the two-dimensional approach.

It is interesting that the three-dimensional and two-dimensional computations differ in studies that include mass transfer in the binary, with the process of accretion taken into account; their results coincide only for γ close to unity [13].

We conclude that the gas-dynamical processes in the disk are specified by a complex force field, which results in the formation of spiral structures with enhanced density and pressure. However, without explicitly taking into account the mechanisms for mass transfer between the accretion disk and binary envelope, it is not possible to obtain a steady-state disk structure in our mathematical model. In order to describe the steady state of the disk, it is necessary to take into account the inflow of matter from the donor star, for example, in a more complete formulation of the problem [5, 6, 13].

6. ACKNOWLEDGMENTS

REFERENCES

1. K. Sawada, N. Sekino, K. Sawada, and E. Shima, KEK Progress Report **89**, 197 (1990).
2. D. Molteni, G. Belvedere, and G. Lanzfame, Mon. Not. R. Astron. Soc. **249**, 748 (1991).
3. T. Matsuda, N. Sekino, E. Shima, *et al.*, Astron. Astrophys. **235**, 211 (1990).
4. D. V. Bisikalo, A. A. Boyarchuk, O. A. Kuznetsov, *et al.*, Astron. Zh. **72** (2), 190 (1995) [Astron. Rep. **39**, 167 (1995)].
5. D. V. Bisikalo, A. A. Boyarchuk, O. A. Kuznetsov, and V. M. Chechetkin, Astron. Zh. **74** (6), 880 (1997) [Astron. Rep. **41**, 786 (1997)].
6. D. V. Bisikalo, A. A. Boyarchuk, O. A. Kuznetsov, and V. M. Chechetkin, Astron. Zh. **74** (6), 889 (1997) [Astron. Rep. **41**, 794 (1997)].
7. M. V. Abakumov, S. I. Mukhin, Yu. P. Popov, and V. M. Chechetkin, Astron. Zh. **78** (6), 505 (2001) [Astron. Rep. **45**, 434 (2001)].
8. P. L. Roe, Ann. Rev. Fluid Mech. **18**, 337 (1986).
9. O. M. Belotserkovskiĭ and Yu. M. Davydov, *The Method of Large Particles in Gas Dynamics* [in Russian] (Nauka, Moscow, 1982).
10. L. D. Landau and E. M. Lifshitz, *Course of Theoretical Physics,* Vol. 6: *Fluid Mechanics* (Nauka, Moscow, 1986; Pergamon, New York, 1987).
11. M. V. Abakumov, S. I. Mukhin, Yu. P. Popov, and V. M. Chechetkin, Astron. Zh. **73** (3), 407 (1996) [Astron. Rep. **40**, 366 (1996)].
12. M. V. Abakumov, S. I. Mukhin, and Yu. P. Popov, Mat. Model. **12**, 110 (2000).
13. D. V. Bisikalo, A. A. Boyarchuk, O. A. Kuznetsov, *et al.*, Astron. Zh. **76** (12), 905 (1999) [Astron. Rep. **43**, 797 (1999)].

Translated by K. Maslennikov

The Evolution of GRS 1915+105—an X-ray Binary with a Black Hole

A. V. Tutukov[1], A. V. Fedorova[1], and A. M. Cherepashchuk[2]

[1] *Institute of Astronomy, Russian Academy of Sciences, ul. Pyatnitskaya 48, Moscow, 109017 Russia*
[2] *Sternberg Astronomical Institute, Universitetskiĭ pr. 13, Moscow, 119899 Russia*
Received March 15, 2002; in final form, May 23, 2002

Abstract—A brief review of the observed parameters of binary systems with black holes is presented. We discuss in detail the evolutionary status of the X-ray binary GRS 1915+105, which contains a massive black hole. Numerical simulations of the evolution of GRS 1915+105 at the X-ray stage indicate that the most probable initial mass of the optical component (donor star) is $(1.5-3)\ M_\odot$. Two possible scenarios are suggested for the evolution of the system prior to the formation of the black hole. If the initial mass of the optical component was $(2.5-3)\ M_\odot$, the system underwent a common-envelope phase; in this case, the initial mass of the black hole progenitor did not exceed $\sim 50\ M_\odot$. If the initial mass of the donor was $(1.5-2.5)\ M_\odot$, a scenario without a common envelope is possible, with the initial mass of the black hole progenitor being smaller than $\sim 50\ M_\odot$. The lack of information about the initial mass-ratio distribution for binary components for small q and the uncertainty of the system parameters make it impossible to give preference to a particular scenario for the system's prior evolution. © *2003 MAIK "Nauka/Interperiodica"*.

1. INTRODUCTION

The possibility of observing black holes (BHs) was predicted in 1964 by Zeldovich [1] and Salpeter [2], who showed that nonspherical accretion onto a BH causes a release of about 10% of the BH's rest energy, which is a huge amount of energy. Further development of the theory of disk accretion onto relativistic objects [3–6] and progress in X-ray astrophysics [7] and optical studies of X-ray binaries [8–14] has resulted in the discovery of numerous BHs in X-ray binaries (see, for example, the recent reviews [15, 16] and references therein).

Currently, masses have been derived for 15 BHs in close binaries: three of these objects belong to massive X-ray binaries with OB stars as the BH companions and 12 to low-mass transient X-ray binaries (X-ray novae). Progress in observations of BHs in close binaries necessitates clarification of the evolutionary status of these systems [17–19]. Here, we will analyze the observational data and basic evolutionary parameters of known X-ray binaries with BHs. We will also consider the formation of the X-ray binary GRS 1915+105.

2. CHARACTERISTICS OF X-RAY BINARIES WITH BLACK HOLES

Table 1 presents the characteristics of known X-ray binaries with BHs [20]. For three of these (SAX J1819.3−2525, XTE 1118+480, GRS 1915+ 105), the masses were estimated only very recently [21–23].

Orosz *et al.* [21] determined the component masses for the transient X-ray binary SAX J1819.3− 2525 (V4641 Sgr); apparent superluminal motions of components in the radio jets of this system have been observed during X-ray flares. This object was discovered as a transient X-ray source [24–26] and was identified with the optical variable star V4641 Sgr, which had been studied by Goranskiĭ [27, 28]. Its orbital period $P = 2^{\text{d}}817$ was determined from spectroscopic observations [21]. The optical light curve forms a double wave with amplitude $\sim 0^{\text{m}}5$, which indicates that the optical star−donor is ellipsoidal and probably fills its Roche lobe. No X-ray eclipses have been observed in this binary. These data can be used to estimate the orbital inclination with reasonable confidence: $60° < i < 71°$. The effective temperature of the donor is $10\,500 \pm 200$ K, and its equatorial velocity of rotation is $V \sin i = 123 \pm 4$ km/s. The component mass ratio, derived assuming that the axial and orbital rotation are synchronous, is $M_X/M_V = 1.50 \pm 0.08$. The spectral type of the optical star is close to B9III. The large distance to this system and the substantial velocities of radio features in the plane of the sky correspond to apparent velocities that exceed the speed of light by a factor of 9.5. As was the case for the X-ray nova GRO J1655−40 [29], the spectrum of the optical star exhibits abundances for α-process elements (oxygen, calcium, magnesium, and titan) that exceed the solar values by factors of $(2-10)$. These elements are formed in the α process in the deep interiors of massive stars. This provides evidence

Table 1. Parameters of binary systems with black holes

System	Spectrum of the optical star	P, days	$f_V(m)$, $M_\odot$	M_X, $M_\odot$	M_V, $M_\odot$	V_{pec}, km/s	Type of X-ray source
Cyg X-1 (V1357 Cyg)	O9.7 Iab	5.6	0.24 ± 0.01	16 ± 5	33 ± 9	2.4 ± 1.2	Stationary
LMC X-3	B3 Ve	1.7	2.3 ± 0.3	9 ± 2	6 ± 2	$-$	Stationary
LMC X-1	O(7-9)III	4.2	0.14 ± 0.05	7 ± 3	22 ± 4	$-$	Stationary
A0620-00 (V616 Mon)	K5 V	0.3	2.91 ± 0.08	10 ± 5	0.6 ± 0.1	-15 ± 5	Transient
GS 2023+338 (V404 Cyg)	K0 IV	6.5	6.08 ± 0.06	12 ± 2	0.7 ± 0.1	8.5 ± 2.2	Transient
GRS 1124−68 (GU Mus)	K2 V	0.4	3.01 ± 0.15	$6(+5-2)$	0.8 ± 0.1	26 ± 5	Transient
GS 2000+25 (QZ Vul)	K5 V	0.3	4.97 ± 0.10	10 ± 4	0.5 ± 0.1	$-$	Transient
GRO J0422+32 (V518 Per)	M2 V	0.2	1.13 ± 0.09	10 ± 5	0.4 ± 0.1	$-$	Transient
GRO J1655−40 (XN Sco 1994)	F5IV	2.6	2.73 ± 0.09	7 ± 1	2.5 ± 0.8	-114 ± 19	Transient
H 1705−250 (V2107 Oph)	K5 V	0.5	4.86 ± 0.13	6 ± 1	0.4 ± 0.1	38 ± 20	Transient
4U 1543−47 (HL Lup)	A2 V	1.1	0.22 ± 0.02	5 ± 2.5	~ 2.5	$-$	Transient
GRS 1009−45 (MM Vel)	(K6-M0)V	0.3	3.17 ± 0.12	$3.6-4.7$	$0.5-0.7$	$-$	Transient
SAX J1819.3-2525 (V4641 Sgr)	B9 III	2.8	2.74 ± 0.12	$9.6(+2.1-0.9)$	$6.5(+1.6-1.0)$	$-$	Transient
XTE 1118+480	(K7-M0)V	0.17	6.1 ± 0.3	$6.0-7.7$	$0.09-0.5$	$-$	Transient
GRS 1915+105	(K-M)III	33.5	9.5 ± 3.0	14 ± 4	1.2 ± 0.2	$-$	Transient

Note: P is the orbital period; $f_V(m) = M_X^3 \sin^3 i/(M_X + M_V)^2$ is the mass function of the optical star; M_X, M_V are the masses of the BH and optical star, respectively; V_{pec} is the peculiar radial velocity of the center of mass of the binary.

that the formation of the BHs in GRO J1655−40 and SAX J1819.3−2525 was accompanied by type Ib/c supernovae explosions, which enriched the donor stars of these systems in nucleosynthesis products from the interiors of their primaries.

Wagner *et al.* [22] carried out spectroscopic and photometric observations of the X-ray nova XTE *J*1118+480, which has a high altitude above the plane of the Galaxy, $z \approx 1.7$ Kpc. This system was discovered in 2000 [30] and identified with an optical
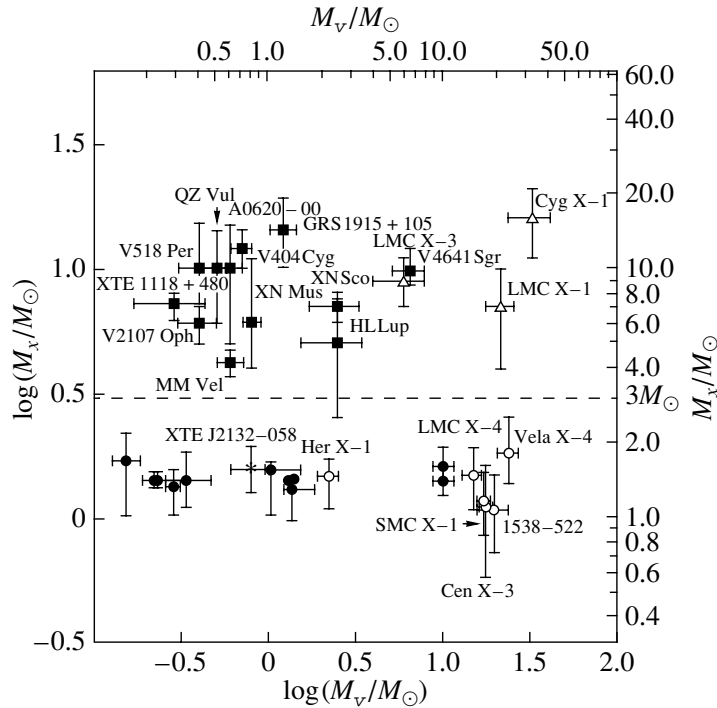
Fig. 1. Dependence of the masses M_X of neutron stars (circles and the cross) and black holes (triangles and squares) on the masses of their companions M_V in close binaries. Filled circles correspond to radio pulsars, hollow circles, to X-ray pulsars, and the cross, to the neutron star in the X-ray nova XTE J2132−058. Filled squares correspond to BHs in X-ray novae, and hollow triangles, to BHs in quasi-stationary X-ray binaries with OB components.

star. The Galactic latitude of the system is high, $b = +62°$, in sharp contrast to other X-ray novae with BHs [15, 16], which are close to the Galactic plane. The optical spectrum of XTE $J1118+480$ in the quiescent state corresponds to a late K7V−M0V star. The orbital period of the system is $P = 0\overset{d}{.}170$, and the mass function of the optical star is $f_V(m) = 6.1 \pm 0.3$ $M_\odot$. The luminosity of the optical star implied by the spectral data is ∼30% of the luminosity of the system at 5800−6400 Å. The rest of the luminosity is provided by the accretion disk. Photometric R observations revealed optical variability with an amplitude of ∼$0\overset{m}{.}2$, due to the orbital motion of the ellipsoidal optical star and eclipses. The orbital inclination of the system is $i = 81° \pm 2°$, and the component mass ratio is $M_X/M_V \approx 20$. These data and the mass function have been used to derive the masses of the BH, $M_X = 6.0−7.7$ $M_\odot$, and optical star, $M_V = 0.09−0.5$ $M_\odot$. XTE $J1118+480$ is apparently the first reliably identified binary with a BH located in the Galactic halo. Its large distance from the Galactic plane probably resulted from the supernova explosion in the system [31].

Grejner *et al.* [23] carried out an infrared spectroscopic study of a unique transient X-ray binary—the "microquasar" GRS 1915+105. The system is located in the Galactic plane at a distance of 11−12 kpc

from the Sun, and is therefore subject to large interstellar absorption. The optical component of the GRS 1915+105 system has been spectroscopically classified as a K−M III red giant. The orbital period, $P = 33\overset{d}{.}5 \pm 1\overset{d}{.}5$, was derived from the Doppler shifts of the absorption lines. The corresponding mass function of the optical star is 9.5 ± 3.0 $M_\odot$. This is the largest mass function of all known X-ray binaries with BHs. If we assume that the mass of the K−M III star is equal to that of a standard single star of this class, 1.2 ± 0.2 $M_\odot$, the mass of the BH in GRS 1915+105 for an inclination of $i = 70° \pm 2°$ will be 14 ± 4 $M_\odot$. The average radius of the Roche lobe of the optical star is 21 ± 4 $R_\odot$. This radius is close to the standard radius for a K−M III star, indicating that the optical component in GRS 1915+105 fills or nearly fills its Roche lobe. The large mass of the BH and the mass-transfer rate in the system determine the physics of the observed microquasar, while the large orbital period and the radius of the orbit $A = 108 \pm 4$ $R_\odot$ impose constraints on evolutionary scenarios for the system [23].

Figure 1 presents the locations of known close binaries with relativistic accretors in a diagram of the mass of the optical star vs. the mass of the relativistic object [20]. It is apparent from Fig. 1 that the masses of the components are not correlated: both BHs and

neutron stars (NSs) occur in binaries with components of both large and small masses. The derived masses for all the X-ray and radio pulsars (19 objects) do not exceed the absolute upper limit for the mass of a neutron star, $\sim 2\ M_\odot$, in full agreement with the expectations of general relativity theory. Moreover, the masses of the neutron stars are confined within narrow limits: $M_{NS} = (1-2)\ M_\odot$, while neither neutron stars or BHs are found in the interval $M_X = (2-4)\ M_\odot$; i.e., the mass distribution for the relativistic objects is bimodal [20].

The absence of a correlation between the masses of the BHs and optical components in X-ray binaries with accreting BHs (Table 1, Fig. 1) is combined with some evidence for a correlation between the BH mass and the orbital period of the system, with increasing orbital period being accompanied by increasing BH masses. The correlation becomes obvious if we consider only systems in which the BH masses are estimated with accuracy better than $\sim 40\%$. Quantitatively, this correlation can be described by the expression $M_X/M_\odot \approx 6.5P^{1/2}$, where P is the orbital period in days. Apart from the obvious observational selection effects, this correlation could be due to an increase of the masses of the collapsing cores of the components in long-period systems, whose axial rotation may be decelerated by the synchronization of orbital and axial rotations.

3. THE EVOLUTIONARY STATUS OF THE X-RAY BINARY GRS 1915+105

3.1. Distribution of Systems with BHs in the Orbital Period−Optical-Component Mass Diagram

It is convenient to analyze the evolutionary status of X-ray binaries with BHs using a diagram of the orbital period vs. the mass of the optical component, shown in Fig. 2. The solid lines indicate the positions of systems with various donors, assuming that the donors fill their Roche lobes. These boundaries were calculated assuming that the mass of the BH is 10 $M_\odot$. (Note that the orbital period of a semidetached system is nearly independent of the accretor mass, and is specified primarily by the parameters of the donor.) The line HeMS indicates the positions of systems whose donors are nondegenerate helium stars, while the line HMS shows the positions of systems whose donors are main-sequence (MS) stars with solar-type surface chemical compositions. The radius within the main sequence roughly doubles for stars with masses exceeding 2 $M_\odot$, providing the finite width of this region in Fig. 2. The concentration of most of the systems toward the HMS line is due to the fact that stars spend most of their lifetime on the main sequence.
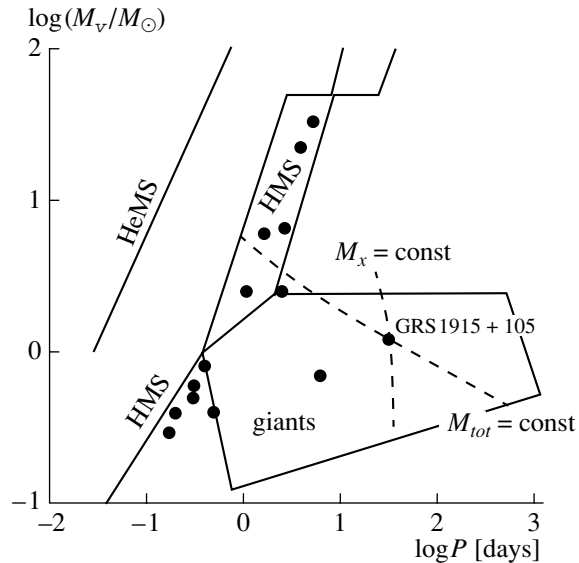
Fig. 2. Location of known X-ray binaries with BHs in the log(orbital period)−log(donor mass) diagram. See text for details.

Let us consider the group of seven systems with donors whose masses are smaller than that of the Sun, located in the lower left corner of Fig. 2. Such donors cannot leave the main sequence over the Hubble time, and therefore such systems should evolve essentially along the HMS line. However, all donors in this group display appreciable deviations from this line. It is possible that the evolution of these systems is strongly affected by an induced stellar wind (ISW) from the donor. The calculations indicate [32] that, in this case, the donor either loses contact with its Roche lobe in the course of the evolution or does not reach the Roche lobe, with the mass transfer being due to the induced stellar wind. Therefore, the orbital periods of such systems will be larger than the case when a MS donor fills its Roche lobe.

The orbital periods increase in more massive systems. Binaries with component masses exceeding $\sim 50\ M_\odot$ lose about half of their total mass in the course of their prior evolution, due to the stellar wind from the primary and its explosion as a supernova. This provides a corresponding increase in the minimum semimajor axes and minimum orbital periods for the most massive but still unobserved X-ray binaries (Fig. 2).

It is known from calculations of the evolution of single stars that those with initial masses of 0.8−2.5 $M_\odot$ display an extended phase of evolution at the stage when the mass of the degenerate helium core increases to its limiting value, $\sim 0.5\ M_\odot$ [31]. The radius of the star in this phase is specified only by the mass of the helium core, making it possible to determine the positions of semidetached systems

with such donors in Fig. 2 (giants) [19]. The orbital periods in these systems can reach several years. In the course of the mass transfer, the mass of the donor can decrease to that of its degenerate helium core $0.13-0.5\ M_\odot$, which corresponds to the lower boundary of the giant domain in Fig. 2. Before the discovery of GRS 1915+105, only one X-ray binary with a BH, V404 Cyg with $P = 6.5$ days, could be confidently classified as such a system. GRS 1915+105 provides a unique opportunity to test current evolutionary concepts for close binaries with giant donors. Evolutionary analyses of its parameters have faced serious problems [23]. Here, we will show that these parameters can be reproduced well in two scenarios for the evolution of a close binary with a massive primary and low-mass companion.

To better illustrate the possible evolution of the GRS 1915+105 system, the dashed lines in Fig. 2 represent two limiting evolutionary tracks (the evolution is directed toward increasing period). The first, conservative, track was plotted under the assumption that the total mass of the system at the X-ray phase does not vary during the mass transfer: $M_{\text{tot}} = \text{const}$. For the second track, it was assumed that the mass transfer at this phase is insignificant compared to the mass loss from the system by the donor's wind: $M_X = \text{const}$. The $M_X = \text{const}$ track and the location of GRS 1915+105 in Fig. 2 suggest the first scenario for the system's evolution during the X-ray phase. The initial mass of the donor (before it filled its Roche lobe) was $1.2-2.5\ M_\odot$. It was only the expansion of the donor after the formation of the degenerate helium core in its interior that turned this into a semidetached system, leading to its current parameters. The initial orbital period in this case differs little from its current value. The conservative track ($M_{\text{tot}} = \text{const}$) suggests another initial mass for the donor. At the time when the Roche lobe was filled, it might have been a MS star with a mass of $3-5\ M_\odot$. At the onset of the mass transfer, the system was compact, with an orbital period as short as $1-3$ days. Further, we will show that the two limiting solutions require two completely different scenarios for the prior evolution of GRS 1915+105, starting from the initial system of two MS stars.

To conclude our analysis of the locations of X-ray binaries with BHs in Fig. 2, we note that all known systems are situated within domains where the donors (filling or nearly filling their Roche lobes) can provide an extended phase of intense mass transfer between the optical donor and the BH accretor. The appreciable dispersion of the donor masses ($0.3-30\ M_\odot$) along with the high initial masses of the BH progenitors, which exceed $\sim 25\ M_\odot$ [32], provide firm and unique evidence for a large dispersion of the

initial mass ratios of the close binary components, which reaches two orders of magnitude.

3.2. Scenario for the Prior Evolution of GRS 1915+105 without a Common Envelope

Let us now try to reconstruct the evolution of the system at previous phases. We will assume that the mass of the BH is $14\ M_\odot$, while the current mass of the subgiant donor filling its Roche lobe is $\sim 1.2\ M_\odot$. The formation of the BH was accompanied by a supernova explosion (probably type Ib/c), and some matter of the BH progenitor was lost in the explosion. The condition under which the system remains gravitationally bound (assuming a circular orbit) is $\Delta M < M_R$, where ΔM is the lost mass and M_R is the mass of the system after the explosion. This condition can be used to estimate the mass lost in the explosion: $\Delta M < 15.2\ M_\odot$. Hence, the mass of the supernova precursor is confined in the interval $14-29\ M_\odot$. Since the system was close before the supernova, the hydrogen envelope of the supernova precursor was lost during preceding phases of the evolution, either due to an intense stellar wind or in a common-envelope phase. Therefore, the supernova precursor was essentially the nondegenerate helium core of a massive initial MS star; i.e., it was a Wolf–Rayet star.

The masses of the helium cores of massive stars M_{He} can be estimated on the basis of evolutionary calculations for such stars [31]:

$$M_{\text{He}}/M_\odot \approx 0.1(M_{\text{MS}}/M_\odot)^{1.4}, \qquad (1)$$

where M_{MS} is the initial mass of the star. This relation yields an estimate for the initial mass of the BH progenitor on the main sequence of $30-60\ M_\odot$. We will now show that, in a scenario in which the massive MS star is transformed into a helium star with an initial donor mass $\sim 1.2\ M_\odot$, it neither filled its Roche lobe nor underwent a common-envelope phase. The variations of the semimajor axis of the system's orbit A in a common-envelope phase can be estimated using the formula [31]

$$M_{\text{MS}}^2/A_0 = M_{V0} \times M_{\text{He}}/A_f, \qquad (2)$$

where M_{V0} is the initial mass of the secondary, M_{He} is the mass of the helium remnant of the primary, and A_0 and A_f are the initial and final semimajor axes of the orbit. To obtain $A_f = 108\ R_\odot$, $M = (30-60)\ M_\odot$, $M_{\text{He}} = (14-29)\ M_\odot$, and $M_{V0} = 1.2\ M_\odot$, the initial semimajor axis of the system should have exceeded $5000-7000\ R_\odot$. It is obvious that binaries with such large distances between the components are not close, since their components are unable to fill their Roche lobes in the course of their evolution.

Therefore, the above analysis indicates that a primary with $M_{V0} = 1.2\ M_\odot$ could not have filled its Roche lobe; instead, it was probably transformed into a nondegenerate helium star under the action of an intense stellar wind. This is possible for MS stars with solar chemical composition and masses exceeding $\sim 50\ M_\odot$ [31]. This is a direct consequence of the absence of red supergiants with such masses and solar chemical composition.

In this scenario, the initial mass of the BH progenitor is constrained to be within very narrow limits: $\sim (50{-}60)\ M_\odot$. Losing mass via the stellar wind, this component is gradually transformed into a helium Wolf–Rayet star with a mass of $\sim (24{-}29)\ M_\odot$ [see (1)]. The collapse of this star leads to the formation of a BH with a mass of $\sim 14\ M_\odot$ in the system. In all, during the prior evolution, the mass of the system decreased by 3–4 times, indicating that its initial semimajor axis was 27–36 $R_\odot$ if $M_{\rm tot}A = $ const. Thus, the assumption of a small initial donor mass $(1.2{-}2\ M_\odot)$ excludes the possibility of a common-envelope phase in the evolution of the system, unlike in the case of shorter-period systems with solar-mass donors, which we studied earlier [19, 32].

3.3. Scenario for the Prior Evolution of GRS 1915+105 with a Common Envelope

Let us now consider the prior evolution of the system in the case of a large initial donor mass. Assuming that its initial mass was $\sim 4\ M_\odot$ and that the mass transfer is conservative (the track $M_{\rm tot} = $ const in Fig. 2) and using the equation of conservation of angular momentum $A M_X^2 M_V^2 = $ const, we find from the current orbital semimajor axis $\sim 108\ R_\odot$ and donor mass $1.2\ M_\odot$ that the semimajor axis was $\sim 15\ R_\odot$ when the donor filled its Roche lobe. It is clear that a common-envelope stage is unavoidable in the formation of such a close massive system, consisting of a BH and a donor with a mass of $\sim 4\ M_\odot$. For an initial mass for the primary $\lesssim 50\ M_\odot$, a mass for its helium remnant $\lesssim 24\ M_\odot$, and a donor mass $\sim 4\ M_\odot$, formula (2) can be used to estimate the initial semimajor orbital axis of the system, which turns out to be smaller than 390 $R_\odot$, indicating that the system is a close binary.

Note that all the numerical estimates for the two scenarios for the prior evolution of the GRS 1915+105 system remain unjustified. The reason is that, to estimate evolutionary variations of the component masses and the orbital semimajor axis, we must adopt some assumptions about the extent to which the mass and orbital angular momentum are conserved. However, the possibility of these two scenarios seems quite certain.

3.4. Accuracy of the Parameters of GRS 1915+105

The final choice between the scenarios can be made after calculations of the evolution of GRS 1915+105 during the X-ray phase supplemented by an estimate of the rate of mass transfer between the components. The observational data [23] indicate that the average X-ray luminosity of the system is close to the Eddington limit for a BH with a mass of $\sim 14\ M_\odot$. Unfortunately, this luminosity has not yet been accurately estimated quantitatively and remains uncertain by a factor of two to three due to the variability of the X-ray flux by factors of up to five [33]. We adopted the Eddington limit for the mass-transfer rate, equal to $1.4 \times 10^{-8}\ M_\odot/{\rm yr}$, in accordance with the formula proposed by King [34]: $\dot{M}_{\rm Edd} = 1.0 \times 10^{-8} M_X$. On the other hand, according to [33], the mass-transfer rate is $(2-10) \times 10^{-8}\ M_\odot/{\rm yr}$. We therefore adopted the average value $6 \times 10^{-8}\ M_\odot/{\rm yr}$, taking $2 \times 10^{-8}\ M_\odot/{\rm yr}$ and the Eddington limit as lower and upper limits, respectively.

The orbital period of the system is reliably known with an accuracy of $\sim 5\%$ [23]. The last evolutionarily significant parameter, the donor mass, was derived from its spectral type, K–M III [23]. When using this method to estimate masses, it should be kept in mind that, evolutionarily, the giant branch is convergent for stars with initial masses 0.8–2.5 $M_\odot$ possessing degenerate helium cores. Assuming the donor with mass 1.2 $M_\odot$ fills its Roche lobe, we can estimate the radius of this star to be $\sim 21\ R_\odot$ and the mass of the degenerate helium core to be $\sim 0.30\ M_\odot$ [31]. Thus, along with the remaining uncertainty within a factor of two to three in the spectral estimate of the current donor mass, the mass of its degenerate helium core can serve as a supplementary tool for the selection of appropriate evolutionary tracks. The noted uncertainties in the observed parameters of GRS 1915+105 must be taken into account when the evolution of the system is simulated numerically during the semidetached stage and reconstructed at phases prior to the observed phase.

4. CALCULATION OF THE EVOLUTION OF THE GRS 1915+105 SYSTEM AFTER THE FORMATION OF THE BLACK HOLE

4.1. Brief Description of the Calculation of the Evolution of the Close Binary

To reproduce the observed parameters of GRS 1915+105, we carried out calculations of the evolution of a close binary with a BH. The calculations were made in two models for the evolution: (1) standard evolution, with mass transfer at the semidetached phase, and (2) evolution taking into account
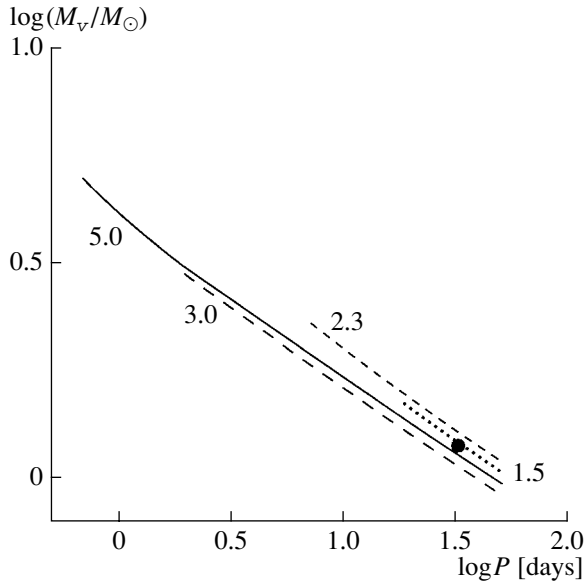
log(M_v/M_☉)

Fig. 3. Tracks calculated for the standard evolutionary model in the log(orbital period)—log(donor mass) diagram. The filled circle denotes the position of GRS 1915+105. The solid, long-dashed, short-dashed, and dotted lines correspond to initial donor masses of $5\,M_\odot$, $3\,M_\odot$, $2.3\,M_\odot$, and $1.5\,M_\odot$, respectively.

log(dM_v/dt), (M_☉/yeas)

Fig. 4. Tracks calculated for the standard evolutionary model in the log(orbital period)—log(donor mass-loss rate) diagram. The filled circle denotes the position of GRS 1915+105. The solid, long-dashed, short-dashed, and dotted lines correspond to initial donor masses of $5\,M_\odot$, $3\,M_\odot$, $2.3\,M_\odot$, and $1.5\,M_\odot$, respectively.

an induced stellar wind from the donor. Both models are described in detail in [32, 35], together with the evolutionary code used in the calculations. Here, we only present a brief qualitative description of the models.

The standard evolutionary model takes into account the the loss of angular momentum by the system via the radiation of gravitation waves and the magnetic stellar wind of the donor, mass transfer between the components, and mass loss from the system when the rate of mass loss by the donor exceeds the Eddington rate. In the last case, we assume that the excess matter leaves the system, carrying away specific angular momentum of the accretor. In this model, mass transfer is possible only at the semidetached phase of the evolution, when the donor fills its Roche lobe.

The evolutionary model including an induced stellar wind from the donor takes into account another potentially important factor: the illumination of the donor by hard radiation originating during of the accretion of matter onto the BH [35]. It is assumed that this results in evolutionarily significant mass loss by the donor in the form of the stellar wind, as is supported by observations [36, 37]. Some of the wind material is captured by the accretor, maintaining its X-ray radiation, while the remainder leaves the system, carrying away specific angular momentum equal to that of the donor. Thus, another process that increases the semimajor axis of the orbit is added.
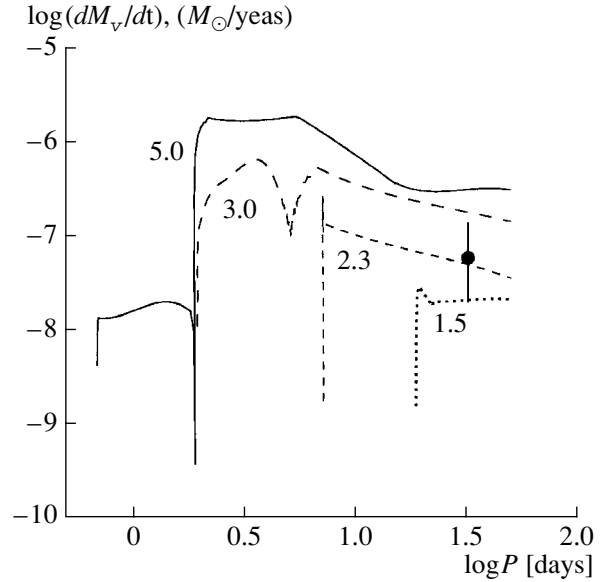
In addition, when the induced stellar wind is taken into account, mass transfer also becomes possible at detached phases, when the donor does not fill its Roche lobe. We took the basic parameters of the ISW model—the ratio of the velocity of the stellar wind and the parabolic velocity and the efficiency of the donor's illumination—to be equal to unity. Note, however, that the intensity of the induced stellar wind is specified by parameters whose exact values cannot be estimated. Therefore, our calculations for the evolution of binaries with BHs including the effect of the induced stellar wind must thus far be considered only illustrations of possible evolutionary scenarios for close binaries with relativistic accretors.

4.2. Initial Parameters for the Calculation of Tracks Reproducing the GRS 1915+105 System

When studying the evolution of the system after the formation of the BH, we assumed that the donor was initially an unevolved MS star. The current parameters of the system were adopted in accordance with [23]: the mass of the BH was $M_X = 14\,M_\odot$, the mass of the donor was $M_V = 1.2\,M_\odot$, and the orbital period was $P = 33.5$ days. Our calculations were aimed at finding the initial mass of the donor M_{V0} and the semimajor orbital axis A_0 that provide a good description of the observed parameters of the system at the current stage of its evolution. We considered values for M_{V0} in the interval 1.5–$6\,M_\odot$ (Table 2),

Table 2. Binary parameters describing GRS 1915+105

Model	$M_{V0}/M_\odot$	$A_0/R_\odot$	P_0, days	$(M_{\text{He}})_0$	R/R_R	M_{He}	$\log(L/L_\odot)$	$\log T_{\text{eff}}$, TO	$M_{\text{acc}}/M_\odot$
Standard	1.5	77	20.1	0.29	1.00	0.31	2.1	3.61	0.30
Standard	2.3	41	7.5	0.26	1.00	0.31	2.1	3.61	1.10
Standard	3.0	17	2.0	0.17	1.00	0.31	2.1	3.61	0.79
Standard	5.0	9	0.7	0.0	1.00	0.31	2.1	3.61	2.19
With ISW	1.5	102	30.2	0.15	0.41	0.23	1.5	3.65	0.04
With ISW	2.0	80	20.7	0.0	0.61	0.26	1.7	3.64	0.22
With ISW	3.0	39	6.9	0.0	0.95	0.31	2.1	3.61	0.67
With ISW	6.0	22	2.6	0.0	0.88	0.26	2.2	3.70	1.01

Note: M_{V0} is the initial donor mass, A_0 and P_0 are the initial semimajor orbital axis and period of the system (after the formation of the BH), $(M_{\text{He}})_0$ is the mass of the donor's helium core at the onset of the mass transfer, R/R_R is the ratio of the radii of the current donor and its Roche lobe, M_{He} is the current mass of the donor's helium core, $L/L_\odot$ and T_{eff} are the current luminosity and effective temperature of the donor, and M_{acc} is the amount of matter accreted by the BH up to the present time.

fitting A_0 for each M_{V0}. The fitting procedure was based on obtaining a positive correlation between A_0 and the theoretical orbital period P, which is reached for $M_V = 1.2\ M_\odot$. However, the final criterion for selecting the initial donor mass is the theoretical mass-transfer rate at the observed phase of its evolution and its variation with time. In the calculated tracks, the mass of the accretor for $M_V = 1.2\ M_\odot$ slightly exceeds $14\ M_\odot$ (Table 2); however, we did not take this into account, since the mass of the BH is known only to within $4\ M_\odot$.

4.3. Calculation Results for the Standard Model

In the standard model for the evolution of binaries, mass transfer is possible only when the donor has filled its Roche lobe. For example, for donors with $M_{V0} = 1.5$ and $3\ M_\odot$, the values of A_0 are $77.4\ R_\odot$ and $17.1\ R_\odot$, and these stars fill their Roche lobes when they are already evolved and the relative masses of their helium cores are 0.20 and 0.06, respectively. The semimajor orbital axis remains nearly unchanged over the prior evolution of the donor: the decreases due to gravitational radiation (and, for $1.5\ M_\odot$, also due to the magnetic stellar wind, after the formation of the convective envelope in the course of the evolution) are 2.4% and 0.5%, respectively.

For a donor with $M_{V0} = 5\ M_\odot$, $A_0 = 8.9\ R_\odot$, and the star fills its Roche lobe when it is on the zero-age main sequence. This essentially excludes M_{V0} values exceeding $5\ M_\odot$. Additional calculations indicate that, for a donor with an initial mass of $6\ M_\odot$ that fills its Roche lobe when it is on the main sequence, the orbital period when its current mass reaches $1.2\ M_\odot$

will be too long (46 days); this value cannot be reduced, since this period will be even longer for a donor that is initially evolved.

Figure 3 presents four evolutionary tracks for $M_{V0} = 1.5, 2.3, 3,$ and $5\ M_\odot$ in the period−donor-mass diagram. Figure 4 presents the same tracks in the period−donor mass-loss rate diagram. For $M_{V0} = 5\ M_\odot$, the rate of mass loss by the donor appreciably exceeds the Eddington value. For $M_{V0} = 3\ M_\odot$, this excess is small; however, both these tracks indicate a prior phase of evolution with a higher mass-transfer rate, which may result in the formation of a common envelope and alter the system's evolution. It is, therefore, unlikely, that the initial mass of the donor exceeds $3\ M_\odot$. For $M_{V0} = 1.5\ M_\odot$, the mass-transfer rate is probably insufficient to describe GRS 1915+105, since it is $0.14\ \dot{M}_{\text{Edd}}$. However, since the system is transient, its average mass-transfer rate may be appreciably lower than is currently observed. Therefore, we cannot exclude values of M_{V0} close to $\sim 1.5\ M_\odot$.

Note that the system with $M_{V0} = 5\ M_\odot$ has a mass-loss rate of $\sim 10^{-6}\ M_\odot$/yr during some fraction of the semidetached phase (Fig. 4). In a system with a BH mass of $\sim 60\ M_\odot$, this matter would be almost completely accreted, and the X-ray luminosity would be $\sim 10^{40}$ erg/s. An X-ray source (probably a binary) with a similar luminosity, $L_X = 8 \times 10^{39}$ erg/s, was observed by Wang [38]. About 20 sources with $L_X \gtrsim 10^{39}$ erg/s ($M_X \gtrsim 10\ M_\odot$) have also been observed in the Antennae [39]. If a microquasar model with a face-on relativistic jet is excluded for such systems,
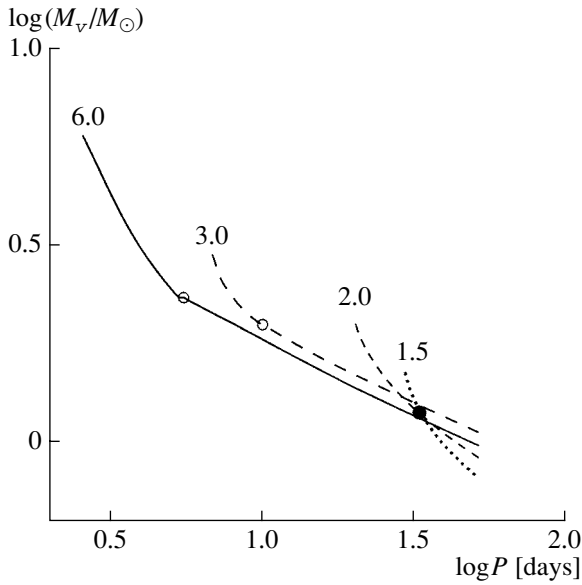
Fig. 5. Tracks calculated for the evolutionary model with induced stellar wind in the log(orbital period)—log(donor mass) diagram. The filled circle denotes the position of GRS 1915+105. The solid, long-dashed, short-dashed, and dotted lines correspond to initial donor masses of $6\,M_\odot$, $3\,M_\odot$, $2\,M_\odot$, and $1.5\,M_\odot$, respectively. The circles on the tracks for 6 and 3 $M_\odot$ mark the time when the donors fill their Roche lobes.

Fig. 6. Tracks calculated for the evolutionary model with induced stellar wind in the log(orbital period)—log(donor mass-loss rate) diagram. The filled circle denotes the position of GRS 1915+105. The solid, long-dashed, short-dashed, and dotted lines correspond to initial donor masses of $6\,M_\odot$, $3\,M_\odot$, $2\,M_\odot$, and $1.5\,M_\odot$, respectively.

it is natural to look for clues to their nature within models for close binaries with massive BHs and donors with masses of $\sim 5\,M_\odot$, whose evolution we are studying here.

Thus, in the standard model for binary evolution, we found that the most probable initial mass of the donor in GRS 1915+105 is approximately $1.5-3\,M_\odot$, while the initial semimajor orbital axis prior to the X-ray stage was $17-77\,R_\odot$.

4.4. Calculation Results for the Close-Binary Model with an Induced Stellar Wind

In the model for the evolution of binaries with induced stellar winds, efficient mass transfer between the components can begin before the donor fills its Roche lobe. In order for the mass transfer to start, the degree of Roche lobe filling by the donor must exceed some critical value necessary for the initiation of a self-maintaining stellar wind [32]. The calculations indicate that, in this case, the mass transfer begins immediately for systems with $M_{V0} = 5$ and $6\,M_\odot$, while, in systems with smaller M_{V0} values, mass transfer occurs only after the degree of Roche lobe filling increases during the expansion of the donor due to the evolution of its core. For example, for a donor with $M_{V0} = 1.5\,M_\odot$, the initial degree of Roche-lobe filling must increase from the initial 0.07 to 0.17. In
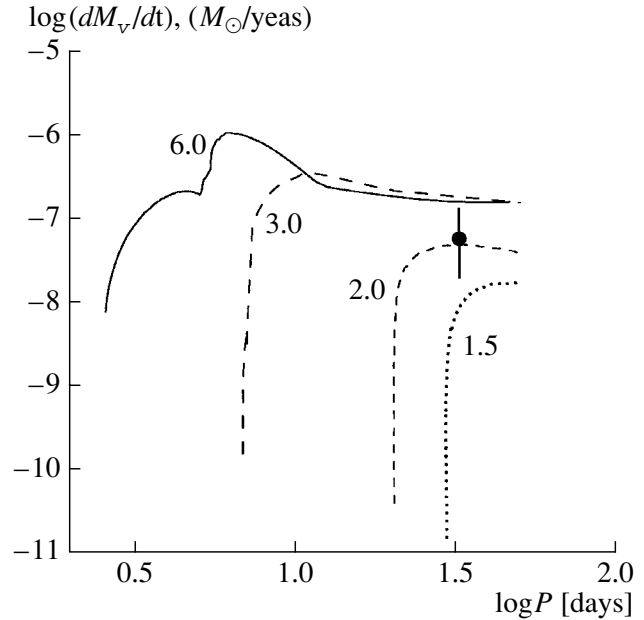
the course of the subsequent evolution, the degree of the donor's Roche lobe filling will increase substantially.

Figure 5 presents four evolutionary tracks for $M_{V0} = 1.5$, 2, 3, and $6\,M_\odot$ in the period–donor-mass diagram. Figure 6 presents the same tracks in the period–donor mass-loss rate diagram. At some point in the evolution, donors with $M_{V0} \geq 3\,M_\odot$ fill their Roche lobes, and this situation continues over a definite evolutionary phase. However, after some time, the degree of Roche lobe filling again decreases, and this occurs sooner for more massive donors (Table 2). Donors with smaller masses never attain contact with their Roche lobes, and mass transfer occurs only via the induced stellar wind, as is typical for the evolution of systems with low-mass donors in this model [32]. For example, for donors with $M_{V0} = 1.5$, 2, and 3 $M_\odot$, the degree of Roche lobe filling for $M_V = 1.2\,M_\odot$ is 0.41, 0.61, and 0.95, respectively.

As we can see from Fig. 6, the same problem occurs for tracks for massive donors as in the standard model: they display a prior evolutionary phase with a super-Eddington mass-transfer rate, which can result in the formation of a common envelope. Therefore, values $M_{V0} > 3\,M_\odot$ are also unlikely here, although, taking into account the induced stellar wind, we can formally select A_0 values even for $M_{V0} = 6\,M_\odot$ (unlike the standard model). For

$M_{V0} = 1.5\ M_\odot$, the mass-transfer rate for the ISW model is even lower than for the standard model: only $0.02\ \dot{M}_{\mathrm{Edd}}$. Consequently, in this case, the lower limit for the donor's initial mass may exceed somewhat that for the standard model.

In the ISW model, there is some increase of the initial semimajor orbital axis compared to the standard evolutionary model (Table 2). This is due to the fact that the tracks for the model with induced stellar wind (particularly for donors with small initial masses) are close to the limiting track $M_X = \mathrm{const}$ shown in Fig. 2, for which A does not increase significantly in the course of the evolution. The tracks calculated for the standard model are equivalent to the second limiting track $M_{\mathrm{tot}} = \mathrm{const}$, where the decrease of the donor mass is accompanied by a substantial increase of the semimajor orbital axis.

Thus, we conclude that, in the model for the binary evolution taking into account the induced stellar wind, the initial donor mass in GRS 1915+105 should be approximately $1.5{-}3\ M_\odot$, and the initial semimajor orbital axis prior to the onset of the X-ray phase was $40{-}100\ R_\odot$.

Note that the modern model for the current donor in GRS 1915+105 filling its Roche lobe is a subgiant with a radius of $21\ R_\odot$ and a degenerate helium core with a mass of $0.31\ M_\odot$. However, the current donors obtained in the evolutionary model with induced stellar wind do not fill their Roche lobes and possess smaller radii and helium cores. For example, donors with $M_{V0} = 1.5$ and $2\ M_\odot$ have radii of 9 and $13\ R_\odot$ and helium cores with masses of 0.23 and $0.26\ M_\odot$. However, the current donor obtained for $M_{V0} = 3\ M_\odot$ taking into account the induced stellar wind is essentially the same as in the standard model.

5. CONCLUSION

We have aimed to clarify the evolutionary status of GRS 1915+105, the longest period X-ray binary with an accreting BH. Our modeling of the evolutionary phase after the formation of the BH indicates that the current parameters of the system—the donor mass, orbital period, and observed accretion rate of the BH—may be consistent with a initial donor mass of $1.5{-}3\ M_\odot$. Initial donor masses exceeding $3\ M_\odot$ can probably be excluded due to the presence of an extended phase with a super-Eddington accretion rate. This should result in the formation of common envelopes, which is inconsistent with the current parameters of the system. Unfortunately, the precise limiting value for the mass-transfer rate for which the formation of common envelopes begins is unknown. The presence of jets may shift it toward higher accretion rates. However, in the absence of

reliable estimates for this shift, we take this limiting value to coincide with the Eddington limit.

Analyzing the prior stage of the evolution of GRS 1915+105, from an initial system of two MS stars to the formation of the BH, we conclude that two different evolutionary scenarios are possible. The choice between them depends on the initial mass of the primary. If this mass exceeds $\sim 50\ M_\odot$, the primary is transformed into a helium Wolf−Rayet star without expansion due to the intense stellar wind at the MS stage, with the subsequent collapse of its core into a BH. The initial mass of the secondary (the current donor) must be $1.5{-}2.5\ M_\odot$, while the initial semimajor axis must be $20{-}30\ R_\odot$.

If the initial mass of the BH progenitor is smaller than $\sim 50\ M_\odot$, the star expands after the MS stage and fills its Roche lobe. In this case, the initial mass of the secondary is $2.5{-}3\ M_\odot$; therefore, the filling of the Roche lobe of the primary results in the formation of a common envelope and a decrease of the semimajor axis of the system to $10{-}20\ R_\odot$. The explosion of the helium Wolf−Rayet star—the remnant of the primary—leads to the formation of the initial state, after which the mass transfer from the donor onto the BH accompanied by the increase of the semimajor orbital axis leads to the formation of a system similar to GRS 1915+105.

The complete lack of information about the initial mass-ratio distribution of binary components for $q = M_V/M_X \lesssim 0.1$ [31] and uncertainties in the current parameters of the system make it impossible to reliably choose between scenarios for the prior evolution of the GRS 1915+105 system at this time.

6. ACKNOWLEDGMENTS

REFERENCES

1. Ya. B. Zel'dovich, Dokl. Akad. Nauk SSSR **155**, 67 (1964) [Sov. Phys. Dokl. **9**, 195 (1964)].
2. E. E. Salpeter, Astrophys. J. **140**, 796 (1964).
3. N. I. Shakura, Astron. Zh. **49**, 921 (1972) [Sov. Astron. **16**, 756 (1972)].
4. N. I. Shakura and R. A. Sunyaev, Astron. Astrophys. **24**, 337 (1973).
5. J. Pringle and M. Rees, Astron. Astrophys. **21**, 1 (1972).
6. I. D. Novikov and K. S. Thorne, in *Black Holes,* Ed. by C. De Witt and D. De Witt (Gordon and Breach, New York, 1973).
7. W. C. Forman, C. Jones, L. Cominsky, *et al.*, Astrophys. J., Suppl. Ser. **38**, 357 (1978).

8. N. L. Webster and P. Murdin, Nature **235**, 37 (1972).

9. C. T. Bolton, Nature **235**, 271 (1972).

10. C. T. Bolton, Nature Phys. Sci. **240**, 124 (1972).

11. A. M. Cherepashchuk, Yu. N. Efremov, N. E. Kurochkin, *et al.*, Inf. Bull. Var. Stars, No. 720 (1972).

12. J. N. Bahcall and N. A. Bahcall, Astrophys. J. **178**, L1 (1972).

13. V. M. Lyutyĭ, R. A. Syunyaev, and A. M. Cherepashchuk, Astron. Zh. **50**, 3 (1973) [Sov. Astron. **17**, 1 (1973)].

14. V. M. Lyutyĭ, R. A. Syunyaev, and A. M. Cherepashchuk, Astron. Zh. **51**, 1150 (1974) [Sov. Astron. **18**, 684 (1974)].

15. P. Charles, in *Black Holes in Binaries and Galactic,* Ed. by L. Kaper, E. P. J. van den Heuvel, and P. A. Woudt (Springer-Verlag, Berlin, 2001), p. 27.

16. A. M. Cherepashchuk, Space Sci. Rev. **93**, 471 (2000).

17. A. V. Tutukov and A. M. Cherepashchuk, Astron. Zh. **66**, 1172 (1989) [Sov. Astron. **33**, 606 (1989)].

18. A. V. Tutukov and A. M. Cherepashchuk, Astron. Zh. **70**, 307 (1993) [Astron. Rep. **37**, 159 (1993)].

19. A. V. Tutukov and A. M. Cherepashchuk, Astron. Zh. **74**, 407 (1997) [Astron. Rep. **41**, 355 (1997)].

20. A. M. Cherepashchuk, Usp. Fiz. Nauk (2002) (in press).

21. J. A. Orosz, E. Kuulkers, M. Van den Klis, *et al.*, astro-ph/0103045.

22. R. M. Wagner, C. B. Foltz, T. Chahbaz, *et al.*, Astrophys. J. **556**, 42 (2001).

23. J. Grejner, J. G. Guby, and M. J. McCaughrean, Nature **414**, 522 (2001).

24. J. J. M. in't Zand, E. Kuulkers, A. Bazzano, *et al.*, Astron. Astrophys. **357**, 520 (2000).

25. C. B. Markwardt, J. E. Swank, and F. E. Marshall, IAU Circ., No. 7120 (1999).

26. R. M. Hjellming, M. P. Rupen, R. W. Hunshead, *et al.*, Astrophys. J. **544**, 977 (2000).

27. V. P. Goranskiĭ, Astron. Tsirk., No. 1024, 3 (1978).

28. V. P. Goranskij, Inf. Bull. Var. Stars, No. 3464 (1990).

29. G. Izraelian, R. Rebolo, G. Basri, *et al.*, Nature **401**, 142 (1999).

30. R. A. Remillard, E. Morgan, D. Smith, and E. Smith, IAU Circ., No. 7389 (2000).

31. A. G. Masevich and A. V. Tutukov, *Stellar Evolution: Theory and Observations* [in Russian] (Nauka, Moscow, 1988).

32. A. V. Tutukov and A. V. Fedorova, Astron. Zh. (2002) (in press) [Astron. Rep. (2002) (in press)].

33. L. Belloni, M. Mendez, and A. R. King, Astrophys. J. **488**, L109 (1997).

34. A. R. King, in *Black Holes in Binaries and Galactic,* Ed. by L. Kaper, E. P. J. van den Heuvel, and P. A. Woudt (Springer-Verlag, Berlin, 2001), p. 155.

35. I. Iben, A. V. Tutukov, and A. V. Fedorova, Astrophys. J. **486**, 955 (1997).

36. E. P. J. van den Heuvel and J. van Paradijs, Nature **334**, 227 (1988).

37. F. Camilo, D. R. Lorimer, P. Frejre, *et al.*, Astrophys. J. **535**, 975 (2000).

38. D. Q. Wang, astro-ph/0201230.

39. A. Zezas *et al.*, astro-ph/0203174; astro-ph/0203175; astro-ph/0203176.

Translated by K. Maslennikov

The Nonthermal Radio Emission of WR 140 in a Model with Colliding Two-Phase Winds

O. V. Abramova, P. V. Averin, and K. V. Bychkov

Sternberg Astronomical Institute, Universitetskiĭ pr. 13, Moscow, 119899 Russia
Received March 15, 2002; in final form, May 23, 2002

Abstract—We present a model in which the nonthermal radio emission of binary systems containing Wolf–Rayet and O components is due to collisions between clouds belonging to dense phases of the wind of each star. The relativistic electrons are generated during the propagation of fast shock waves through the clouds and their subsequent de-excitation. The initial injection of superthermal particles is due to photoionization of the de-excited cold gas by hard radiation from the shock front. Therefore, the injection takes place in cloud regions fairly far from the front. Further, the superthermal electrons are accelerated by the betatron mechanism to relativistic energies during the isobaric compression of the cloud material, when most of the gas radiates its energy. Collisions between the clouds can occur far beyond the contact boundary between the rarefied wind components. Thus, the model avoids the problem of strong low-frequency absorption of the radiation. © *2003 MAIK "Nauka/Interperiodica".*

1. INTRODUCTION

In the current paper, we explain the nonthermal radio emission of binary stars containing Wolf–Rayet (WR) and OB components using the concept of a two-phase stellar wind, i.e., a wind involving dense, compact clouds along with a rarefied gas. Until recently, only a rarefied wind component has been taken into account in most studies of such objects. The idea that there might be additional ultraviolet radiation in close binary systems due to dissipation occurring when supersonic flows of gas from the WR star pass around the O component was suggested by Cherepashchuk [1] in 1967 to explain the excess HeII emission of V444 Cyg star. The concept of a one-phase wind was developed in many subsequent papers. Nevertheless, it gradually became clear that certain observations could be more easily interpreted in models with two-phase winds.

A two-phase stellar-wind model for Wolf–Rayet supernova precursors was proposed by Bychkov in 1979 [2] to explain the fine filamentary structure of supernova remnants. In 1984, Cherepashchuk *et al.* [3] suggested that there should be less absorption of radio emission in a two-phase than in a one-phase stellar wind, since the irregular density distribution will make the wind more transparent. Somewhat later, in 1990, Cherepashchuk [4] applied the concept of a clumpy stellar wind in order to remove the discrepancy between X-ray luminosities calculated theoretically and observed by the *Einstein* observatory. A comparison of the mass-loss rates of the WN5 component of the binary V444 Cyg determined using two independent methods provides evidence in support of the presence of clouds: analysis of the radio observations yields a value an order of magnitude higher than the value derived from optical observations [5]. In addition, the presence of clouds in the wind of the WR star can explain the rapid spectral and photometric variability of the system [3, 6, 7].

The current paper continues the earlier work of Aleksandrova (Abramova) and Bychkov in applying a two-phase stellar-wind model to the binary system WR 140. This model also enables us to explain the X-ray and infrared emission of this system [8, 9].

The nonthermal radio emission is usually believed to be associated with the acceleration of relativistic electrons at a shock front. We shall consider a model in which the relativistic electrons are accelerated in collisions of clouds. The theory will be compared with observations for the particular case of WR 140, which has been studied in detail over a wide range of wavelengths from radio to X-ray.

The speeds of the outflows from the WR and OB stars exceed the speed of sound by more than two orders of magnitude. Therefore, the shock waves produced by collisions between flows from the different components can be considered infinitely strong. The binary system is schematically (not to scale) drawn in Fig. 1. The interaction between the rarefied components results in the formation of a contact boundary C, shown by the solid curve, with standing shock waves F_{WR} and F_{OB} on either side of the contact boundary, drawn by the dashed curves.
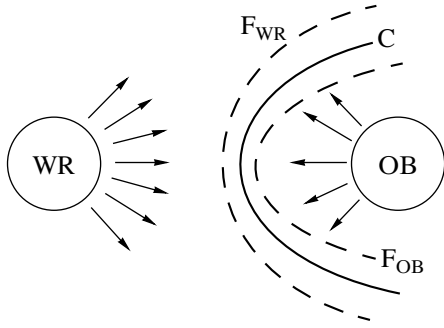
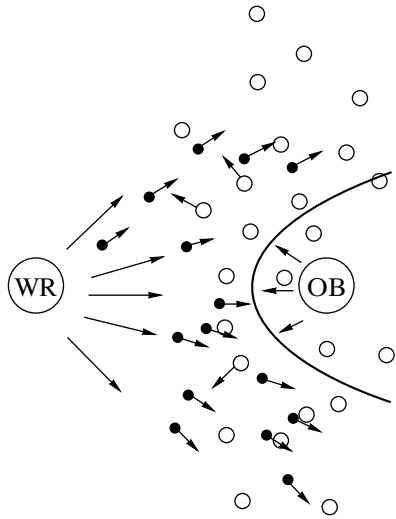**Fig. 1.** Rarefied phases of the stellar wind.

Fig. 2. Interaction between the two-phase winds.

Only rarefied wind phases have usually been considered in previous studies dealing with superthermal particles. The region of electron acceleration in such models is concentrated near the standing shocks. If the velocity of the inflowing gas is taken to be about 3000 km/s, which is typical for binary systems containing OB and WR components, the gas temperature at the front should be hundreds of millions of degrees, so that the generation of energetic particles seems quite probable. However, after passing through the front, the gas flows away and its density decreases. As a result, the superthermal particles undergo adiabatic energy losses. Moreover, as was shown by White and Becker [10], the high density of ionized gas in the supposed region of electron acceleration should result in considerable absorption of the nonthermal radio emission at $\lambda = 20$ cm. However, their observations showed the opposite behavior: measurements at $\lambda = 2, 4,$ and 20 cm over the entire orbital period of the system showed an absence of a low-frequency cut-off. White and Becker [10] interpreted this result as indicating that the wind from the WR component is concentrated predominantly

in the equatorial plane, which is inclined at some angle to the orbital plane. When the O star is in front of the disk, the radio emission reaches the observer unhindered. However, if the O star is behind the disk, there will be absorption. Further, the contact boundary between the two winds is quite extended and passes through regions with very different densities and optical depths at various frequencies. Therefore, if absorption of the nonthermal radio emission is important, then the model explaining the observations must be very sophisticated [see 10, p. 356].

Therefore, if only the rarefied components of the wind are taken into account, there are two difficulties: (1) the adiabatic energy losses of the superthermal particles after their initial acceleration and (2) the expected absorption of low-frequency radio emission. In addition, such models do not specify a mechanism for the acceleration.

To overcome these difficulties, we shall consider below the injection and subsequent acceleration of superthermal electrons in the presence of clouds. A simplified model for the interaction between the two-phase winds is presented in Fig. 2. The solid curve denotes the contact boundary (marked C in Fig. 1). The filled and hollow circles represent clouds ejected from the WR star and OB star, respectively. To avoid excessive complexity of the figure, we have not drawn shock waves in the rarefied gas. Let us consider collisions of the clouds in more detail. The shock waves assumed to be responsible for the electron acceleration begin to propagate inside each cloud just after the collision. Let us now formulate this model more fully.

2. DESCRIPTION OF THE MODEL

A collision between clouds is schematically presented in Fig. 3, where W is the flux from the Wolf–Rayet star, O is the flux from OB star, and B is the contact boundary. The directions of the cloud motions are shown by the solid long arrows. To avoid excessive complexity, we have drawn only features important for discussing the initial injection and subsequent acceleration of the superthermal electrons. The shock S_1 propagates through the cloud W, and the shock S_2 propagates through the cloud O. The dashed arrows show the directions of motion of the fronts with respect to the boundary B.

The gas temperature at the viscous shock depends on the ratio of the densities in the clouds. Let us assume that the cloud on the right is considerably more dense than the cloud on the left. Then, the front S_1 moves relative to the undisturbed medium W with a velocity approximately equal to the sum of the cloud velocities. Together with the large helium content in the flow from the WR star, this facilitates

strong heating of the plasma at the viscous shock. It is not important whether or not there is de-excitation behind the front S_1, but we shall assume that the O cloud is sufficiently dense that there is radiative cooling in this cloud. The region of de-excited gas is marked by the letter D.

The superthermal electrons are injected during the photoionization of the cold gas by the hard radiation, which is produced primarily in the front S_1. Their subsequent behavior is determined by the ratio of the rate of ionization losses $(dE/dt)_i$ and the acceleration efficiency $(dE/dt)_a$, which depends on the particle energy E. The quantity $(dE/dt)_i$ for a nonrelativistic particle in a fully ionized plasma decreases as $E^{-1/2}$, while $(dE/dt)_a$ depends on the particular acceleration mechanism considered. The isobaric compression of the gas experiencing de-excitation is accompanied by betatron acceleration of the injected electrons in the frozen-in magnetic field, with the rate of the energy gain increasing with E. Thus, there exists a threshold energy E_{thr} with the following property: electrons whose initial energies E_0 are less than the threshold energy will gradually mix with the ambient thermal particles, while those with $E_0 > E_{thr}$ will be accelerated after their injection. In the following sections, we will elucidate the conditions for acceleration of the electrons to relativistic energies and observational differences between various models with a rarefied wind and clouds.

3. CONDITIONS FOR ELECTRON ACCELERATION

Let us assume that a superthermal electron is produced in the plasma via photoionization. Its subsequent behavior is determined by the competition between two processes—ionization losses and betatron acceleration. Assuming that the acceleration is followed by efficient isotropization, we obtain for nonrelativistic particles

$$\left(\frac{dE}{dt}\right)_a = \frac{2}{3}\frac{E}{n}\frac{dn}{dt}, \tag{2.1}$$

where n is the density of the thermal component of the medium. The ionization losses in the fully ionized plasma in the nonrelativistic case are [11]

$$-\left(\frac{dE}{dt}\right)_i = \frac{2\pi n e^4 L}{\sqrt{2mE}}, \tag{2.2}$$

where

$$L = \ln\left(\frac{4mE^2}{\pi e^2 n \hbar^2}\right) \approx 35 \ln\left(\frac{E_{keV}^2}{n_{13}}\right), \tag{2.3}$$

m is the electron mass, e is the electron electrical charge, $\hbar$ is Planck's constant, E_{keV} is the energy in
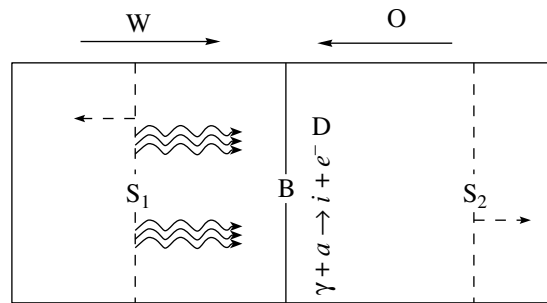
Fig. 3. Collision between the clouds.

keV, and $n_{13} = n/10^{13}$ cm^{-3}. We shall be interested in energies of about $100-200$ keV and densities of the order of $10^{14}-10^{16}$ cm^{-3}.

The derivative dn/dt is determined by the compression of the gas due to de-excitation:

$$\frac{5}{2}\frac{d}{dt}(kT) = -n\varphi(T) \tag{2.4}$$

at the constant pressure p

$$nkT = p. \tag{2.5}$$

The rate of radiative losses $\varphi(T)$ is calculated per electron and per heavy particle.

Let us consider the relationship between the de-excitation of the thermal component of the plasma and the acceleration of an injected electron. Using $(2.1)-(2.5)$, we can write E as a function of T:

$$\frac{dE}{d(kT)} = -\frac{2}{3}\frac{E}{kT} + \frac{5\pi e^4 L}{\varphi(T)\sqrt{2mE}}. \tag{2.6}$$

Ignoring the weak dependence of L on n and E, we obtain a solution of (2.6) for the initial values T_0 and $E_0 = E(T_0)$:

$$\frac{E}{E_0} = \left(\frac{T_0}{T}\right)^{2/3}\left[1 - B\,\Phi(T, T_0)\right]^{2/3}, \tag{2.7}$$

where

$$B = \frac{15\pi}{2}\frac{ke^4 L}{\sqrt{2m}E_0^{3/2}T_0} \quad \text{and} \quad \Phi(T, T_0) = \int_T^{T_0}\frac{\xi d\xi}{\varphi(\xi)}. \tag{2.8}$$

This last formula demonstrates that the rate of acceleration in our model depends on the character of the de-excitation. The first term on the right-hand side describes betatron acceleration of the superthermal electrons, while the second term describes the ionization losses. To simplify our subsequent analysis, we introduce the variables

$$y = \left(\frac{E}{E_0}\right)^{3/2}\frac{T}{T_0}, \qquad Q = B\,\Phi(T, T_0), \tag{2.9}$$

so that (2.7) will take the form

$$y = 1 - Q. \qquad (2.10)$$

We can clearly see that efficient acceleration can take place only at small values of Q. For definiteness, we shall assume that

$$Q < \frac{1}{2}. \qquad (2.11)$$

Let us estimate the value of the integral on the right-hand side of (2.7) for several temperature ranges. When $T > 10^7$ K, the radiative cooling is determined by free−free transitions [12],

$$\varphi_{ff} = C_{ff}\sqrt{T},$$

and, in a fully ionized hydrogen−helium plasma with a normal set of elemental abundances,

$$C_{ff} \approx 2 \times 10^{-27} \text{ erg cm}^3/\text{s K}^{1/2}.$$

In this case, the function Φ is equal to

$$\Phi(T, T_0) = \frac{2}{3}\frac{T_0^{3/2} - T^{3/2}}{C_{ff}},$$

while the condition (2.11) reduces to

$$\frac{\sqrt{T_0}}{E_{0_{\text{keV}}}^{3/2}} < 1.18 \times 10^{-3}.$$

This last inequality cannot be satisfied for any reasonable values of the electron temperature and energy. Therefore, if the electrons are cooled by bremsstrahlung, the injection of superthermal particles is followed by their dissipation rather than acceleration. In the interval

$$2 \times 10^4 \text{ K} < T < 8 \times 10^5 \text{ K}, \qquad (2.12)$$

the de-excitation function is determined by resonant transitions of beryllium-, boron-, and lithium-like ions of carbon, nitrogen, oxygen, and neon. Its temperature dependence is not monotonic and, to first approximation, oscillates around the value $\varphi_m \approx 4 \times 10^{-22}$ erg cm^3/s [12]. At the constant value $\varphi = \varphi_m$, the acceleration condition takes the form

$$\frac{\sqrt{T_5}}{E_{100}^{3/2}\varphi_{21}} < 4. \qquad (2.13)$$

For convenience, we have introduced the notation

$$T_5 = T/10^5 \text{ K}, \qquad E_{100} = E/100 \text{ keV},$$
$$\varphi_{21} = \varphi \times 10^{21} \text{ erg cm}^3/\text{s}.$$

It follows from (2.13) that the injection of fast electrons can be followed by acceleration if their initial energy is sufficiently large. Let us consider the injection of such particles in a plasma that has already cooled.

4. INITIAL INJECTION

The injection of fast electrons occurs during the photoionization of the gas far behind the shock front. The electron energy E is equal to the difference between the energy of the ionizing photon $E_p h$ and the ionization potential P. The quantity $E_p h$ is determined by the electron temperature at the shock front T_{ef}. If there is an efficient exchange of energy between the ions and electrons, then [11]

$$kT_{\text{ef}} \approx \frac{1}{3}\mu m v^2 = 31.1\mu v_{3000}^2 \text{ keV}. \qquad (3.1)$$

Here, v is the shock velocity with respect to the cloud, $v_{3000} = \frac{v}{3000 \text{ km/s}}$, m is the atomic mass unit, and μ is the molecular weight. In a fully ionized hydrogen plasma, $\mu = 0.5$. Clouds ejected from the Wolf−Rayet star consist primarily of helium, for which $\mu = 4/3$. The velocities of the shock waves inside each cloud are determined by the density ratios. The conservation of momentum leads to the approximate relation

$$\frac{v_{\text{WR}}}{v_{\text{OB}}} \approx \sqrt{\frac{\rho_{\text{OB}}}{\rho_{\text{WR}}}}. \qquad (3.2)$$

For example, a head-on collision between a cloud from the OB star with a higher density and a cloud from the WR star with a lower density results in the generation of a shock inside the second cloud, with a velocity approximately equal to the sum of the cloud velocities. Therefore, the shock-front velocity in the direction connecting the stars can be as large as 5000 km/s in some clouds, with the temperature at the front exceeding 100 keV. We shall consider further only collisions resulting in $50 < T_{\text{ef}} < 100$ keV. The intensity of the bremsstrahlung depends on the photon energy $E_p h$ as $\exp(-E_p h/kT)$, so that about 5% of photons have energies 150−300 keV. According to (3.1), the electron energies reach $5 \times 31.1 \times 1.3 \approx 200$ keV for a shock-front velocity of $v = 3000$ km/s. Such electrons satisfy the condition for subsequent acceleration (2.13). Let us take the energy E of the injected electrons to be 200 eV.

The most efficient means to inject electrons is photoionization of the iron-ion K shell. This ionization energy is below 7 keV, considerably less than the specified injection threshold. Therefore, the energy of the primary electrons can be assumed to equal the photon energy $E_p h$. The photoionization cross-section $\sigma(E_p h)$ for $E_p h$ equal to 200 eV is about 2×10^{-24} cm^2 [13].

The rate $R(E_p h)$ of the injection of electrons with energy $E_p h$ depends on the optical depth of the ionized element. In the case under consideration, we should take into account all the ionization states of iron:

$$\tau_{\text{Fe}} = n\, z_{\text{Fe}}\, \sigma(E_p h)\, d. \qquad (3.3)$$

Here, d is the size of the cloud and z_{Fe} is the number density of iron relative to the total number of particles. The quantity $R(E_ph)$ per heavy particle is equal to the front luminosity multiplied by τ_{Fe} and divided by the number of particles in the cloud:

$$R(E_ph) = \frac{\rho_{WR}v_{WR}^3}{4}r\frac{\exp(-E_ph/kT_{ef})}{W}\frac{S}{nV}, \quad (3.4)$$

where S is the area of the cloud and V is its volume. Let us consider the meaning of this last formula, using for definiteness the parameters of the cloud ejected from the WR star. The integrated energy flux in the case of complete de-excitation is $\frac{1}{2}\rho v^3$, and half this flux is directed toward the de-excited layers. The main contribution is produced by hot regions near the front. The exponential factor describes the contribution from photons with energies above E_ph. If the gas behind the front was not, in fact, de-excited and cools adiabatically, we must introduce the correction factor

$$r = \min\left\{5, \frac{t_{dyn}}{t_{cool}}\right\}, \quad (3.5)$$

where t_{cool} is the characteristic time scale for de-excitation and t_{dyn} is the dynamical scale. We will adopt the following estimates:

$$t_{cool} = \frac{kT}{\varphi n} \approx 22\frac{\sqrt{T_9}}{n_{14}} \text{ s}, \quad (3.6)$$

$$t_{dyn} = \frac{d}{s} \approx 300\frac{d_{11}}{v_{3000}} \text{ s}, \quad (3.7)$$

where $d_{11} = d/10^{11}$ cm, $T_9 = T/10^9$ K, and $n_{14} = n/10^{14}$ cm^{-3}. We considered clouds responsible for the infrared and X-ray emission in our previous papers [8, 9]. The corresponding quantity r was close to unity. To carry out the numerical estimates below, we shall use the same parameters and assume that $r = 1$. We obtain from (3.3) and (3.4)

$$R(E_ph) = \frac{1}{2}\frac{mv^2}{2E_ph}\mu rvnz\sigma\exp(-E_ph/kT_{ef}). \quad (3.8)$$

Substituting the numerical values

$$\frac{mv^2}{2E_ph} = 0.2, \quad \mu = 1.3, \quad r = 1, \quad v = 3000 \text{ km/s},$$

$$n = 10^{14} \text{ cm}^{-3}, \quad z_{Fe} = 10^{-4},$$

which are typical for the conditions under consideration, we obtain

$$R \sim 5 \times 10^{-9} \text{ s}^{-1}.$$

Let us estimate the number of injected electrons b_{inj} per heavy particle, which is equal to the product of R and the time during which the clouds collide t_{col}. If the relative velocity of the clouds is $v_{rel} = 3000$ km/s

and their size is 10^{11} cm, we obtain $t_{col} = 300$ s. Therefore,

$$b_{inj} \approx 10^{-6}. \quad (3.9)$$

In fact, b_{inj} depends on two quantities, v_{rel} and d, each of which can take on many values. Nevertheless, we shall use below the simplest estimate (3.9).

5. THE FINAL ACCELERATION OF THE ELECTRONS

The electrons satisfying the injection condition (2.13) will experience subsequent betatron acceleration in the plasma that is compressed due to de-excitation. The acceleration of a nonrelativistic electron is described by (2.7) in the absence of bremsstrahlung losses:

$$E \sim T^{-2/3}. \quad (4.1)$$

According to (4.1), an electron injected into a gas layer with initial energy $E_ph \approx 200$ eV will reach its rest energy when the layer has cooled by approximately a factor of ten. For example, if the temperature of the layer at the time of injection is 10^6 K, the electron will become relativistic when the temperature is about 10^5 K. Let us assume, as above, that the acceleration is followed by the efficient isotropization of the electrons. In this case, the compression of the de-excited gas is followed by an increase in its energy according to the law

$$E \sim T^{-1/3}. \quad (4.2)$$

If isotropization is not able to proceed, the rate of acceleration will be greater.

The lower limit of the T_{fin} of the cooling gas temperature can be estimated as follows. It is known that the infrared radiation of the WR 140 system is due to dust at a temperature of about 1000 K (see, for example, [14]). In our previous model [9], the dust is formed by de-excitation of the gas after collisions between clouds; accordingly, let us adopt $T_{fin} = 1000$ K. Therefore, the energy of a relativistic electron increases by approximately a factor of five and is equal to about 2.5 MeV at the final stage of the acceleration process.

Thus, we shall assume that the above processes result in the generation of relativistic electrons with energies

$$E = 2.5 \text{ MeV}.$$

Further, the magnetic field intensity H can be derived from the condition that there be synchrotron radiation at 2 cm, corresponding to the circular frequency $\omega_{obs} = 9.42 \times 10^{10}$ Hz. All formulas required for the corresponding calculations can be found, for example,

in [15]. The maximum synchrotron radiation is emitted at the frequency

$$\omega_{\mathrm{m}} = 0.44\omega_{\mathrm{H}}\gamma^2,$$

where

$$\omega_{\mathrm{H}} = 1.76 \times 10^7 H \text{ Hz}, \qquad \gamma = \frac{E}{mc^2}.$$

Substituting $\omega_{\mathrm{m}} = \omega_{\mathrm{obs}}$ and $\gamma = 5$, we obtain the estimate

$$H \approx 500 \text{ G}.$$

Such a field strength can easily be generated as a result of the compression of de-excited gas behind the shock front. In any case, the corresponding energy density $H^2/8\pi \approx 10^4$ erg/cm^3 is considerably less than the dynamical pressure $\rho v^2 \approx 10^7$ erg/cm^3.

Let us estimate the number of relativistic electrons N_R required to produce the luminosity L_R of the WR 140 system at wavelength $\lambda = 2$ cm. If the distance to this object is $r \approx 1.3$ kpc, the observed flux of 20 mJy corresponds to $L_R \approx 4.5 \times 10^{19}$ erg/s Hz. After dividing this quantity by the power radiated by one electron

$$\frac{dE}{dt} = 0.92\frac{\sqrt{3}}{2\pi}\frac{e^3 H}{mc^2},$$

we obtain

$$N_R \approx 4.5 \times 10^{38}.$$

Let us compare this value with the number of particles in the stellar wind N_W. For definiteness, we shall consider a sphere with radius $a \approx 14$ AU. If the rate of outflow is $10^{-5} M_\odot$/yr, then about 1.3×10^{48} particles—hydrogen and helium ions—are concentrated in the sphere of radius a. Consequently, the observed radio intensity can be obtained if the ratio of the number of relativistic electrons to the number of heavy particles b_{obs} is equal to

$$b_{\mathrm{obs}} = \frac{N_R}{N_W} \approx 3.3 \times 10^{-10}.$$

We can see that the quantity b_{inj} characterizing the efficiency of the injection mechanism is a factor of 3×10^3 greater than the observational requirements.

In fact, such an injection rate is not excessive. Even electrons with a relatively small energy $\gamma = 5$ experience considerable magnetobremsstralung losses in the strong magnetic field ($H = 500$ G). The characteristic time scale of the radiation

$$\tau_{\mathrm{rad}} = \frac{5.2 \times 10^8}{\gamma H^2}\text{s}$$

is 4.2×10^2 s. This is substantially less than the time t_{a} required for the cloud to pass through a distance of the order of the semimajor axis of the system a. Each

cloud is a source of synchrotron radiation only when the shock wave is propagating inside it, i.e., during the interval t_{col}. Consequently, we should have

$$\frac{b_{\mathrm{inj}}}{b_{\mathrm{obs}}} \le \frac{t_{\mathrm{a}}}{\tau_{\mathrm{rad}}}. \tag{4.3}$$

Substituting numerical values, we conclude that (4.3) is satisfied for the WR 140 system.

6. CONCLUSION

The synchrotron radiation emitted by the WR 140 system could plausibly be due to a series of cloud collisions. In the same way as the X-ray emission, it represents a series of alternating bursts, each of several minutes duration. Another characteristic feature of our model is the location of the radiation source, which is the area where the clouds can collide; i.e., it is not directly related to the region near the boundary between the rarefied phases. This last fact is very important, since substantial absorption of low-frequency radio emission occurs in the vicinity of this boundary.

Along with the papers cited in the Introduction, our results represent indirect support for clumpy stellar-wind models. Such models can explain the observations of the WR 140 system in the radio, infrared, and X-ray better than models with only a rarefied wind phase.

Direct support for the clumpy-wind model would be the detection of variations in all spectral ranges. We would expect flux variations on time scales corresponding to the characteristic time for collisions between the clouds, of the order of several minutes. The amplitude of such variations depends on the number of colliding clouds at a given time. According to our estimates [8], the relative amplitude of the variations could be as large as several percent in the X-ray.

REFERENCES

1. A. M. Cherepashchuk, Peremen. Zvezdy **16** (2), 226 (1967).
2. K. V. Bychkov, Astron. Zh. **56**, 781 (1979) [Sov. Astron. **23**, 438 (1979)].
3. A. M. Cherepashchuk, J. A. Eaton, and Kh. F. Khaliullin, Astrophys. J. **281**, 774 (1984).
4. A. M. Cherepashchuk, Astron. Zh. **67**, 955 (1990) [Sov. Astron. **34**, 481 (1990)].
5. A. M. Cherepashchuk, in *Wolf-Rayet Stars: Binaries, Colliding Winds, Evolution (IAU Symposium 163)*, Ed. by K. A. van der Hucht and M. W. Peredure (Kluwer, Dordrecht, 1995), p. 262.
6. A. F. J. Moffat, L. Drissen, R. Lamontagne, and C. Robert, Astrophys. J. **334**, 1038 (1988).
7. I. I. Antokhin, T. Nugis, and A. M. Cherepashchuk, Astron. Zh. **69**, 516 (1992) [Sov. Astron. **36**, 260 (1992)].

8. O. V. Aleksandrova and K. V. Bychkov, Astron. Zh. **77** (12), 883 (2000) [Astron. Rep. **44**, 781 (2000)].

9. O. V. Aleksandrova and K. V. Bychkov, Astron. Zh. **78** (4), 327 (2001) [Astron. Rep. **45**, 281 (2001)].

10. R. L. White and R. H. Becker, Astrophys. J. **451**, 352 (1995).

11. S. P. Pikelner, *Fundamentals of Cosmic Electrodynamics* (Nauka, Moscow, 1966; NASA, Washington, 1964).

12. N. G. Bochkarev, *Foundations of Physics of the Interstellar Medium* [in Russian] (Mosk. Univ., Moscow, 1992).

13. W. M. J. Veigele, At. Data **5**, 51 (1973).

14. J. A. Hackwell, R. D. Gehrz, and G. L. Grasdalen, Astrophys. J. **234**, 133 (1979).

15. L. D. Landau and E. M. Lifshitz, *Course of Theoretical Physics,* Vol. 2: *The Classical Theory of Fields* (Nauka, Moscow, 1967; Pergamon, Oxford, 1975).

Translated by Yu. Dumin

Evolution of Wolf−Rayet Stars in Binary Systems: An Analysis of the Mass and Orbital-Eccentricity Distributions

A. M. Cherepashchuk[1] and V. G. Karetnikov[2]

[1]*Sternberg Astronomical Institute, Moscow University, Universitetskiĭ pr. 13, Moscow, 119992 Russia*

[2]*Astronomical Observatory, Odessa National University, Shevchenko Park, Odessa, 65014 Ukraine*
Received April 8, 2002; in final form, May 23, 2002

Abstract—We have undertaken a statistical study of the component mass ratios and the orbital eccentricities of WR + O close binary, detached main-sequence (DMS), contact early-type (CE), and semidetached (SD) systems. A comparison of the characteristics of WR + O systems and of DMS, CE, and SD systems has enabled us to draw certain conclusions about the evolutionary paths of WR + O binaries and to demonstrate that up to 90% of all known WR + O binaries formed as a result of mass transfer in massive close O + O binary systems. Since there is a clear correlation between the component masses in SD systems with subgiants, the absence of an anticorrelation between the masses of the WR stars and O stars in WR + O binaries cannot be considered evidence against the formation of WR + O binaries via mass transfer. The spectroscopic transitional orbital period $P_{\rm tr}^{\rm sp}$ corresponding to the transition from nearly circular orbits ($e_{\rm sp} < 0.1$) to elliptical orbits ($e_{\rm sp} \geq 0.1$) is $\sim 14^{\rm d}$ for WR + O systems and $\sim 2^{\rm d}-3^{\rm d}$ for OB + OB systems. The period range in which all WR + O orbits are circular ($1\overset{\rm d}{.}6 \leq P \leq 14^{\rm d}$) is close to the range for SD systems with subgiants, $0\overset{\rm d}{.}7 \leq P \leq 15^{\rm d}$. The large difference between the $P_{\rm tr}^{\rm sp}$ values for WR + O and OB + OB systems suggests that a mechanism of orbit circularization additional to that for OB + OB systems at the DMS stage (tidal dissipation of the orbital energy due to radiative damping of the dynamical tides) acts in WR + O binaries. It is natural to suggest mass transfer in the parent O + O binaries as this supplementary orbit-circularization mechanism. Since the transitional period between circular and elliptical orbits for close binaries with convective envelopes and ages of 5×10^9 years is $P_{\rm tr} = 12^{\rm d}4$, the orbits of most known SD systems with subgiants had enough time to circularize during the DMS stage, prior to the mass transfer. Thus, for most SD systems, mass transfer plays a secondary role in circularization of their orbits.

In many cases, the initial orbital eccentricities of the O + O binary progenitors of WR + O systems are preserved, due to the low viscosity of the O-star envelopes and the short timescale for their nuclear evolution until the primary O star fills its Roche lobe and the mass transfer begins. The mass transfer in the parent O + O systems is short-lived, and the number of orbital cycles during the early mass-transfer stage is relatively low (lower than for the progenitors of SD systems by three or four orders of magnitude). The continued transfer of mass from the less massive to the more massive star after the component masses have become equal leads to the formation of a WR + O system, and the orbit's residual eccentricity increases to the observed value. The increase of the orbital eccentricity is also facilitated by variable radial mass loss via the wind from the WR star in the WR + O system during its motion in the elliptical orbit. The result is that WR + O binaries can have considerable orbital eccentricities, despite their intense mass transfer. For this reason, the presence of appreciable eccentricities among WR + O binaries with large orbital periods cannot be considered firm evidence against mass transfer in the parent O + O binary systems. Only for the WR + O binaries with the longest orbital periods (4 of 35 known systems, or 11%) can the evolution of the parent O + O binaries occur without filling of the Roche lobe by the primary O star, being governed by radial outflow in the form of the stellar wind and possibly by the LBV phenomenon, as in the case of HD 5980. © *2003 MAIK "Nauka/Interperiodica".*

1. INTRODUCTION

It is currently believed that Population I Wolf−Rayet stars are the naked helium cores of once massive stars that have lost their hydrogen envelopes, either as a result of mass transfer in close binary systems [1−3] or due to the intense outflows of stellar wind from single massive stars [4, 5]. According to [1−3], well-known WR + O binaries [6−9] formed from massive O + O binary systems with initial component-mass ratios close to unity as a result of quasiconservative mass transfer between the components, usually at the B evolution stage [10],

when the more massive O star, with its inert helium core and hydrogen shell source, fills its Roche lobe. WR + O binaries can be considered evolutionary progenitors of massive X-ray binary systems [1, 3, 11] containing neutron stars and black holes.

Recently, the role of mass loss by massive stars and the significance of stellar-wind collisions in the evolution of close binaries have been subjects of discussion [12−14]. Moffat [12] suggested that the formation and evolution of WR stars in massive close binaries takes place exclusively via radial mass loss by the massive star in the form of stellar wind, without this star filling its Roche lobe and the associated outflow through the inner Lagrange point L_1. This hypothesis is based on the fact that known WR + O binaries demonstrate a relation between the component-mass ratio, $q = M_{WR}/M_O$, and the spectral subtype of the WR star: q gradually decreases from late to early WR subtypes.

It was suggested in [12] that there was no mass transfer in the parent $O_1 + O_2$ system, so that the observed decrease of q with decreasing mass of the WR star in WR + O binaries was due to radial mass loss via the wind from the initially massive star, O_1, with the mass of the companion star, O_2, being nearly constant. In this picture, binarity plays virtually no role in the formation of the WR star, which forms via the scenario of Conti [5]. In its current form, this scenario can be represented by the following scheme (cf., for instance, [15]):

$$O \rightarrow Of \rightarrow WNLha \rightarrow WN7(\rightarrow WNE) \rightarrow WC \rightarrow SN$$
$$\text{for } M_i > 60M_\odot,$$

$$O \rightarrow Of \rightarrow LBV \rightarrow WN9\text{-}11 \rightarrow WN8 \rightarrow WNE \rightarrow$$
$$WC \rightarrow SN \text{ for } 40M_\odot \lesssim M_i < 60M_\odot,$$

$$O \rightarrow Of \rightarrow RSG \rightarrow WN8 \rightarrow WNE \rightarrow WC \rightarrow SN$$
$$\text{for } 25M_\odot < M_i \lesssim 40M_\odot,$$

where LBV and RSG denote the luminous blue variable and red supergiant stages. As usual, the abbreviations WNL, WNE, and SN denote late WN stars, early WN stars, and supernovae. We emphasize right from the start that this scenario is not able to explain the origin of WR + O binaries with short orbital periods, $P \leq 3^d$: it is known [16] that the orbital period of a binary increases in the course of radial mass loss via a high-speed wind. Seven of 35 WR + O binaries with measured radial-velocity curves have short periods, which is ~20% of all these systems (see table).

At the same time, the existence of WR stars in very long-period WR + O binary systems ($P \cong$ 7−14 years) and even in visual binary and multiple systems [9] shows that Moffat's hypothesis [12]

should be taken seriously, since possibilities for radius increases during nuclear evolution are very limited for the most massive ($M > 60M_\odot$) stars, due to their intense mass loss via their stellar winds [17]. The problem of the relative numbers of O and WR stars, as well as of WN and WC stars, in galaxies with different metallicities (see, for example, [18]) also requires a comparison of the roles of stellar wind and mass exchange in the evolution of close binary systems.

According to Moffat [12] and Maeder [18], the principal pieces of evidence against the formation of WR stars in massive close binary systems due to mass transfer are the following.

(1) There is no anticorrelation between the masses of the WR and O stars in WR + O binaries, which, according to [12, 18], should exist in the case of conservative mass transfer.

(2) There are systems with elliptical orbits among WR + O binaries with large orbital periods, whereas the orbits of semidetached binary systems with subgiants that have passed through a mass-transfer stage are always circular (also cf. [19]).

However, it was shown in [20, 21] that no anticorrelation between the masses of the subgiants and of their main-sequence (MS) companion stars was observed even in semidetached close binaries with subgiants, where there is no doubt that mass transfer had occurred. In addition, De Greve [22] noted that, in contrast to systems with subgiants, the mass-transfer time scale for the massive close-binary progenitors of WR + O binaries, which is close to the thermal time scale, can be shorter than the time needed for the original elliptical orbit to become circular due to the mass transfer. De Greve [22] and Vanbeveren [23] suggested that most OB + OB binaries experience a stage of mass transfer, with the formation of a WR star. This is supported by a preliminary analysis of the orbital-eccentricity distributions for WR + O binaries and classical detached main-sequence systems that are eclipsing binaries [20].

2. THE OBSERVATIONAL MATERIAL

We will compare the component masses M_i and orbital eccentricities e for WR + O binaries, classical detached main-sequence (DMS) systems, contact early-type (CE), and semidetached (SD) close binaries. The comparison of WR + O binaries and SD close binaries, in which mass transfer has certainly already occurred, is especially important. Subgiants formed in SD systems (via mass transfer during the A evolutionary stage [10], on the thermal time scale) fill their Roche lobes, but their mass loss via the inner Lagrange point L_1 proceeds on the nuclear evolutionary time scale, i.e., very slowly. Thus, evolutionary

Parameters of WR + O binaries (from [9], [6], and [8])

System	Spectral type	$M_{\mathrm{WR}}, M_\odot$	$M_{\mathrm{O}}, M_\odot$	P, days	e
HD 63099	WC5 + O7	9	32	14.305	0.0
γ^2Vel	WC8 + O7.5 III–V	9.5	30	78.53(1)	0.33 ± 0.01
HD 90657	WN5 + O4–6	19	37	8.2546(1)	0.04 ± 0.03
HD 92740	WN7h + O9 III–V	55	21	80.336(1)	0.60 ± 0.01
HD 94305	WC6 + O6–8	16	34	18.82	0
HD 94546	WN4 + O8 V	4	9	4.8306(1)	0.0
HD 97152	WC7 + O7 V	14	23	7.886(3)	0.0
HDE 311884	WN6 + O5 V	51	60	6.2393(1)	0
HD 152270	WC7 + O5–8	11	29	8.8908(5)	0
CV Ser	WC8d + O8–9 IV	13	27	29.704(2)	0.19 ± 0.03
HD 186943	WN3 + O9.5 V	17	36	9.5550	0.07 ± 0.04
HD 190918	WN5 + O9 I	17:	34:	112.4(2)	0.39 ± 0.07
V444 Cyg	WN5 + O6 III–V	9.3	27.9	4.212435	0.04 ± 0.01
HD 193793	WC7pd + O4–5	27:	60:	2900 ± 10	0.85 ± 0.01
CX Cep	WN4 + O5 V	20	28.3	2.12687	0
HD 211853	WN6/WCE + O6 I(+WN + O)	15	27	6.6884(+3.4696)	0.0 + 0.000
CQ Cep	WN6 + O9 II–Ib	24	30	1.6412436	0.01 ± 0.01
B22	WC6 + O5–6 V–III:	12:	35:	14.926	0.17
B32	WC4 + O6 V–III:	5	30	1.91674	0
AB8	WO4 + O4 V	14	52	16.644	0.19
HD 5980	WN4 + O7 I	8:	27:	19.266	0.49
AB6	WN3 + O7	8	47	6.681	0
HD 193928	WN5 + O5 V–III	45	30	21.6895(3)	0.02 ± 0.03

System	Spectral type	$f_{\mathrm{WR}}(M), M_\odot$		P, days	e
HD 62910	WN7/WCE + ?	0.20		85.37	0.4
HD 192641	WC7pd + O9	12.1		4765 ± 50	> 0.12
HD 193077	WN5o + B?	4.7(8)		1538.0	0.28 ± 0.07
AS422	WN + WC + ?	7.7 :		22.0	0
B26	WN7 + ?	2.4		1.9075	0
B65	WN7 + ?	4.2		3.0032	0
B72	WN6 + B1 Ia	3.8		4.3092	0
B82	WN6 + O5	0.02		4.377	0
B86	WNL/Of	1.6 :		52.7 :	0
B87	WN6 + ?	0.10		2.7596	0
B90	WN7+?	1.4 :		25.17 :	0
HD 16523	WC5+?	0.007−0.016		2.4096	0.0

changes of the characteristics of subgiants in SD systems can be neglected.

We use data from the catalogs of characteristics of eclipsing and spectroscopic binaries [8, 9, 24–29], which contain reliable parameters for WR + O, DMS, CE, and SD binary systems. The data for 23 SB2 WR + O systems, 12 SB1 WR + O systems, 61 DMS, 88 CE, and 82 SD systems were used. Analysis of the orbital eccentricities for close binaries of different types is especially important.

The distributions of the orbital eccentricities as a function of orbital period and the combined mass of the close binary can be used as additional evidence for or against mass transfer through the inner Lagrange point L_1 in close binary systems [19]. The table contains data on the masses and orbital eccentricities of SB2 and SB1 WR + O binaries taken from [6, 8, 9]. The binarity effects under study appear to be independent of metallicity, and we will use data for Galactic WR stars as well as WR stars in the Large and Small Magellanic Clouds.

We did not include data on two peculiar WR binaries [9]: Cyg X-3 (WN(3−7) + C, $P \cong 4{.}^{\rm h}8$, $e_{\rm sp} = 0$) and HD 197406 (WN8h + B3IV/C, $P \cong 4{.}^{\rm d}3$, $e_{\rm sp} = 0.08 \pm 0.03$). The Cyg X-3 system has undergone secondary mass transfer with a common envelope stage [30], and the companion is a relativistic object. For this reason, its characteristics are very different from the parameters of typical WR + O binaries. The HD 197406 system either has a relatively low-mass B star as the companion or has passed through a stage of secondary mass transfer and has a black hole companion [31]. Because of this system's uncertain status, we did not include it in the table or our statistical analysis. We also excluded the WR + O binary HD 320102 (WN5 + O7, $P \cong 12{.}^{\rm d}6$), since its component masses are unusually low ($M_{\rm WN5} = 2.3 M_\odot$, $M_{\rm O7} = 4.1 M_\odot$) [9], probably due to overestimation of the orbital inclination ($i = 85°$).

Uncertain values in the table are followed by colons (:). The values given as $e = 0.0$ were derived from analyses of radial-velocity curves, while those given as $e = 0$ were postulated during the interpretation of the radial-velocity curves. Comparison of data from [9] and [6, 8] demonstrates that the mean uncertainty of the masses of the WR stars in the WR + O binaries is ∼30%, though discrepancies in the mass of a single WR star can reach a factor of two in some cases (γ^2Vel, HD 152270, HD 94546; cf. also [8]).

For DMS, CE, and SD systems, we will use photometric orbital eccentricities $e_{\rm ph}$ derived from analyses of their eclipsing light curves. The $e_{\rm ph}$ values are most reliable, whereas the spectroscopic orbital

eccentricities derived from the radial-velocity curves, $e_{\rm sp}$, are often spurious due to selective absorption of light from the components of the close binaries by gas flows in the system. For example, many SD systems with subgiants have appreciable $e_{\rm sp}$ values (V448 Cyg: $e_{\rm sp} = 0.04$; RS Sgr: $e_{\rm sp} = 0.04$; GT Cep: $e_{\rm sp} = 0.06$; U Sge: $e_{\rm sp} = 0.03$; TX UMa: $e_{\rm sp} = 0.08$; IZ Peg: $e_{\rm sp} = 0.06$; TU Mon: $e_{\rm sp} = 0.02$; QS Aql: $e_{\rm sp} = 0.06$), whereas all these systems have $e_{\rm ph} = 0$ [29, 32]. We must use spectroscopic orbital eccentricities for the WR + O binaries because of the low number of systems showing sufficiently deep eclipses. Taking into account this discussion and the $e_{\rm sp}$ and $e_{\rm ph}$ data for SD systems, we consider spurious all $e_{\rm sp}$ values for WR + O binaries not exceeding 0.1. Thus, we assume that the orbits of WR + O binaries with $e_{\rm sp} < 0.1$ are essentially circular.

For comparison with the data for the WR + O systems, we also used the spectroscopic orbital eccentricities for 174 OB + OB binaries (SB1 or SB2) from the eighth "Catalogue of the Orbital Elements of Spectroscopic Binary Systems" by Batten *et al.* [29]. Most of the combined masses for these systems, $M_1 + M_2$, exceed $10 M_\odot$, in accordance with the mass range for the WR + O binaries. As for the WR + O binaries, we will consider many of the eccentricities $e_{\rm sp} < 0.1$ for these OB + OB systems to be spurious. We will also use the results of our statistical studies of the characteristics of eclipsing binaries [21].

3. CORRELATIONS BETWEEN THE MASSES OF THE COMPONENTS IN WR+O, DETACHED MS, CE, AND SD SYSTEMS

Morton [33], Smak [34], and Kippenhahn and Weigert [10] carefully considered the component mass ratios for binary systems, believing, with good reason, that effects influencing the component mass ratios of close binaries associated with mass transfer are key for tests of evolutionary theories for close binaries. The mean component mass ratio for close binary systems, $q = M_2/M_1$, has been considered in many studies, and is close to $q = 0.8$ for DMS systems and to $q = 0.3$ for low-mass and intermediate-mass SD systems [21], with the difference being quite significant. Observational selection effects are a key problem in studies of close-binary component mass ratios (see, for instance, [35]) and can strongly distort the observed ratios. The masses of close-binary components are correlated due to the observing conditions: systems with mass ratios close to unity are often observationally preferred in mass studies. This is especially true for DMS and CE systems. The evolved components of SD systems and WR + O binaries (subgiants and WR stars) display considerable excess luminosities for their masses, so that, when
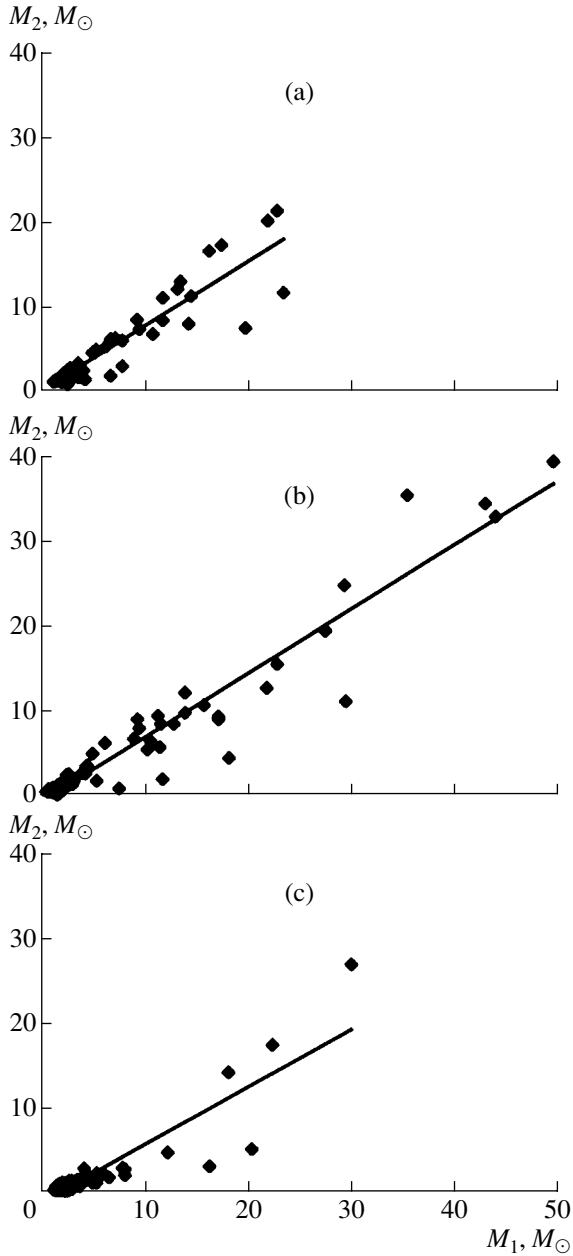
Fig. 1. Relations between the component masses for (a) DMS, (b) CE, and (c) SD systems of any mass.

the component luminosity ratio is close to unity, it is often possible to measure masses for the evolved components that are much lower than the masses of their companions. It was noted in [8] that observational selection effects are weak for WR + O systems with low- and moderate-mass WR stars ($M_{\mathrm{WR}} = 5-20M_\odot$) and are appreciable for the most massive WR stars. Various observational selection effects have been analyzed; for example, it was demonstrated in [36] that the observed distribution of mass ratios,

$$q = \frac{M_2}{M_1},$$ in SD systems ranged from ~0.1 to ~0.7,

with a pronounced maximum near $q \cong 0.2-0.3$. Note that measurements of component masses in close binaries during the last two decades have usually been based on CCD data, rather than photographic spectra. Such data enable the construction of reliable radial-velocity curves for both components of a close binary system, even when their luminosities (and masses) differ strongly (by up to a factor of ~10). This considerably reduces the influence of observational selection effects on the derived component masses.

It was found in [37] that, for SD systems, the larger the mass of the primary, M_1, the larger the ratio $q = M_2/M_1$ of the subgiant mass M_2 to M_1. A similar relation, though with the opposite sign, is also observed for the WR + O systems (see above): the larger the mass of the evolved WR star, the larger the mass ratio $q = M_{\mathrm{WR}}/M_{\mathrm{O}}$. Moffat [12] explains this relation for the WR + O systems as resulting from radial mass loss via the stellar wind from the WR star, with the mass of the O star being constant. The required mean rate of mass loss by the WR star is $\langle \dot{M}_{\mathrm{WR}} \rangle = 5 \times 10^{-5} \, M_\odot/\mathrm{yr}$ [12]. Another possible interpretation of this relation in a mass-transfer model was suggested by De Greve [22]: the greater the mass loss via the wind from the primary O_1 star in the initial $O_1 + O_2$ system, the lower the mass of this star during the mass-transfer stage, including its final stage and the formation of the WR star.

Figure 1 presents relations between the component masses for (a) DMS, (b) CE, and (c) SD systems with any known masses. In all cases, a clear correlation between the component masses is observed. The correlation is highly significant: the correlation coefficients are 0.84, 0.92, and 0.80, respectively, for the DMS, CE, and SD systems. These high correlation coefficients indicate that the role of observational selection effects is not large. In fact, if there were actually a large scatter in the component mass ratios for the DMS systems, with the observed correlation in Fig. 1a being due to the observational selection effects discussed above, we would expect a significant scatter of the data points about the relation $M_1 = f(M_2)$ and a correlation coefficient significantly lower than unity. In our case, the correlation coefficient is close to unity, testifying to the reality of the correlations in Fig. 1.

Figure 2 presents relations between the component masses for (a) WR + O, (b) CE, and (c) SD systems. Here, we selected only those CE and SD systems with combined component masses $M_1 + M_2 > 10M_\odot$, corresponding to the range of combined masses for the WR + O systems. Data for WR + O systems within the entire range of known masses were used. There is no anticorrelation between the masses of the WR and O stars in the WR + O systems, and instead a hint of a weak correlation,
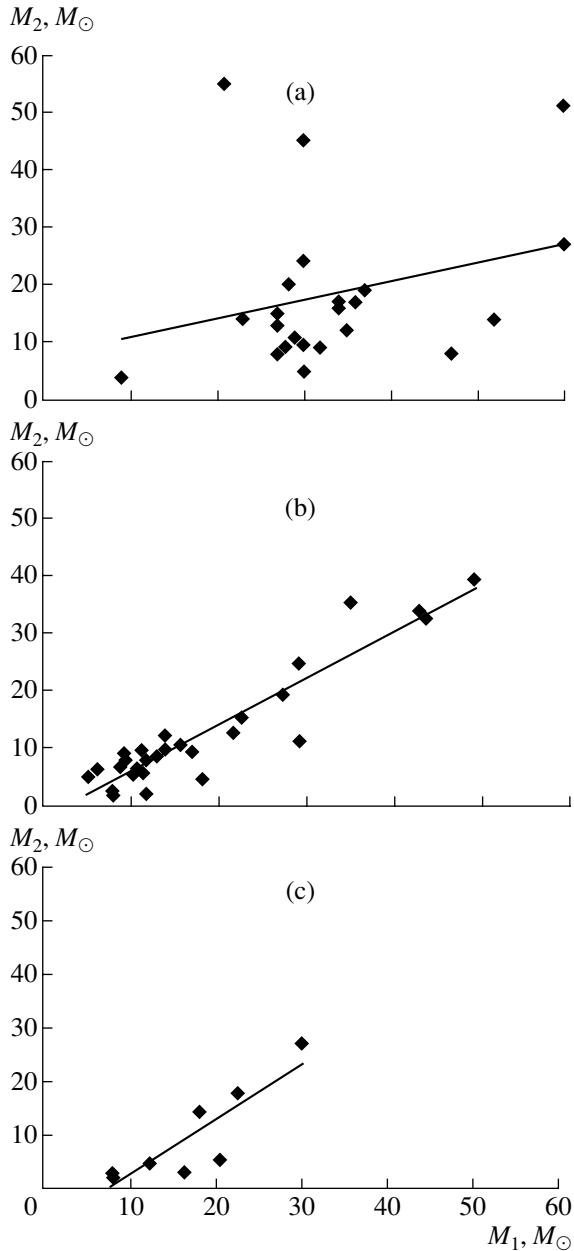
Fig. 2. Relations between the component masses for (a) WR + O, (b) CE, and (c) SD systems. CE and SD systems with masses $M_1 + M_2 > 10M_\odot$ were selected.

Fig. 3. Relations between the component masses for (a) WR + O, (b) CE, and (c) SD systems. CE and SD systems with masses for each of the components $> 10M_\odot$ were selected.

with a correlation coefficient $\sim$0.07. In this case, the correlation coefficient is too low to rule out the possibility that the weak correlation between the masses of the WR and O stars is due to observational selection effects. A firm correlation, rather than an anticorrelation, is also observed between the component masses in the CE and SD systems (correlation coefficients of $\sim$0.87 and 0.76, respectively).

Figure 3 presents relations between the component masses for (a) WR + O, (b) CE, and (c) SD systems. We selected only those CE and SD sys-
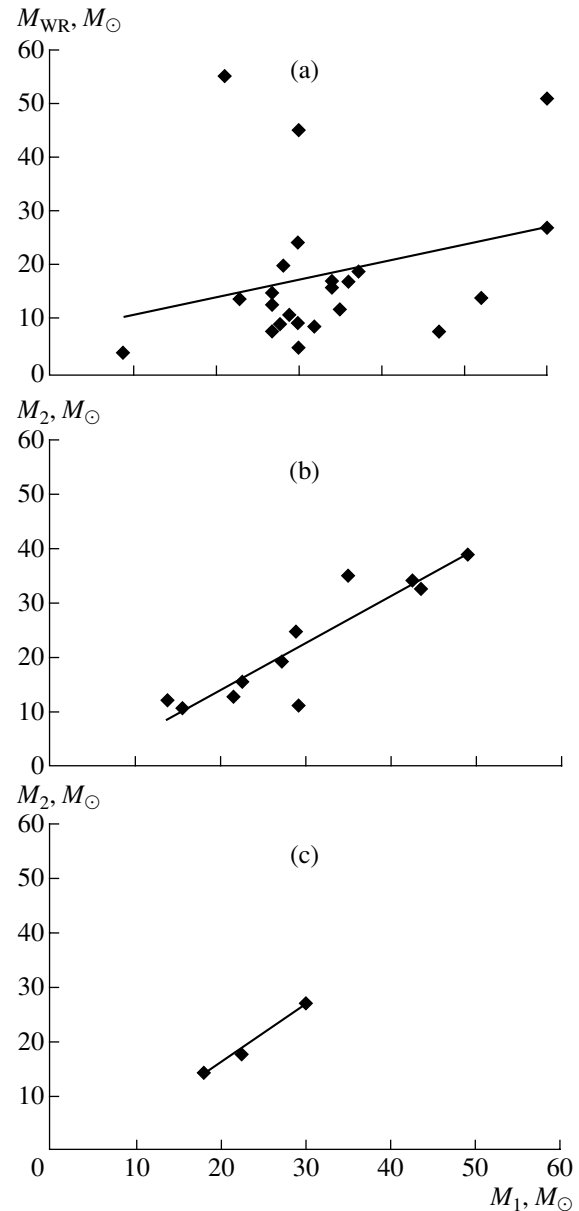
tems with masses for each of their components $M_i > 10M_\odot$. These are the most massive CE and SD systems, which best correspond to the WR + O systems. As before, we used data for WR + O systems within the entire range of known masses. In this case as well, there is a weak correlation between the masses of the WR and O components of the WR + O systems, and a correlation (rather than anticorrelation) between the component masses of the CE and SD systems (correlation coefficients of 0.82 and 0.99, respectively).

Thus, using extensive observational material on

eclipsing systems, we confirm that, even for SD systems with subgiants that have certainly passed through a mass-transfer stage, we observe a correlation rather than an anticorrelation between the masses of the subgiants and of the MS stars. As noted in [21], if the role of observational selection effects is relatively small (and, in our case, the high correlation coefficients support this assumption), this correlation reflects two facts.

(1) There is a large scatter of initial combined masses for close binaries at the evolutionary stage preceding the mass-transfer stage (the DMS stage).

(2) The initial mass ratio q_0 of the components of close binaries in the stage preceding the mass-transfer stage is close to unity. Analysis of the DMS systems (Fig. 1a) suggests that this value is $q_0 \cong 0.8$.

Mass transfer in close binaries cannot "beat" the influence of the large scatter in the initial combined masses (Fig. 1c). Therefore, a correlation, rather than an anticorrelation, between the masses of the subgiant and the MS star is observed for SD systems that have completed the mass-transfer stage, but with a lower correlation coefficient than for the DMS systems and with a lower mean value for the component mass ratio q.

Let the initial component mass ratio for the parent DMS system be $q_0 = M_2/M_1$, with M_1 being the mass of the more massive star. Let the mass of the subgiant after conservative mass transfer (originally the more massive star) in the corresponding SD system be $M_1' = kM_1$, where $0 \leq k \leq 1$. Then, in the case of conservative mass transfer and a reversal of which component is the more massive, the mass of the now more massive component, which was the MS star in the SD system formed, is $M_2' = M_2 + M_1(1 - k)$. The resulting mass ratio in the SD system is

$$q' = \frac{M_1'}{M_2'} = \frac{kM_1}{M_2 + M_1(1 - k)} = \frac{k}{q_0 + 1 - k}. \quad (1)$$

The value of q' decreases from $q' = 1/q_0$ to $q' = 0$ when k decreases from 1 to 0, so that the observed value, $q' = 0.3$ (the mean mass ratio for the moderate-mass SD systems), corresponds to $k = 0.4$ (for $q_0 = 0.8$)—apparently quite a reasonable value.

The same two factors as for the SD systems (see above) are probably operating in the WR + O systems, with the only difference being that the scatter of the initial masses in the parent massive DMS systems (O + O binaries) could be considerably larger. In addition, the WR star that forms after the mass transfer in an O + O system experiences strong mass loss via the stellar wind (in contrast to the subgiants in SD systems). The result is that, as for the SD systems, we observe a weak correlation (rather than anticorrelation) between the masses of the WR and

O components of WR + O systems, with the correlation coefficient being much lower than for the SD systems and with the mean mass ratio being $q = M_{\mathrm{WR}}/M_{\mathrm{O}} \cong 0.5$. However, if the weak correlation between the masses of the WR and O stars in the WR + O systems is due to observational selection effects, we can immediately conclude that an anticorrelation is not ruled out by the observations. The existence of a correlation between the component masses for the CE systems (Figs. 1b, 2b, 3b), which are in an early stage of mass transfer further supports our conclusions (in the case of large combined masses, some of the CE systems may be the immediate progenitors of WR + O systems).

All these facts indicate that the absence of an anticorrelation between the WR and O component masses in WR + O binaries cannot be considered evidence against the occurrence of mass transfer in the massive O + O close binaries that are the progenitors of WR + O systems.

4. POSSIBLE MECHANISMS FOR ORBITAL-ECCENTRICITY VARIATIONS IN CLOSE BINARIES

Among the 35 WR + O binaries with measured orbital eccentricities (see the table), 10 systems ($\sim 30\%$) have spectroscopic orbital eccentricities $e_{\mathrm{sp}} > 0.1$. Thus, 70% of the WR + O binaries with e_{sp} values have nearly circular orbits, a fact that can naturally be attributed to the effects of mass transfer in massive O + O systems. Let us briefly discuss the possible origins of variations in the orbital eccentricities of close binaries (for more detail see, for example, [38−40]).

Two main mechanisms for orbital circularization operate during the DMS stage in close binaries [41, 42]. In the case of solar-type stars ($M < 1.5-1.6M_\odot$) with strong convective envelopes, the orbits are circularized by the very efficient turbulent dissipation of the energy of the orbital motion in equilibrium tides. Due to the viscosity of the material in the stellar envelope, the equilibrium tidal humps are located along a line inclined by some angle to the line connecting the component centers, rather than directly along this central line. As a result, the rotational momentum and rotational energy of the star are transferred back and forth between the orbit and the star. The efficiency of the mechanism depends strongly on the stellar radius R as a fraction of the orbital semi-major axis a (the time scale for the orbital circularization is $t_{\mathrm{cir}} \sim \left(\dfrac{R}{a}\right)^{-8}$) and depends only weakly on the specific component masses [41].

The main mechanism for orbital circularization in close binaries with massive ($M > 1.6M_\odot$) stars with

radiative envelopes and convective cores is the dissipation of the energy of the orbital motion in dynamical tides with radiative damping [41]. In this case, the tidal potential forms gravitational waves in the star, which are not standing waves, since the radiative-cooling time in the star's outer layers is comparable to the tidal period, leading to damping of the dynamical tides and energy dissipation. This results in a transfer of angular momentum back and forth between the rotating stars and the orbital motion. In this case, the time scale for the orbital circularization depends strongly on the star's relative radius $\left(t_{\mathrm{circ}} \sim \left(\frac{R}{a}\right)^{-10.5}\right)$, making the efficiency of orbital circularization via this mechanism many orders of magnitude lower than for stars with convective envelopes [41]. For example, the orbital-circularization time scale, t_{circ}, for a star with a mass of $1M_\odot$ (convective envelope) in a close binary with semi-major axis $a = 10R_\odot$ is 2.5×10^8 years, whereas we find, for a stellar mass of $2M_\odot$ (radiative envelope) in a close binary with $a = 10R_\odot$, $t_{\mathrm{circ}} = 1.8 \times 10^{10}$ years [38], which is an order of magnitude longer than the nuclear-evolution time for such a star.

The relative separations of components of close binaries with equal masses, for which the orbital circularization time is one-quarter of the stars' main-sequence life times, are [38, 41] $\left(\frac{a}{r}\right)_{\mathrm{circ}} = 32.76$ for $M = 0.5M_\odot$, 20.36 for $M = 1M_\odot$, 14.71 for $M = 1.2M_\odot$, 3.94 for $M = 1.6M_\odot$, 3.92 for $M = 2M_\odot$, 3.88 for $M = 5M_\odot$, 3.91 for $M = 7M_\odot$, and 3.98 for $M = 10M_\odot$. Thus, for massive stars with radiative envelopes, the critical relative stellar radius R/a for which an elliptical orbit has sufficient time to circularize over the star's nuclear evolution depends only weakly on the star's mass and is ~ 0.25.

It is important that the rate of circularization of an elliptical orbit in a close binary is different when the axial and orbital rotation deviate from synchronism. For significant nonsynchronism, when $\Omega/\omega > 2.007$, where Ω and ω are the angular velocities of the axial and orbital rotation, the orbital eccentricity increases rather than decreases during the radiative dissipation in dynamical tides [41]. A similar effect of increasing orbital eccentricity occurs in the case of nonsynchronous equilibrium tides and viscous (turbulent) dissipation: the corresponding critical value of the nonsynchronism is $\Omega/\omega = 1.636$ [41, 43].

According to [41], in close binaries, the synchronization of the component axial and orbital rotation due to tidal effects occurs earlier than the orbital circularization. The synchronization time depends on the star's relative radius $\frac{R}{a}$ as $t_{\mathrm{cync}} \sim \left(\frac{R}{a}\right)^{-6}$ or $t_{\mathrm{cync}} \sim \left(\frac{R}{a}\right)^{-8.5}$, respectively, for stars with convective and radiative envelopes [41].

Massive OB stars in the DMS stage, as well as WR stars in binary systems, lose mass via their stellar winds, which also brings about changes in the orbital eccentricity (for example, see [39]). The star's mass-loss rate via a symmetrical wind, $\dot{M}$, increases at the orbit periastron. According to [39], this leads to an increase in the orbital eccentricity in accordance with the law

$$\frac{1+e}{1+e_0} = \left(\frac{M_0}{M}\right)^{\beta},$$

where M_0 and e_0 are the initial combined mass and orbital eccentricity, and the parameter $\beta \lesssim 1$ is the ratio of the additional mass lost via the wind at periastron to the entire amount of mass lost during an orbital period. The variations of e due to this effect are especially significant for systems with stars with large radii, such as binaries containing asymptotic-giant-branch stars [39]. In the case of massive WR + O binaries with high-velocity winds, the radii of the hydrostatic cores of their WR stars are usually much smaller than their Roche lobes, so that β is comparatively low.

As soon as one of the components fills its Roche lobe, the close binary commences mass transfer through the inner Lagrange point L_1. It follows from the above (see also [38]) that, in many cases, the tidal friction in the stellar envelopes completes the circularization of the elliptical orbit prior to the Roche lobe filling and mass transfer in the close binary. However, if circularization was not complete, mass transfer will take place in the elliptical orbit, and the mass-transfer rate will increase when the mass-losing star comes to the periastron of its orbit. The variation of the orbital eccentricity δe due to the enhanced mass transfer at periastron can be estimated using the formula [39, 40]

$$\delta e = 2\delta \mathrm{M}_{\mathrm{tran}} \left(\frac{1}{M_1} - \frac{1}{M_2}\right)(e + \cos\theta),$$

where M_1 and M_2 are the component masses and θ is the polar angle of the star's radius vector ($\theta = 0$ at periastron). Since the mass transfer is enhanced at periastron ($\delta M_{\mathrm{tran}} > 0$), we see that δe is positive (the eccentricity increases) if $M_1 < M_2$, and δe is negative (the eccentricity decreases) when $M_1 > M_2$. Thus, if the mass transfer commenced in an elliptical orbit during an early stage in the transfer, when the more massive star flows onto the less massive star, the orbit is circularized, but during the subsequent mass transfer, after the reversal of the components'
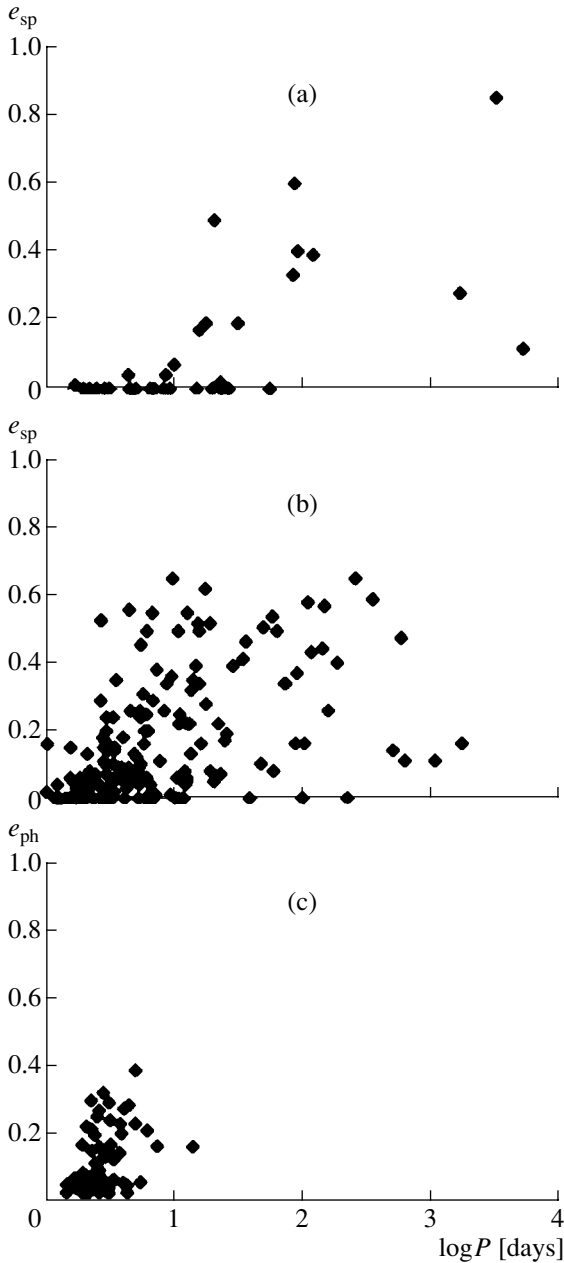
Fig. 4. Dependence of orbital eccentricity e on orbital period for (a) WR + O and (b) OB + OB systems from [29] and (c) for close binaries in the LMC.

a distance $\sim 6a$ from the binary system (where a is the semi-major axis of the initial orbit) [45]. In this case, the eccentricity increases at a rate [45]

$$\dot{e} \cong 1.9 \times 10^{-3} \left(\frac{M_{\mathrm{disk}}}{M} \right) \left(\frac{2\pi}{P} \right),$$

where M_{disk} is the mass of the relict disk at distances of up to $\sim 6a$ from the system.

Thus, if M_{disk} is sufficiently high, the resonance interaction of the young binary with the circumbinary disk can lead to the formation of an elliptical orbit with a considerable eccentricity. Rapid axial rotation of a young component of such a newly formed close binary can lead to considerable nonsynchronism of the axial and orbital motions in the binary. In this case, the transfer of energy and rotational momentum from this star to the orbit can also increase the orbital eccentricity (see above).

After synchronization of the axial and orbital motions and dissipation of the outer envelope, the tidal dissipation of the orbital energy of the system's components begins to operate, efficiently circularizing the orbit. The most efficient orbital circularization occurs when a young solar-type star has not yet reached the main sequence and is undergoing a fully convective stage on the Hayashi track [46]. The combined action of the three discussed mechanisms (resonance interaction of a young close binary with its relict disk, the dissipation of the energy of a young star's rapid rotation, and tidal dissipation during the synchronism stage) leads to the observed orbital eccentricities of DMS systems.

5. COMPARISON OF ORBITAL ECCENTRICITIES FOR WR + O BINARIES AND DMS, CE, AND SD SYSTEMS

Short-period binary systems are known to usually have circular orbits, whereas the orbits of long-period binaries are mainly elliptical [47]. This difference is especially evident for binaries containing components with late spectral types with convective envelopes, whose matter has a high turbulent viscosity [48]. It is usually believed that the orbital circularization in such DMS systems is due to the tidal dissipation of the components' orbital energy (see, for example, [41]). This mechanism can be efficient during the early evolution of a close binary, when its components have not yet reached the main sequence and possess extended convective zones on Hayashi tracks [46], or during the long stay of the components on the main sequence [41]. In the first case, the transition period P_{tr} corresponding to the transition from circular to elliptical orbits is $P_{\mathrm{tr}} = 7^{\mathrm{d}}2 - 8^{\mathrm{d}}5$ [46] and is virtually independent of the time spent by the components on the main sequence. In the second case, as noted

roles, the mass flow from the less massive to the more massive star can lead to an increase of the orbital eccentricity (if the orbit did not have enough time to become completely circular during the initial mass-transfer stage) [39].

Let us now consider the initial conditions for the formation of close binaries with very elliptical orbits. Artymowicz and Lubow [44] discuss a mechanism for the formation of an elliptical orbit in a young close binary due to resonance interactions between the binary and a circumbinary disk of primordial matter located

in [49], the value of P_{tr} depends on the age of the close binary at the DMS stage, so that the value of P_{tr} can be used to estimate the age of an ensemble of close binaries with the same evolution time.

For close binaries containing components with convective envelopes, the theory predicts a relation between the orbital circularization time T_{cir} and the transition period P_{tr}: $T_{cir} \sim P_{tr}^{16/3}$ [41], $T_{cir} \sim P_{tr}^{49/12}$ [50], or $T_{cir} \sim P_{tr}^{10/3}$ [49]. Observations show that P_{tr} does depend on the ensemble age, testifying that a significant amount of orbital circularization takes place during the stay of the close-binary components on the main sequence. For example, $P_{tr} = 5\overset{d}{.}6$ for close binaries in the comparatively young Hyades and Coma open clusters, with ages of $\sim 6 \times 10^8$ years [51], $P_{tr} = 12\overset{d}{.}4$ in the cluster M 67, with an age of 5×10^9 years, and P_{tr} is the highest for close binaries of the Galactic halo, with ages of $\sim 15 \times 10^9$ years: $P_{tr} = 18\overset{d}{.}7$ [52]. The mass transfer in close binaries leads to efficient circularization of their orbits, and no SD systems with orbital eccentricities $e \neq 0$ are known [53, 54]. In addition, it follows from these data that, since the ages of solar-type SD systems with subgiants are several billion years and their components possess strong convective envelopes, orbital circularization in such SD systems could already be finished during the DMS stage (for systems with periods $P < 12^d - 15^d$). Therefore, mass transfer in such SD systems occurred in the presence of nearly circular orbits, and was not important for the orbital circularization. The situation is quite different for systems with OB components: their ages are lower by two or three orders of magnitude, and the component envelopes are radiative and have low viscosities, mainly due to radiative damping of the dynamical tides [41].

We compare the $e(P)$ distributions for WR + O binaries and for OB + OB binaries with combined masses $M_1 + M_2 > 10 M_\odot$. This range of combined masses, $M_1 + M_2 > 10 M_\odot$, corresponds to that for the WR + O systems, so we can assume that the ages of the WR + O and OB + OB systems are comparable. The mechanism for tidal dissipation of the orbital energy can also be considered to be the same for the WR + O and OB + OB systems (radiative damping of the dynamical tides), since the components of these systems are massive, hot stars without convective envelopes. We can assume that, compared to solar-type close binaries, the tidal dissipation is much less efficient for WR + O and OB + OB systems, so that we can neglect orbital circularization during the DMS stage for the OB + OB systems in a number of cases (in contrast to SD systems).
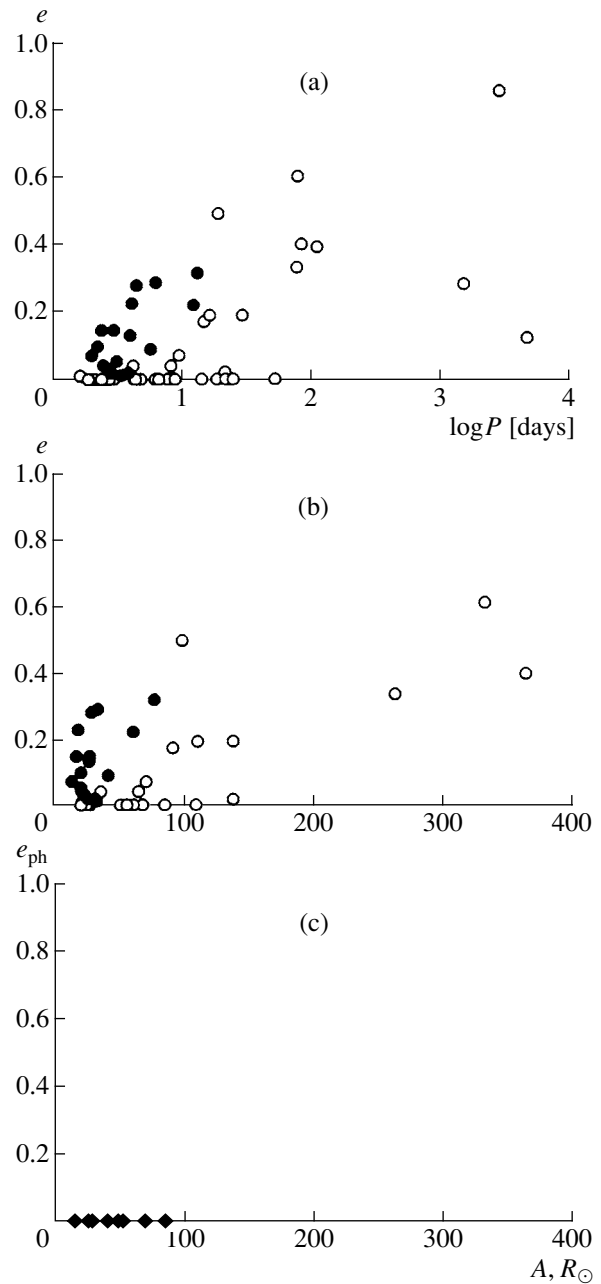

Fig. 5. Comparison of the dependence of eccentricity e on (a) orbital period P and (b) separation A for DMS systems with masses $M_1 + M_2 > 10 M_\odot$ (filled circles) and for WR + O systems (open circles). The $e(A)$ relation for SD systems is also shown (c). The A values are expressed in solar radii.

Figure 4 displays the dependence of the spectroscopic orbital eccentricities e_{sp} on the orbital periods P for 35 WR + O binaries (the table), 174 OB + OB systems from [29], and 68 eclipsing binaries in the Large Magellanic Cloud [28]. A comparison of Fig. 4a and Fig. 4b reveals a strong difference between the $e_{sp}(P)$ distributions for WR + O and OB + OB sys-

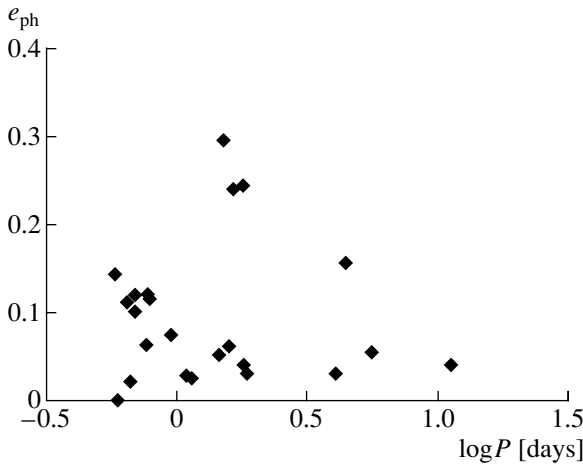**Fig. 6.** Dependence of orbital eccentricity e_{ph} and period P for CE systems with any mass.

tems. As noted above, values $e_{\mathrm{sp}} < 0.1$ can be spurious, and we will use the value $e_{\mathrm{sp}} = 0.1$ to estimate the spectroscopic transition period $P_{\mathrm{tr}}^{\mathrm{sp}}$. We will take $P_{\mathrm{tr}}^{\mathrm{sp}}$ to be the orbital period such that all orbits with $P < P_{\mathrm{tr}}^{\mathrm{sp}}$ have spectroscopic eccentricities below 0.1 ($e_{\mathrm{sp}} < 0.1$), while orbits with $e \geq 0.1$ are encountered for $P > P_{\mathrm{tr}}^{\mathrm{sp}}$. Among the WR + O systems, $e_{\mathrm{sp}} < 0.1$ for all systems with $P \leq P_{\mathrm{tr}}^{\mathrm{sp}}(\mathrm{WR}) = 14^{\mathrm{d}}$ ($\sim 50\%$ of the total number of systems). Orbits with $e \geq 0.1$ are encountered only for $P > 14^{\mathrm{d}}$. In the interval $14^{\mathrm{d}} < P < 53^{\mathrm{d}}$, both systems with $e_{\mathrm{sp}} < 0.1$ and with $e_{\mathrm{sp}} \geq 0.1$ are encountered among the WR + O binaries. The fractions of systems with $e_{\mathrm{sp}} < 0.1$ and $e_{\mathrm{sp}} \geq 0.1$ for $14^{\mathrm{d}} < P < 53^{\mathrm{d}}$ are 60% and 40%, respectively. For $P > 53^{\mathrm{d}}$, all the orbits of the WR + O systems have significant eccentricities, $e_{\mathrm{sp}} > 0.1$ ($\sim 20\%$ of the total number of known WR + O systems with measured radial-velocity curves). The parameters for the system B86 (see the table), with a period of $P = 52^{\mathrm{d}}7$, are only preliminary, and we adopt the more conservative estimate $P = 30^{\mathrm{d}}{-}50^{\mathrm{d}}$ for the boundary value of the orbital period beyond which all the orbits are elliptical. The fraction of WR + O binaries with $P < 30^{\mathrm{d}}{-}50^{\mathrm{d}}$ and $e_{\mathrm{sp}} > 0.1$ remains the same ($\sim 20\%$).

For the OB + OB systems, a significant number of orbits with $e_{\mathrm{sp}} > 0.1$ appear for periods $P > P_{\mathrm{tr}}^{\mathrm{sp}}(\mathrm{OB}) \cong 2^{\mathrm{d}}8$ (see also [55]). The values $P_{\mathrm{tr}}^{\mathrm{sp}}(\mathrm{WR}) = 14^{\mathrm{d}}$ for the WR + O binaries and $P_{\mathrm{tr}}^{\mathrm{sp}}(\mathrm{OB}) = 2^{\mathrm{d}}8$ for the OB + OB systems differ by a factor of five. This large difference of the transition periods indicates that the efficiency of the orbital circularization is much higher for WR + O systems than for OB + OB binaries; it is natural to attribute this to the effects

of Roche lobe filling by the initially more massive O star and mass transfer through the inner Lagrange point L_1 in the parent O + O systems. Note also that the range of periods for circular orbits of WR + O binaries, $1^{\mathrm{d}}6 < P < 14^{\mathrm{d}}$, is close to the range for SD systems with subgiants, $0^{\mathrm{d}}7 < P < 15^{\mathrm{d}}$, which are known to have $e \equiv 0$.

To verify these results, we will compare the $e_{\mathrm{sp}}(P)$ distribution for the WR + O binaries with the most reliable data on the photometric orbital eccentricities of close binaries e_{ph}.

Figure 4c presents the $e_{\mathrm{ph}}(P)$ distribution for 68 eclipsing binary systems of the Large Magellanic Cloud [28]. All the eclipsing systems contain components with spectral types earlier than A0 [28], so that all of them can be considered massive OB + OB close binaries with combined component masses $M_1 + M_2 > 10 M_{\odot}$. We can see in Fig. 4c that values $e_{\mathrm{ph}} > 0.1$ begin to appear for periods $P > P_{\mathrm{tr}}^{\mathrm{sp}}(\mathrm{LMC}) \cong 2^{\mathrm{d}}$, close to the value $P_{\mathrm{tr}}^{\mathrm{sp}}(\mathrm{OB}) = 2^{\mathrm{d}}8$ for the OB + OB binaries of [29].

An even more rigorous verification of our results can be performed using the photometric orbital eccentricities for DMS eclipsing binaries with the best-studied light curves, including DMS systems with measured apsidal motions [27]. Figure 5 displays a comparison of the $e_{\mathrm{ph}}(P)$ and $e_{\mathrm{ph}}(A)$ distributions (A is the semi-major axis of the relative orbit) for massive DMS systems and of the $e_{\mathrm{sp}}(P)$ and $e_{\mathrm{sp}}(A)$ distributions for the WR + O systems; the $e_{\mathrm{ph}}(A)$ distribution for SD systems (which all have $e_{\mathrm{ph}} \equiv 0$) is also shown. We selected only DMS systems with combined masses $M_1 + M_2 > 10 M_{\odot}$. We used the data for WR + O systems with the entire range of known masses.

We can see in Fig. 5 that the data for the most reliable orbital eccentricities confirms our results: in the period range $P < P_{\mathrm{tr}}^{\mathrm{sp}}(\mathrm{WR}) = 14^{\mathrm{d}}$, where all the e_{sp} values for WR+ O systems are below 0.1, virtually all the e_{ph} values for the DMS systems are significantly different from zero. The corresponding spectroscopic transition period for massive DMS systems is $P_{\mathrm{tr}}^{\mathrm{sp}}(\mathrm{DMS}) = 2^{\mathrm{d}}{-}3^{\mathrm{d}}$. The range of semi-major axes for which all orbits are nearly circular is $A \leq 90{-}100 R_{\odot}$ for the WR + O systems and $A \leq 20 R_{\odot}$ for the DMS systems.

We thus observe a dramatic difference between the orbital eccentricity distributions for WR + O binaries and massive DMS systems: the transition period for the massive DMS systems, $P_{\mathrm{tr}}^{\mathrm{sp}}(\mathrm{DMS}) = 2^{\mathrm{d}}{-}3^{\mathrm{d}}$, is much shorter than the period for the WR + O systems, $P_{\mathrm{tr}}^{\mathrm{sp}}(\mathrm{WR}) = 14^{\mathrm{d}}$. The ranges of periods and orbital semi-major axes for WR + O binaries with

circular orbits ($P < 14^d$, $A < 90-100R_\odot$) are close to the corresponding ranges for SD systems with subgiants.

Figure 6 displays the $e_{ph}(P)$ relation for the CE systems. These massive close binaries are at an early stage of the initial mass transfer, presumably preceding the formation of WR + O systems. We see that the e_{ph} values are nonzero over the entire range of orbital periods, $P \le 10^d$. This is quite understandable: intense mass transfer capable of efficient orbital circularization in early stages has not yet begun in CE systems, and the efficiency of orbital circularization via tidal dissipation is rather low for OB + OB systems in some cases (here, $P_{tr}^{sp}(DMS) = 2^d-3^d$), due to the low viscosity of the matter in the OB envelopes and the short time scale for their nuclear evolution. However, since the relative radii of the components are high for some CE systems ($R/a \cong 0.4-0.5$) and exceed the critical value for stars with radiative envelopes, $R/a = 0.25$ (see above), orbital circularization during the DMS stage and the stage close to the Roche lobe filling operates efficiently.

6. ANALYSIS OF PARTICULAR TYPES OF WR+O SYSTEMS

Let us consider known WR + O systems (see the table) and estimate the influence of various factors on their orbital circularization as functions of the initial periods and masses of their parent $O_1 + O_2$ systems.

The mean combined mass of the WR + O systems is $M_{WR} + M_O \cong 50M_\odot$ [8]. Taking into account the mass loss via the WR wind and possible mass loss from the binary system during the mass transfer, we adopt the value $M_1 + M_2 = 70M_\odot$ for the mean combined mass of the parent $O_1 + O_2$ systems. For a mean initial mass ratio $q_0 = 0.8$, the initial component masses for the parent $O_1 + O_2$ system are $M_1 \cong 40M_\odot$ and $M_2 \cong 30M_\odot$, and the corresponding radii are $R_1 = 10R_\odot$ and $R_2 = 9R_\odot$ [32]. Then, the critical relative radius of the primary star for which an elliptical orbit becomes circular within a time equal to one-quarter of the main-sequence life time of the O_1 star [38, 41], $R_1/a = 0.25$, corresponds to the critical orbital period $P_{crit} = 3^d3$ and the critical semi-major axis $a_{crit} = 40R_\odot$. Note that the value $P_{crit} = 3^d3$ is close to the spectroscopic transition period for massive OB +OB systems, $P_{tr}^{sp} = 2^d-3^d$, corresponding to the transition from nearly circular to elliptical orbits.

Since the synchronization of the axial and orbital motions in a close binary occurs prior to circularization of its orbit [41], let us consider the parent $O_1 + O_2$ systems in an established synchronous regime with the initial orbital eccentricity e_0.
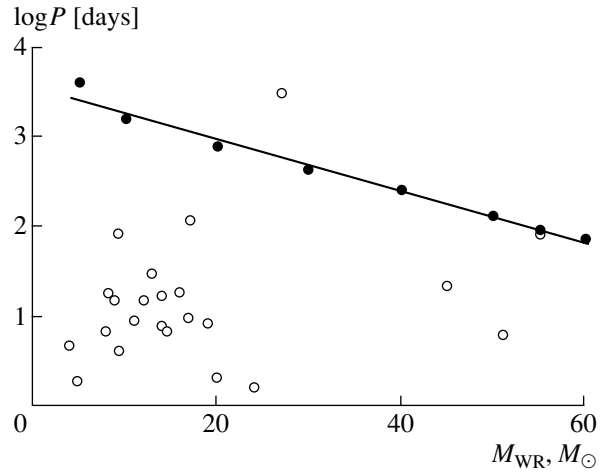

Fig. 7. Positions of known SB2 WR + O systems in the $M_{WR} - \log P$ plane (open circles). The solid line corresponds to the relation between the maximum initial period of the parent $O_1 + O_2$ system, P_{max}^i, and the initial mass of the WR stars formed in the mass transfer, M_{WR}^i. All known SB2 WR + O systems except for the HD 193793 and HD 92740 systems were formed as a result of mass transfer.

If the initial orbital period of the parent $O_1 + O_2$ system with $e = e_0$ is $P \le 3^d3$ ($a \le 40R_\odot$), the elliptical orbit has enough time to circularize due to tidal effects in the DMS stage, prior to the primary star's filling its Roche lobe. After the circularization of the elliptical orbit, the orbital period significantly decreases due to tidal effects [38, 41], facilitating Roche lobe filling by the O_1 star. The subsequent mass transfer takes place in the circular orbit, leading to the formation of a WR + O system with e = 0. In the case of conservative mass transfer, the orbital period increases substantially compared to its initial value (see, for example, [38]). If the mass transfer is accompanied by a loss of mass and angular momentum from the system, the period of the WR + O system that is formed can be close to the initial value. The degree of nonconservativeness of the mass transfer depends on many factors (see, for example, [56, 57]), and it is not possible to uniquely relate the initial period of the parent $O_1 + O_2$ system to the period of the resulting WR + O binary.

Thus, as for the SD systems, the role of mass transfer in orbital circularization is negligible in the closest parent $O_1 + O_2$ systems, and the main result of the mass transfer is a strong increase of the orbital period of the formed WR + O system compared to its initial period (if the mass transfer is conservative).

If the initial period is $P > 3^d3$ ($a > 40R_\odot$), the mass transfer in the $O_1 + O_2$ system may occur in an elliptical orbit, if the orbit did not have enough time to circularize during the DMS stage. The time for orbital

circularization due to tidal effects in massive $O_1 + O_2$ systems depends very strongly on the relative radius of the O_1 primary: $t_{\mathrm{circ}} \sim (R/a)^{-10.5}$ [41]. Therefore, the orbital circularization time decreases drastically during the evolutionary increase of the O_1 star radius. For example, a twofold increase of R_1/a, from the critical value (0.25) to the size of the Roche lobe ($\sim$ 0.5), corresponds to a decrease of t_{circ} by three orders of magnitude. At the same time, if the O_1 star has significantly left the main sequence, the time scale for its evolutionary expansion is of the order of the thermal relaxation time, which is shorter than the nuclear evolution time by three orders of magnitude. Thus, the decrease of the orbital circularization time due to the O_1 star filling its Roche lobe is compensated by the decrease of the evolution time scale for the O_1 star. We can assume this compensation to be incomplete for $O_1 + O_2$ systems with the longest periods, in which the O_1 star fills its Roche lobe during the most advanced, and hence short-lived, stage of its evolution, so that there remains a considerable orbital eccentricity by the beginning of the mass transfer in the parent long-period $O_1 + O_2$ system. At early stages of the mass transfer, when the more massive star, O_1, flows onto the less massive star, e decreases. If the orbit has not had enough time to circularize during early stages of the mass transfer, the eccentricity will grow after the masses become equal, with continuing mass transfer. Further increase of the eccentricity after the mass transfer is favored by variable radial mass loss via the stellar wind from the WR star in the WR + O system formed, which is maximum at the orbit periastron.

If, however, the orbit becomes circular during early stages of the mass transfer, a WR + O system with a circular orbit forms as a result of the mass transfer.

The WR + O systems form from massive $O_1 + O_2$ systems. For each initial mass of the O_1 primary, there is a maximum initial orbital period separating $O_1 + O_2$ systems with and without mass transfer, since the possibilities for the O_1 star's radius to increase in the course of its nuclear evolution are limited. It was shown in [22] that, if we take the Humphreys–Davidson limit [17]—attained by massive stars after hydrogen burning in their cores ceases—as an estimate of the maximum radius of the O_1 star, we can estimate the corresponding maximum initial orbital periods, P_{max}^i; if the initial mass ratio is $q_0 = 0.6$, $P_{\mathrm{max}}^i \cong 1900^{\mathrm{d}}$ for $M_1 = 20 M_\odot$, $\sim 900^{\mathrm{d}}$ for $M_1 = 40 M_\odot$, $\sim 400^{\mathrm{d}}$ for $M_1 = 60 M_\odot$, and $\sim 10^{\mathrm{d}}$ for $M_1 = 120 M_\odot$ [22]. The $O_1 + O_2$ binaries with initial periods $P^i > P_{\mathrm{max}}^i$ do not experience a mass-transfer stage: in this case, the maximum evolutionary increase of the O_1-star radius is insufficient for the star to fill its Roche lobe.

Let us check if the known WR + O systems satisfy these conditions (the table). The initial mass of the WR star in a close binary after mass transfer is related to the mass of the parent O_1 star by the formula [3, 57]

$$\frac{M_{\mathrm{WR}}^i}{M_\odot} = 0.1 \left(\frac{M_1}{M_\odot} \right)^{1.4}$$

for $3 M_\odot \leq M_1 \leq 100 M_\odot$. It gives the initial masses of the parent O_1 stars: $M_1 = 16 M_\odot$ for $M_{\mathrm{WR}}^i = 5 M_\odot$, $M_1 = 26 M_\odot$ for $M_{\mathrm{WR}}^i = 10 M_\odot$, $M_1 = 43 M_\odot$ for $M_{\mathrm{WR}}^i = 20 M_\odot$, $M_1 = 58 M_\odot$ for $M_{\mathrm{WR}}^i = 30 M_\odot$, $M_1 = 71 M_\odot$ for $M_{\mathrm{WR}}^i = 40 M_\odot$, $M_1 = 89 M_\odot$ for $M_{\mathrm{WR}}^i = 55 M_\odot$.

Each initial mass of the WR star corresponds to a maximum orbital period for the $O_1 + O_2$ system: $P_{\mathrm{max}}^i \approx 4000^{\mathrm{d}}$ for $M_{\mathrm{WR}}^i = 5 M_\odot$, $\sim 1500^{\mathrm{d}}$ for $M_{\mathrm{WR}}^i = 10 M_\odot$, $\sim 700^{\mathrm{d}}$ for $M_{\mathrm{WR}}^i = 20 M_\odot$, $\sim 400^{\mathrm{d}}$ for $M_{\mathrm{WR}}^i = 30 M_\odot$, $\sim 250^{\mathrm{d}}$ for $M_{\mathrm{WR}}^i = 40 M_\odot$, $\sim 130^{\mathrm{d}}$ for $M_{\mathrm{WR}}^i = 50 M_\odot$, $\sim 90^{\mathrm{d}}$ for $M_{\mathrm{WR}}^i = 55 M_\odot$, $\sim 75^{\mathrm{d}}$ for $M_{\mathrm{WR}}^i = 60 M_\odot$.

Because of the mass loss via the wind, the observed masses of the WR stars in WR + O systems (Table) are lower than the corresponding initial values, M_{WR}^i. The decrease in mass depends on the age of the WR stars and, using the current mass-loss rates $\dot{M}_{\mathrm{WR}}$ [8], does not exceed $30-40\%$, on average. In many cases, the observed periods of WR + O systems are probably longer than the initial periods of the parent $O_1 + O_2$) systems P^i though the opposite may be true for the shortest period WR + O systems with $P < 3^{\mathrm{d}}$ (nonconservative mass transfer).

Figure 7 presents the $\log P_{\mathrm{max}}^i = f(M_{\mathrm{WR}}^i)$ relation, with the WR stars plotted at positions corresponding to the observed M_{WR} and P values for known SB2 WR + O systems (see the table). Even taking into account uncertainties in estimating the initial masses M_{WR}^i and periods P^i from the observed values, there is good reason to conclude that most known SB2 WR + O systems must have undergone a mass-transfer stage. Only two of the 23 known SB2 WR + O systems were apparently formed not as a result of mass transfer but exclusively due to radial mass loss via their stellar winds. These are the HD 193793 ($P = 2900^{\mathrm{d}}$, $e = 0.85$, $M_{\mathrm{WR}} = 27 M_\odot$) and HD 92740 ($P = 80\overset{\mathrm{d}}{.}336$, $e = 0.60$, $M_{\mathrm{WR}} = 55 M_\odot$) systems, which have positions in Fig. 7 very close to the critical line, $\log P_{\mathrm{max}}^i = f(M_{\mathrm{WR}}^i)$. It is striking that these particular WR + O systems possess the highest orbital eccentricities: $e = 0.85$ and $e = 0.60$. The values of e for the remaining SB2 R + O binaries after the mass-transfer stage

are $e = 0-0.5$. The large e values for HD 193793 and HD 92740 are probably due to the fact that the orbital circularization during the DMS stage was negligible for these systems, and there was no mass transfer. For these reasons, the systems have retained their initial $e = e_0$ values, which have been further increased to the observed values due to variable radial mass loss via the wind from the WR star in the elliptical orbit.

It seems likely that the two systems with the longest orbital periods among the SB1 WR + O systems (HD 192641, $P = 4765^d$, $e > 0.12$ and HD 193077, $P = 1538^d$, $e = 0.28$) also evolved without mass transfer, with outflows via their stellar winds (final conclusions will be possible when the masses of the WR stars in these systems are estimated). Thus, the number of known WR + O systems that evolved exclusively under the action of wind outflows does not exceed 4 of 35, or $\leq 11\%$.

For case B conservative mass transfer, the periods of the corresponding WR + O systems after the mass transfer should be at least $\sim 10^d$ [57]. However, 18 of the 35 known WR + O systems (the table), or 51%, have periods below 10^d. We noted above that it is impossible to explain periods this short for WR + O systems as resulting exclusively from evolution under the action of the stellar wind. The most reasonable explanation for these short periods is nonconservative mass transfer in the parent $O_1 + O_2$ systems [57]. Two SB2 WR + O systems of the 23 known (HD 92740, $q = 2.6$, $P = 80^d336$, $e = 0.60$ and HD 193928, $q = 1.5$, $P = 21^d6895$, $e = 0.02 \pm 0.08$) have component mass ratios $q = M_{WR}/M_O > 1$, which are inconsistent with a scenario with mass transfer without a common envelope stage. As noted above, the HD 92740 system probably evolved exclusively under the influence of radial outflow via its stellar wind. The orbital period of HD 193928 is too long for the system to have undergone a common-envelope stage, and its eccentricity is too low for the system to evolve solely under the action of the wind outflow. The problem of this system's evolutionary status remains open. The unusual characteristics of HD 193928 could be due to peculiarity of the initial parameters of the parent $O_1 + O_2$ system.

Let us now consider the various stages of orbital circularization for the WR + O systems that have passed through a mass-transfer stage (31 systems; see the table).

All the systems with $P \leq 14^d3$ (19 of 35 known systems, or 54%) have circular or nearly circular orbits ($e_{sp} < 0.1$). In these WR + O systems, orbital circularization took place either during the DMS

stage (systems with $P \lesssim 3^d$) or early in the mass-transfer stage, before the equalizing of the component masses in the $O_1 + O_2$ system.

In the period range $14^d < P < 30^d-50^d$, both circular and elliptical orbits are found, and systems with $e = 0$ and $e \neq 0$ do not obviously differ in terms of the masses of their WR stars. These systems were also formed as a result of mass transfer in the parent $O_1 + O_2$ systems. Due to their long initial periods, $P^i > 3^d3$, there was not enough time in the DMS stage for complete circularization of the orbit. Therefore, the mass transfer began in an elliptical orbit. Some of the systems could not complete their orbital circularization during the early mass-transfer stage, and the subsequent mass transfer after equalization of the component masses (with mass flowing from the less massive the more massive star) resulted in the formation of the WR + O systems and an increase of their residual orbital eccentricities. The further growth of the orbital eccentricities due to the variable radial wind from the WR star in the elliptical orbit established the observed eccentricities. The other group of WR + O systems, with periods in the range $14^d < P < 30^d-50^d$, completed their orbital circularization during the early mass-transfer stage, forming WR + O systems with circular orbits.

All the systems with $P > 30^d-50^d$ have elliptical orbits. If we exclude four long-period systems (HD 193793, HD 92740, HD 192641, and HD 193077) that apparently were formed by outflow through stellar wind, the rest of the systems, with $P > 30^d-50^d$, could well originate due to mass transfer. Since the initial periods are much longer than the critical period ($P^i \gg 3^d3$), these WR + O systems could not complete their orbital circularization during either the DMS stage or the early mass-transfer stage. After the equalization of the component masses, the secondary stage of mass transfer and the subsequent radial outflow via the wind of the WR star in the elliptical orbit resulted in the formation of WR + O systems with the observed orbital eccentricities.

Note that WR stars are encountered even in visual binary and multiple systems with elliptical orbits [9]. In such cases, the formation of the WR star must have occurred due to radial mass loss in the form of a stationary stellar wind, and possibly also due to the LBV phenomenon (as for the WR + O system HD 5980 [58]). An example of a system where an initially massive O star did not fill its Roche lobe and evolved under the influence of radial mass loss via the stellar wind and the LBV phenomenon may be the transient X-ray binary GRS1915 + 105, which has a black hole ($M_x = 14 \pm 4M_\odot$, $M_v = 1.2 \pm 0.2M_\odot$) and a very long orbital period, $P = 33^d5$ [59].
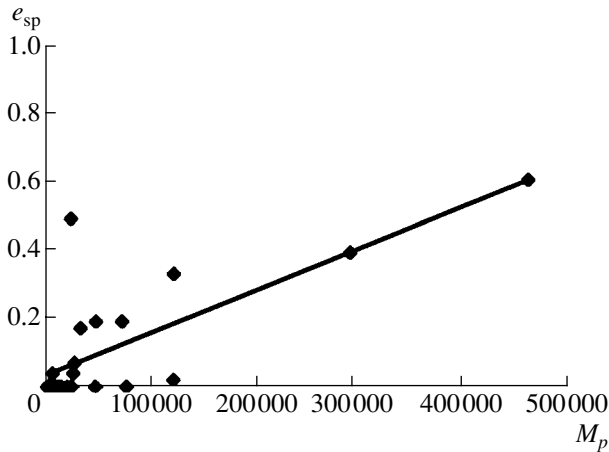
Fig. 8. Relation between the orbital eccentricities of the WR + O systems, e_{sp}, and the parameter $M_p = (M_{WR} + M_O)^2 P$, which is inversely proportional to the number of orbital periods elapsed during the mass transfer, N.

Thus, our results suggest that up to 90% of known WR + O binaries were formed from massive $O_1 + O_2$ systems as a result of the more massive O_1 star filling its Roche lobe and the associated flow of material through the inner Lagrange point L_1, in agreement with the standard evolution scenario for close binary systems [1−3]. Of course, modern versions of this scenario should take into account the stellar wind flow from the massive O stars and WR stars and the effects of collisions between the stellar winds, which disturb the conservative character of the mass transfer, but probably do not qualitatively change the general pattern of the mass transfer in massive close binaries [22, 23]. Note that, even without taking into account the wind outflow, recent three-dimensional gas-dynamical computations of gas flows in interacting close binaries demonstrate that, if the primary fills its Roche lobe and matter flows through the inner Lagrange point, up to 50% of the matter can leave the system in the region of the outer Lagrange point, L_2 [56].

7. RELATION BETWEEN THE ORBITAL ECCENTRICITIES OF THE WR + O SYSTEMS AND THE NUMBER OF ORBITAL PERIODS ELAPSED DURING THE MASS TRANSFER

If the mass transfer in close binaries occurs on the thermal time scale, we expect that large orbital eccentricities should be found more often for close binaries with the largest combined masses and the largest initial orbital periods. The thermal relaxation time for a massive O_1 star—the progenitor of the WR

star in a WR + O system—is

$$T_k \cong \frac{GM_1^2}{R_1 L_1} \sim \frac{10^7}{M_1^2} \text{ years},$$

where M_1 is the initial mass of the O_1 star in solar units. The number of orbital periods elapsed during the mass-transfer stage in the close binary, which is close to T_k, is

$$N \approx \frac{10^7}{M_1^2 \bar{P}},$$

where $\bar{P}$ is the orbital period (in years), averaged over the time for the mass transfer. The resulting orbital eccentricity toward the end of the early mass-transfer stage e_f, is lower the higher the number of periods N, and we can suppose that

$$e_f \sim M_1^2 \bar{P}.$$

Thus, we expect a correlation between the observed orbital eccentricities in WR + O binaries and the values of $M_1^2 \bar{P}$. Since (i) more than half the mass of the primary O_1 flows onto the secondary O_2 as a result of the mass transfer and (ii) some fraction of the matter flowing out of the O_1 star may leave the binary system through the outer Lagrange point L_2 [56] and (iii) the formed WR star loses mass via its stellar wind, we can use the combined mass of the WR + O binary, $M_{WR} + M_O$, as a rough estimate for the initial mass M_1. As an estimate of $\bar{P}$, we take the observed period of the WR + O system, P (since the dependence on $\bar{P}$ is linear, this will probably lead to only small errors in our estimate of e_f).

Figure 8 presents the dependence of the observed spectroscopic orbital eccentricities e_{sp} of known SB2 WR + O binaries on the $M_p = (M_{WR} + M_O)^2 P$. We have not included the longest period SB2 WR + O system HD 193793, which has probably not passed through a mass-transfer stage (see above). The square of the combined mass of the WR + O binaries varies from system to system by one to two orders of magnitude, and the period P by two to three orders of magnitude. Thus, the relation $e_{sp}[(M_{WR} + M_O)^2 P]$ resembles the relation $e_{sp}(P)$ (Fig. 4). On the other hand, taking into account the influence of the combined mass improves the correlation between e_{sp} and $(M_{WR} + M_O)^2 P$: the number of systems with $e_{sp} \cong 0$ in the region of large values of the argument becomes lower. The correlation coefficients in the $e_{sp}[M_{WR} + M_O)^2 P]$ and $e_{sp}(P)$ relations are 0.56 and 0.42, respectively.

Thus, the correlation in Fig. 8 agrees with the hypothesis of De Greve [22] that the original elliptical orbits of massive close binaries may have insufficient time to circularize, because they experience mass

transfer for a comparatively short time. The efficiency of the circularization of an elliptical orbit depends, not only on the number of orbital periods elapsed during the initial stage of the mass transfer (before the equalization of the component masses), but also on the motional energy the star loses during each elliptical orbit (for a given angular momentum of the system, the orbital eccentricity leads to an excess kinetic energy of the star's orbital motion over that for a circular orbit). The longer the period P, the lower the number of orbits elapsed during the early mass-transfer stage, but the mean kinetic energy of the star's orbital motion also simultaneously decreases (as $\bar{v}^2$), facilitating circularization of the orbit. Which factor will win out as the period increases—the effect of the lower number of orbits (slowing the circularization of the orbit during the mass transfer) or the effect of the decreasing kinetic energy of the star's orbital motion (facilitating orbital circularization during the mass transfer)?

Simple estimates show that, since the semi-major axis of the orbit is $a \sim P^{2/3}$, the mean kinetic energy of the star's orbital motion is

$$\bar{E}_k \sim \bar{v}^2 \sim \frac{a^2}{P^2} \sim P^{-2/3}.$$

At the same time, the number of orbital periods elapsed during the early stages of the mass transfer is

$$N \sim P^{-1}.$$

Thus, the kinetic energy of the star's orbital motion decreases with increasing orbital period more slowly than does the number of orbital periods during the early mass-transfer stage. This suggests that the circularization of the binary orbit due to mass transfer becomes less efficient as the orbital period P increases, since, in this case, the binary system must lose a relatively higher fraction of the kinetic energy of the orbiting stars over a smaller number of orbits.

It is interesting to study the dependence of the orbital eccentricities of close binaries on the combined masses of the components. Figure 9 shows $e(M_1 + M_2)$ relations for the WR + O, DMS, and CE systems. We can see that there is practically no correlation between the orbital eccentricities and the combined masses for the DMS systems, as is quite natural. There is a hint of a weak correlation for the CE systems: on average, e increases with increasing $M_1 + M_2$, though the significance of this correlation is very low (the correlation coefficient is 0.06).

For the WR + O binaries, there is a weak correlation between the orbital eccentricities and the combined masses (correlation coefficient 0.11): on average, the $e_{\rm sp}$ values increase with increasing combined mass. This result is consistent with the hypothesis
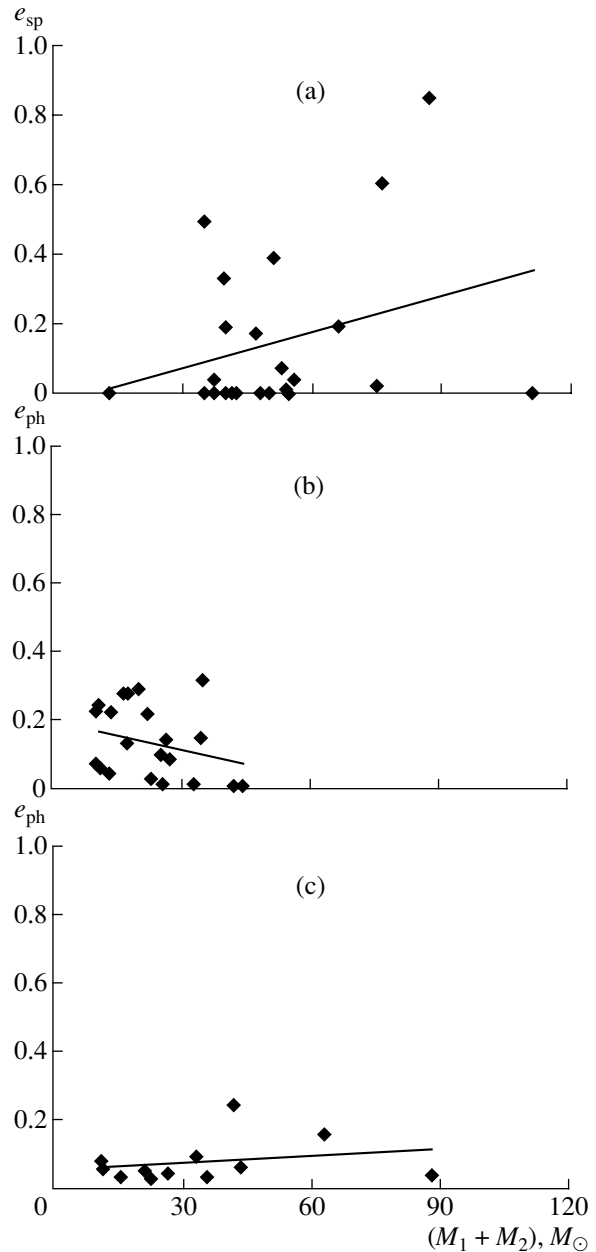
Fig. 9. Relation between the orbital eccentricities, e, and the combined component masses for the (a) WR + O, (b) DMS, and (c) CE systems.

that the orbits of the most massive WR + O systems were not completely circularized because the mass-transfer stage was too short [22]. Taking into account the influence of the orbital periods (see above), we find a significant correlation between the values of $e_{\rm sp}$ and of $(M_{\rm WR} + M_{\rm O})^2 P$ for the WR + O systems (the correlation coefficient is 0.56; Fig. 8).

In light of the above discussion, it is interesting to study the SD systems with the highest combined masses and the longest orbital periods to look

for "residual" photometric orbital eccentricities using high-accuracy light curves. If found, the small "residual" orbital eccentricities of these SD systems could be important for estimating the efficiency of orbital circularization in close binary systems.

Thus, the existence of significant orbital eccentricities for WR + O systems with long orbital periods ($P > 30^d$–50^d) cannot be considered decisive evidence against mass transfer in the parent O + O systems.

Theoretical gas-dynamical studies of mass transfer in massive close binaries and a rigorous quantitative analysis of the efficiency of circularization of initially elliptical orbits during this evolutionary stage of binary systems are of considerable interest.

8. EXAMPLES OF MASSIVE CLOSE BINARIES WITH MASS TRANSFER AND INTENSE STELLAR WINDS

Here, we list some massive close binaries that show obvious signs of Roche lobe filling by one of the stars and a flow of material through the inner Lagrange point L_1, despite the presence of an intense stellar wind from the components.

(1) There is a whole class of interacting W Ser-type binary systems (for example, see [6, 7]). In these systems, the less massive star fills its Roche lobe, and matter flows through the inner Lagrange point L_1 onto the more massive component, around which a thick disk forms, made up of the material of the outflowing star. In several cases, an excess helium abundance has been found for the less massive, outflowing star (β Lyr, RY Sct). Thus, W Ser systems have almost completed the process of the components' exchange of roles during the mass transfer. Of special interest among these systems are the most massive close binaries: RY Sct ($M_1 = 35M_\odot$, $M_2 = 10.7M_\odot$, $P \cong 11^d12$), β Lyr ($M_1 = 13.4M_\odot$, $M_2 = 3M_\odot$, $P \cong 12^d93$), V367 Cyg ($M_1 = 19M_\odot$, $M_2 = 12M_\odot$, $P \cong 18^d60$), W Cru ($M_1 = 26M_\odot$, $M_2 = 26M_\odot$, $P \cong 198^d5$). These systems can be considered the immediate progenitors of WR + O binaries. For example, Antokhina and Cherepashchuk [60] showed for one of the most massive W Ser systems, the binary RY Sct, that the parameters of its components derived from an analysis of its light curve and radial-velocity curve suggested this system is a progenitor of a WR + O binary.

Thus, observations of W Ser systems directly indicate that, despite the strong outflow via the stellar wind, the initially more massive O star has filled its Roche lobe, enabling mass transfer through the inner Lagrange point L_1, leading to a reversal of the masses

of the components and the formation of a helium-excess star, the progenitor of a WR star.

Other examples of massive close binaries that can be considered progenitors of WR + O binaries (BD+40°4220 and HDE 228776) are discussed by Massey and Conti [61].

(2) Another example is provided by quasi-stationary X-ray binaries with OB supergiants of the Cyg X-1 and Cen X-3 type [6, 7]. These systems are close to the early stage of secondary mass transfer. The regular optical variability of these systems, due primarily to the ellipsoidality of the optical star, testifies that their optical stars are strongly tidally distorted and are close to filling their Roche lobes, despite the intense radial outflow via the stellar wind (at a rate of about $10^{-6}M_\odot$/yr). In this case, as for the W Ser systems, the strong stellar wind from the massive, hot OB supergiant does not prevent the filling of its Roche lobe. Since the relative radii of the optical stars are high in these systems ($R/a \cong 0.5$), their orbits are usually close to circular (with the exception of the Vela X-1 system, for which $P \cong 9^d$, $e = 0.09$). This is due to orbital circularization during the DMS stage and the stage when the radius of the optical star approaches that of the Roche lobe, since the value of R/a exceeds the critical value (0.25) in this case.

(3) The object SS 433 provides another example. This massive X-ray binary at an advanced evolutionary stage contains a relativistic object and an optical star that fills or overfills its Roche lobe and exhibits intense secondary mass transfer, at a rate of up to $10^{-4}M_\odot$/yr [62]. The normal star fills or overfills its Roche lobe despite the intense stellar wind, in addition to the strong wind ($\dot{M} \cong 10^{-4}M_\odot$/yr) from the supercritical accretion disk surrounding the relativistic object.

(4) Another example is the object Cyg X-3. This short-period X-ray binary ($P = 4.8$ hours) with an optical WR star was probably formed during the secondary mass transfer in a common-envelope binary system via the "spiraling" mechanism for braking of the relativistic object and intense mass loss by the binary [30]. The system completed the secondary mass transfer during its common-envelope evolution, resulting in a considerable loss of angular momentum and a strong decrease in the period. However, in this case, the formation of a "second-generation" WR star unavoidably had to pass through a stage of Roche lobe filling by the massive O-star progenitor of the WR star, with an intense flow of matter through the inner Lagrange point L_1 onto the relativistic object. Thus, Cyg X-3 is a good example of a close binary that experienced secondary mass transfer via the inner Lagrange point L_1.

Finally, according to [32], there is a separate class of so-called contact early-type binaries (CE systems; we have used their parameters in this paper), which contains many systems with very high masses and strong outflows of matter via their stellar winds, such as AO Cas ($M_1 = 29 M_\odot$, $M_2 = 24.5 M_\odot$, $P = 3\overset{d}{.}52$); UU Cas ($M_1 = 42.5 M_\odot$, $M_2 = 34 M_\odot$, $P = 8\overset{d}{.}52$), UW CMa ($M_1 = 43.5 M_\odot$, $M_2 = 32.5 M_\odot$, $P = 4\overset{d}{.}39$), V382 Cyg ($M_1 = 27.2 M_\odot$, $M_2 = 19.3 M_\odot$, $P = 1\overset{d}{.}89$), TU Mus ($M_1 = 22.6 M_\odot$, $M_2 = 15.4 M_\odot$, $P = 1\overset{d}{.}39$), V1182 Aql ($M_1 = 29.2 M_\odot$, $M_2 = 11.1 M_\odot$, $P = 1\overset{d}{.}62$), V729 Cyg ($M_1 = 58.5 M_\odot$, $M_2 = 13.7 M_\odot$, $P = 6\overset{d}{.}60$). In all these cases, the strong stellar wind from the system components does not prevent them from filling (or almost filling) their Roche lobes.

The above examples provide direct observational evidence for the importance of mass transfer through the inner Lagrange point L_1 after Roche lobe filling in massive close binaries with intense stellar winds from the components.

9. CONCLUSIONS

Our statistical analysis of the component mass ratios for various types of close binaries (WR + O, DM, CE, and SD systems) shows that the WR + O systems do not exhibit an anticorrelation between the masses of their WR and O components; moreover, there is a hint of a correlation between the component masses: on average, the higher the mass of the O star, the higher the mass of the WR star. The clear correlation (rather than anticorrelation) between the masses of the components of CE systems—and especially of SD systems, which have undoubtedly experienced mass transfer that led to the formation of their subgiants—leads us to the following two conclusions.

(1) The absence of an anticorrelation between the masses of the WR and O stars in WR + O binaries does not provide evidence against the possible formation of the WR stars in massive close binaries due to mass transfer.

(2) The presence of a weak correlation between the masses of the WR and O stars in WR + O binaries and of a clear correlation between the masses of the subgiants and the main-sequence stars in SD systems can be explained by the large scatter of the combined masses of the corresponding parent DMS systems and by the fact that the mean initial mass ratio of the stars in DMS systems is close to unity ($q_0 \cong 0.8$).

Our statistical analysis of the orbital-eccentricity distributions for different types of close binaries (WR + O, DMS, CE, and SD systems) revealed a dramatic difference between the eccentricity distributions for WR + O systems and for DMS OB + OB systems: the spectroscopic transition periods are $P_{tr}^{sp}(WR) = 14^d$ and $P_{tr}^{sp}(DMS) = 2^d - 3^d$.

These facts testify that some orbital-circularization mechanism acts in the WR + O systems, in addition to that operating in massive DMS OB + OB systems (tidal dissipation of the components' orbital energy due to radiative damping of the dynamical tides; for example, see [41]). It is natural to suggest that this additional orbital-circularization mechanism in WR + O systems is the Roche lobe filling by the originally more massive O star in the parent O + O system and the associated mass transfer.

Due to the relatively short mass-transfer time for massive CBSs, the circularization of the orbits of the longest period O + O binary progenitors of WR + O systems probably cannot be completed during the mass-transfer stage (more exactly, during the early part of this stage), since the number of orbital periods elapsing during the early mass-transfer stage is relatively low (three or four orders of magnitude lower than for SD systems with subgiants). Further mass transfer after the component masses have been equalized, when matter flows from the less massive star to the more massive one, leads to an increase in the residual orbital eccentricity. The variable radial mass loss from the WR star that is formed via the wind in the elliptical orbit also favors increasing orbital eccentricity.

In addition, in contrast to SD systems with subgiants, in which the orbital-circularization mechanism (tidal dissipation of the orbital energy in the viscous convective stellar envelopes) operates efficiently during the DMS stage, the effects of orbital circularization during the DMS stage are negligible for the massive O + O binary progenitors of WR + O systems. For these reasons, the longest period WR + O binaries have considerable orbital eccentricities.

Thus, our results indicate that considerable orbital eccentricities for WR + O systems with the longest orbital periods cannot be considered firm evidence against mass transfer in the parent O + O systems. The examples given above of massive close binaries with mass transfer in the presence of strong stellar winds demonstrate the importance and necessity of mass transfer through the inner Lagrange point L_1 in the evolution of massive close binaries.

In summary, we conclude that up to 90% of all known WR + O binaries were formed via the classical mechanism of the reversal of the component masses in massive O + O close binaries [1−3]: the initially more massive O star fills its Roche lobe so that matter flows through the inner Lagrange point L_1.

The longest period WR + O systems (HD 193793, HD 92740, HD 192641, HD 193077) may not have

experienced mass transfer, so that they evolved under the action of the stellar-wind outflow from their massive O components and the LBV phenomenon, in accordance with the scenarios described by Moffat [12] and Conti [5]. Theoretical gas-dynamical studies of the efficiency of circularization of elliptical orbits in massive O + O binaries are of considerable interest in this context.

The distribution of Galactic WN and WC stars in WR + O systems as a function of their orbital periods discussed in [9] is also noteworthy: the relative number of WC stars increases with increasing orbital period. If confirmed for a larger number of WR + O binaries, this will also provide evidence for the importance of mass transfer during the formation of WR stars in WR + O binaries.

Finally, let us estimate the contribution of massive binaries undergoing mass transfer to the formation of WR stars in the Galaxy. Accurate estimation of the role of binarity in the formation of WR stars requires taking into account observational selection effects, which is a separate problem. We restrict our consideration to approximate estimates of the influence of binarity. The fraction of WR + O binaries among WR stars in the Galaxy, estimated mainly from studies of periodic spectroscopic and photometric variability, is $\sim$40% [9, 12]. It is difficult to detect binaries with orbital inclinations that are close to zero, so that this estimate should be considered a lower limit. Taking into account the existence of WR + C binaries with relativistic companions (such as the Cyg X-3 system) and of hypothetical WR + (A$-$M) systems (the progenitors of low-mass X-ray binaries with neutron stars and black holes [8]), we adopt the estimate $\sim$50% as a realistic fraction of binaries among WR stars.

We have estimated that the fraction of WR + O binaries that have undergone mass transfer in their parent massive O + O systems is $\sim$90%. The contribution of WR + O binaries with long ($P > 100^d$) orbital periods, for which there was probably no mass transfer, could be underestimated due to observational selection effects, so that this value should be taken as an upper limit. The fraction of Galactic WR stars formed due to mass transfer in massive O + O binaries is then no higher than 45%. More than 55% of Galactic WR stars were probably formed via stellar-wind outflows and the LBV and RSG phenomena [15, 4, 5], in the case both of single massive O stars and of O + O binaries with large initial orbital periods.

Note that, for the hypothetical WR + (A$-$M) binaries [8], the ratio of the number of systems evolving with mass transfer in a common envelope to the number evolving solely via their stellar wind is 11/1, since

the number of known short-period ($P < 6^d$) X-ray novae is 11 [8, 63], and only one long-period system of this kind has been detected (GRS 1915+105, $P = 33\overset{d}{.}5$ [59]).

Our estimate can be checked independently using data on the distribution of orbital periods of massive OB + OB binaries from the catalog of Batten *et al.* [29]. If, as follows from our results, all the WR + O binaries with periods, $P < 30^d - 50^d$ have passed through a mass-transfer stage, we should estimate the fraction of OB + OB binaries with periods $P < 30^d$ and $P < 10^d$, since the orbital period increases after the mass transfer. The fraction of OB + OB binaries with $P < 30^d$ among all OB + OB systems in [29] ($\sim$200 systems) is $\sim$80%, and the fraction with periods $P < 10^d$ is close to 66%. Taking into account the possible underestimation of the number of OB + OB binaries with long orbital periods, these values should be considered upper limits. The fraction of Galactic WR stars that were formed as a result of mass transfer in massive O + O systems then does not exceed 40%$-$33%, in agreement with the above estimate.

We emphasize again that an accurate account of the role of binarity in the formation of WR stars requires an analysis of all possible observational selection effects, which is a separate problem (see, for example, [35]).

ACKNOWLEDGMENTS

REFERENCES

1. E. P. J. Van den Heuvel and H. Heize, Nature Phys. Sci. **239**, 67 (1972).
2. B. Paczynski, in *IAU Symposium 40: Wolf-Rayet and High Temperature Stars,* Ed. by M. Barry and J. Sahade (Reidel, Dordrecht, 1973), p. 143.
3. A. V. Tutukov and L. R. Yungel'son, Nauchn. Inf. Astrsoveta Akad. Nauk SSSR **27**, 58 (1973); **27**, 70 (1973); **27**, 86 (1973).
4. G. S. Bisnovatyi-Kogan and D. K. Nadejin, Astrophys. Space Sci. **15**, 353 (1972).
5. P. S. Conti, Mem. Soc. R. Sci. Liège **9** (6), 193 (1976).
6. A. M. Cherepashchuk, N. A. Katysheva, T. S. Khruzina, and S. Yu. Shugarov, *Highly Evolved Close Binary Stars: Catalog* (Gordon and Breach, Amsterdam, 1996).

7. A. M. Cherepashchuk, N. A. Katysheva, T. S. Khruzina, and S. Yu. Shugarov, *Highly Evolved Close Binary Stars: Finding Charts* (Gordon and Breach, Amsterdam, 1996), p. 1.

8. A. M. Cherepashchuk, Astron. Zh. **78**, 145 (2001) [Astron. Rep. **45**, 120 (2001)].

9. K. A. van der Hucht, New Astron. Rev. **45**, 135 (2001).

10. R. Kippenhahn and A. Weigert, Z. Astrophys. **65**, 251 (1967).

11. E. P. J. Van den Heuvel, in *IAU Symposium 73: Structure and Evolution of Close Binary Systems,* Ed. by P. Eggleton, S. Mitton, and J. Whelan (Reidel, Dordrecht, 1976), p. 35.

12. A. F. J. Moffat, in *IAU Symposium 163: Wolf-Rayet Stars: Binaries, Colliding Winds, Evolution,* Ed. by K. A. Van der Hucht and P. M. Williams (Kluwer, Dordrecht, 1995), p. 213.

13. P. P. Eggleton and F. Verbunt, Mon. Not. R. Astron. Soc. **220**, 13P (1986).

14. D. Vanbeveren, Astron. Astrophys. **252**, 159 (1991).

15. P. A. Crowther, L. J. Smith, D. J. Hillier, and W. Schmutz, Astron. Astrophys. **293**, 427 (1995).

16. A. Batten, *Binary and Multiple Systems of Stars* (Pergamon, Oxford, 1973; Mir, Moscow, 1976).

17. R. M. Humpreys and K. Davidson, Publ. Astron. Soc. Pac. **106**, 1025 (1994).

18. A. Maeder, in *Proc. 33rd Liège Intl. Astrophys. Colloq. "Wolf-Rayet Stars in the Framework of Stellar Evolution," Liège University, 1996,* Ed. by J. M. Vreux *et al.*, p. 39.

19. P. Massey, Astrophys. J. **246**, 153 (1981).

20. A. M. Cherepashchuk and V. G. Karetnikov, Odessa Astron. Publ. **12**, 180 (1999).

21. V. G. Karetnikov and A. M. Cherepashchuk, Astron. Zh. **75**, 539 (1998) [Astron. Rep. **42**, 476 (1998)].

22. J. P. De Greve, in *Proc. 33rd Liège Intl. Astrophys. Colloq. "Wolf-Rayet Stars in the Framework of Stellar Evolution," Liège University, 1996,* Ed. by J. M. Vreux *et al.*, p. 55.

23. D. Vanbeveren, in *Evolutionary Processes in Binary Stars,* Ed. by M. Wijers, M. Davies, and C. Tout (Kluwer, Dordrecht, 1996), p. 155.

24. V. G. Karetnikov and I. L. Andronov, Available from Ukr. NIINTI, No. 2629-89 (Kiev, 1989).

25. I. I. Bondarenko and E. L. Perevozkina, *Early-Type Contact Binary Stars* [in Russian] (Ural. Univ., Yekaterinburg, 1997).

26. *Catalog of Orbital Elements, Masses and Brightnesses of Eclipsing Detached Main-Sequence Variables and Some Statistical Analysis,* [in Russian] Ed. by I. I. Bondarenko (Ural. Univ., Yekaterinburg, 1999).

27. Kh. F. Khaliullin, in *Binary Stars,* [in Russian] Ed. by A. G. Masevich (Kosmosinform, Moscow, 1997), p. 139.

28. C. Alcock, R. A. Allsman, D. Alves, *et al.*, Astron. J. **114**, 326 (1997).

29. A. H. Batten, J. M. Fletcher, and D. G. Mac Carthy, *Eighth Catalogue of the Orbital Elements of Spectroscopic Binary Systems,* Publ. DAO Victoria XVII (1989).

30. A. M. Cherepashchuk and A. F. J. Moffat, Astrophys. J. **424**, L53 (1994).

31. L. Drissen, R. Lamontagne, A. F. J. Moffat, *et al.*, Astrophys. J. **304**, 188 (1986).

32. M. A. Svechnikov, *Catalog of Orbital Elements, Masses, and Brightnesses of Binary Stars* [in Russian] (Irkutskiĭ Univ., Irkutsk, 1986).

33. D. C. Morton, Astrophys. J. **132**, 146 (1960).

34. J. Smak, Acta Astron. **12**, 28 (1962).

35. L. R. Yungelson and A. V. Tutukov, in *IAU Symposium 143: Wolf-Rayet Stars and Interrelations with Other Massive Stars in Galaxies,* Ed. by K. A. van der Hucht and B. Hidayat (Kluwer, Dordrecht, 1991), p. 459.

36. J. M.García and A. Giménez, in *IAU Symposium 151: Evolutionary Processes in Interacting Binary Stars,* Ed. by Y. Kondo *et al.* (Kluwer, Dordrecht, 1992), p. 295.

37. G. Giuricin, F. Mardirossian, and M. Mezzetti, Astrophys. J., Suppl. Ser. **52**, 35 (1983).

38. J. R. Hurley, A. T. Christopher, and O. R. Pols, Mon. Not. R. Astron. Soc. **329**, 897 (2002).

39. N. Soker, Astron. Astrophys. **357**, 557 (2000).

40. P. Eggleton, *Evolutionary Processes in Binary and Multiple Stars* (Cambridge Univ. Press, Cambridge, 2000).

41. J.-P. Zahn, Astron. Astrophys. **57**, 383 (1977); Erratum, *ibid.* **67**, 162 (1977).

42. J.-P. Zahn, Astron. Astrophys. **220**, 112 (1989).

43. G. H. Darwin, Philos. Trans. R. Soc. London **170**, 1 (1879).

44. P. Artymowicz and S. H. Lubow, Astrophys. J. **421**, 651 (1994).

45. P. Artymowicz, C. J. Clarke, S. H. Lubow, and J. E. Pringle, Astrophys. J. **370**, L35 (1991).

46. J.-P. Zahn and L. Bouchet, Astron. Astrophys. **223**, 112 (1989).

47. W. W. Campbell, Lick Obs. Bull. **6**, 17 (1910).

48. R. H. Koch and B. J. Hrivnak, Astron. J. **86**, 438 (1981).

49. I. Goldman and T. Mazeh, Astrophys. J. **376**, 260 (1991).

50. J. L. Tassoul, Astrophys. J. **324**, L71 (1988).

51. M. Mayor and J.-C. Mermillard, in *IAU Symposium 105: Observational Tests of the Stellar Evolution Theory,* Ed. by A. Maeder and A. Renzini (Reidel, Dordrecht, 1984), p. 411.

52. G. Torres, D. W. Latham, T. Mazeh, *et al.*, in *IAU Symposium 151: Evolutionary Processes in Interacting Binary Stars,* Ed. by Y. Kondo, R. Sistero, and R. S. Polidan (Kluwer, Dordrecht, 1992), p. 491.

53. S. Piotrowski, Bull. Acad. Pol. Sci., Ser. Sci., Math., Astron. Phys. **12**, 419 (1965).

54. B. Paczynski, Ann. Rev. Astron. Astrophys. **9**, 183 (1971).

55. R. H. Koch, Bull. Am. Astron. Soc. **8**, 305 (1976).

56. A. V. Fedorova, D. V. Bisikalo, A. A. Boyarchuk, *et al.*, Astron. Zh. **77**, 357 (2000) [Astron. Rep. **44**, 309 (2000)].

57. L. R. Yungel'son and A. G. Masevich, Itogi Nauki Tekh., Ser. Astron. **21**, 43 (1982).

58. A. F. J. Moffat, S. V. Marchenko, P. Bartzakos, *et al.*, Astrophys. J. **497**, 896 (1998).

59. J. Greiner, J. G. Cuby, and M. J. McCaughrean, Nature **414**, 522 (2001).

60. E. A. Antokhina and A. M. Cherepashchuk, Pis'ma Astron. Zh. **14**, 252 (1988) [Sov. Astron. Lett. **14**, 105 (1988)].

61. P. Massey and P. S. Conti, Astrophys. J. **218**, 431 (1977).

62. A. M. Cherepashchuk, Mon. Not. R. Astron. Soc. **194**, 761 (1981).

63. A. M. Cherepashchuk, Usp. Fiz. Nauk **172**, 959 (2002).

Translated by N. Samus'

Model Atmospheres of Red Giants

Ya. V. Pavlenko

Main Astronomical Observatory, National Academy of Sciences of Ukraine, Goloseevo, Kiev, 03680 Ukraine
Received March 10, 2002; in final form, June 26, 2002

Abstract—Techniques and results of computations of model atmospheres are discussed for M and C giants and for giants with abundance anomalies. The SAM12 code, a modification of the ATLAS12 code developed by Kurucz, is used. Blanketing effects due to atomic and molecular line absorption are taken into account using the opacity-sampling approach. The computed model atmosphere for the Sun (G2V) is used as a test of the SAM12 code. The model red-giant atmospheres are compared with models reported in other studies. Comparisons between the computed and observed spectral energy distributions are given for the C giant WX Cyg (C-J6) and Sakurai's object (V4334 Sgr). © *2003 MAIK "Nauka/Interperiodica"*.

1. INTRODUCTION

The computation of model atmospheres for stars of late spectral types is an essential part of numerous astrophysical studies. Currently, several fairly detailed grids of model atmospheres are available [1–4], all based on similar approximations, such as LTE, plane-parallel geometry of the medium, and the absence of energy sources and sinks. Descriptions of techniques for computing such models can be found in a number of monographs [5, 6] and on the internet [4]. Considerable progress in this area has been possible due to the following.

(1) The computation of fairly complete sets of the atomic and molecular absorption lines that largely determine blanketing effects in the atmospheres of stars of late spectral types [2, 7–9].

(2) Quantum-mechanical calculations of the cross sections of free–bound absorption for a variety of atoms and ions [10].

(3) The development of codes to perform optimized calculations of opacities and convection that ensure rapid convergence of the iterative process of computing model atmospheres [2, 4].

(4) The use of high-performance computing facilities to solve astrophysical problems, which has made it possible to carry out extensive computations based on vast input arrays on reasonable time scales.

On the other hand, the acquisition of new observational data in recent years has increased the requirements for the model atmospheres to be used. The high-quality spectroscopic observations now available are sensitive even to tiny variations in elemental abundances, which is important first and foremost for refinements of our understanding of stellar structure and evolution. Note that, in some cases, such as studies of the chemical compositions of C giants,

the use of model grids available in the literature is difficult. The spectra of such stars depend on many parameters—the effective temperature T_{eff}, surface gravity $\log g$, metallicity $[\mu]$, ratio $C/O = \log N(C) - \log N(O)$, isotopic ratio $^{12}C/^{13}C = N(^{12}C)/N(^{13}C)$, turbulence velocity V_t, and abundances of individual elements. An even more interesting case is the task of modeling the spectra of R CrB stars, which are at later evolutionary stages and whose atmospheres are depleted in hydrogen.

Here, we are mainly concerned with computing model atmospheres for red giants. We present results for the model atmospheres and spectral energy distributions (SEDs) of M and C giants, which have substantially different chemical compositions. The sets of basic opacity sources are also different for these two types. We have also computed a new model-atmosphere grid for Sakurai's object.

The model for the solar atmosphere was used to test our techniques. On the whole, the computation of model atmospheres for dwarfs of late spectral types (K–M) has certain specific features associated with the dominant role of convection in the energy transport in these stars. Furthermore, dwarfs in the Galactic disk have mainly normal, i.e., solar, compositions. Virtually none of the abundance anomalies known for giants are present in K and M dwarfs.

2. THE COMPUTATIONAL PROCEDURE

We computed the model atmospheres using the SAM12 code, which is a modification of the AT-LAS12 code [11], and previous versions of our own codes for the computation of model atmospheres and synthesized spectra [12, 13]. We have made substantial changes in the opacity subroutines. The main advantage of SAM12 is its ability to compute model

atmospheres for stars with a given (generally, other than solar) chemical composition.

As in ATLAS12, the abundances of 99 elements were specified as input parameters. These did not vary with depth, and the microturbulence velocity was also assumed to be constant.

Opacities

We computed the cross sections for free−bound absorption by CI, NI, and OI atoms for SAM12 [14] using data from the TOPBASE database [10]. The opacity due to atomic and molecular absorption was taken into account using an opacity-sampling approach [15]. The absorption-coefficient profile over a line was specified by a Voigt function $H(a, v)$, with the damping constants taken from databases or computed using the Unsöld approximation [16].

A list of atomic and molecular absorption lines for $\lambda\lambda$ 40−60 000 nm was compiled based on various sources:

(1) a list of atomic lines from VALD [17];

(2) the molecular lines of H_2, ^{12}CN, ^{13}CN, $^{12}C_2$, $^{13}C_2$, $^{12}C^{13}C$, ^{12}CO, ^{13}CO, SiH, and MgH from Kurucz' CDROM 15 [2];

(3) a list of H_2O lines computed by us using the database of water levels and transitions of Partridge and Schwenke [8];

(4) the list of OH lines of Schwenke [18].

The SAM12 code takes into account the isotopic composition of the absorbing molecules, which is important for computing model atmospheres for red giants with low $^{12}C/^{13}C$ ratios (see Sections III.C and III.D).

Naturally, the set of opacity sources used in computing the model atmospheres of oxygen-sequence giants with $C/O < 1$ differed from that for C giants with $C/O > 1$. Absorption by TiO, VO, and H_2O plays the main role in the atmospheres of M giants, while absorption by carbon-containing molecules is most important in the atmospheres of C giants.

When computing the model atmospheres for M giants, we employed the JOLA technique realized in a version of the BIGF1 code [19] to take into account the absorption in TiO and VO molecular bands. This technique for calculating the opacity due to molecular band absorption makes it possible to reproduce not only the relative intensities of lines but also the overall SEDs of stars of late spectral types [20, 21].

Chemical Equilibrium

The system of equations for the ionization−dissociation equilibrium was solved for a mixture of more than 100 constituents. Computations for M and C giants were done for different sets of molecular species. The species and their ionization−dissociation equilibrium constants were chosen based on an analysis of the results of Tsuji [22]. For some molecules (TiO, VO, H_2O), we calculated the equilibrium constants using the most recent data available [23, 24].

Convection

The technique realized by Kurucz in the ATLAS12 code, based on a modified mixing-length theory, was employed to take into account convection. This technique is described in detail by Castelli *et al.* [25].

Synthesized Spectra

We computed the synthetic spectra[1] of red giants and compared them with the observed spectra. This was done using the WITA6 code [26] with the same opacity sources, chemical equilibrium constants, and sets of lines adopted in the model-atmosphere calculations. The synthesized spectra were computed in steps of $s = 0.005$ nm in the optical and in steps of $s = 0.05$ nm in the infrared. The effect of instrumental broadening was modeled using a convolution integral and was represented by a Gaussian profile. The computed and observed spectra were compared in terms of their normalized fluxes[2].

3. RESULTS

The Sun

Modeling the solar atmosphere is an essential step in testing available techniques for computing model stellar atmospheres [2, 27]. We also computed the solar atmosphere using the SAM12 code, using the abundances of [28] and taking molecules into account when calculating the ionization−dissociation equilibrium. The equation of radiative transfer was solved including the effects of continuum absorption and atomic and diatomic-molecular line absorption with a microturbulence velocity of $V_t = 2$ km/s. When calculating the convective energy transport, we specified the mixing-length parameter to be $l/H = 1.6$.

---

[1] In essence, our calculations yielded SEDs for the objects studied. However, to simplify the presentation, we use here the term "synthetic spectra."

[2] That is, the observed and computed fluxes reduced to a certain magnitude at a given wavelength were compared.
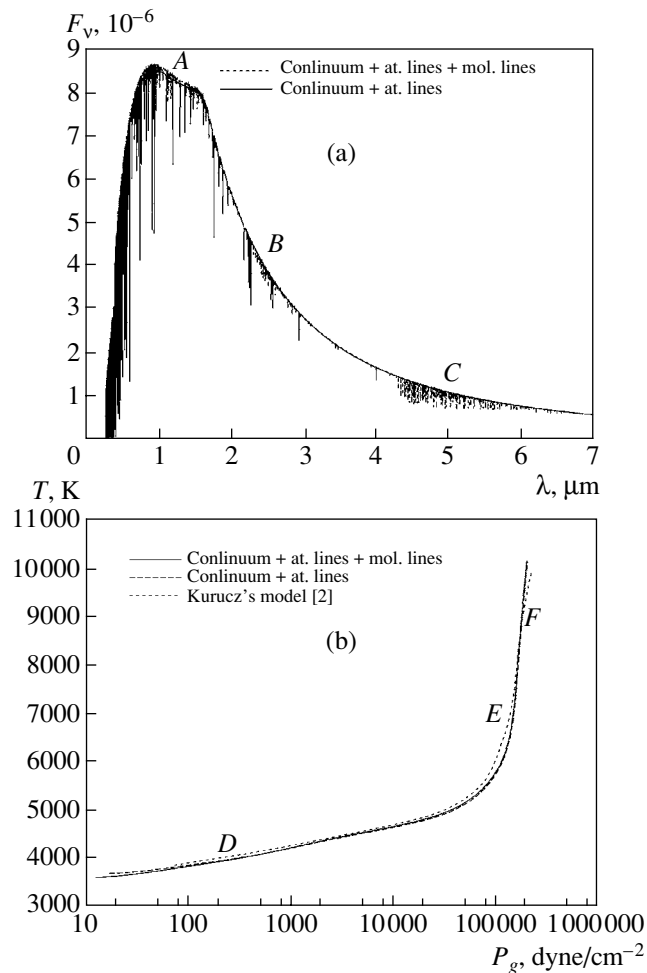
Fig. 1. (a) Theoretical energy distributions for the model atmospheres of the Sun computed with and without molecular absorption. (b) Temperature distribution in these models. The thermal structure of the model atmosphere of Kurucz [2] is also shown.

Absorption by negative hydrogen ions H^- dominates over other sources of continuum opacity in the solar atmosphere [6]. Atomic line absorption is important in the UV and optical (Fig. 1a). In the short-wavelength region of the solar spectrum, fairly strong isolated lines and bands of some molecules (OH, NH, etc. [29]) are observed. In the theoretical IR spectrum of the Sun, absorption in the first-overtone CO bands can be distinguished near ~ 1.2, ~ 2.4, and ~ 4.5 μm against the background of the relatively weak atomic absorption. In Fig. 1a, the letters A, B, and C label spectral intervals where CO bands with $\Delta v = 2$, 1, and 0 are situated. On the whole, molecular absorption is weak in the quiet solar photosphere. The temperature differences between model atmospheres of the Sun calculated with and without molecular absorption do not exceed several tens of kelvins.

Figure 1b compares our model with the model atmosphere of the Sun computed by Kurucz using the ATLAS9 code [2]. By and large, these model atmospheres are in satisfactory agreement. Small temperature differences (< 50 K) in the outer region, D in Fig. 1b, can be explained by the different ways in which blanketing effects were considered; specifically, Kurucz [2] determined the opacity distribution function using a different technique than ours. In region E, which represents the photospheric layers in the Kurucz model, the temperatures are higher. This is an effect of so-called penetrative convection, which was taken into account by Kurucz but neglected in our calculations. Finally, differences between the ATLAS9 and SAM12 codes in their treatment of convective energy transport and opacities and in their temperature-correction procedures are manifest in the deepest layers (region F).

M Giants

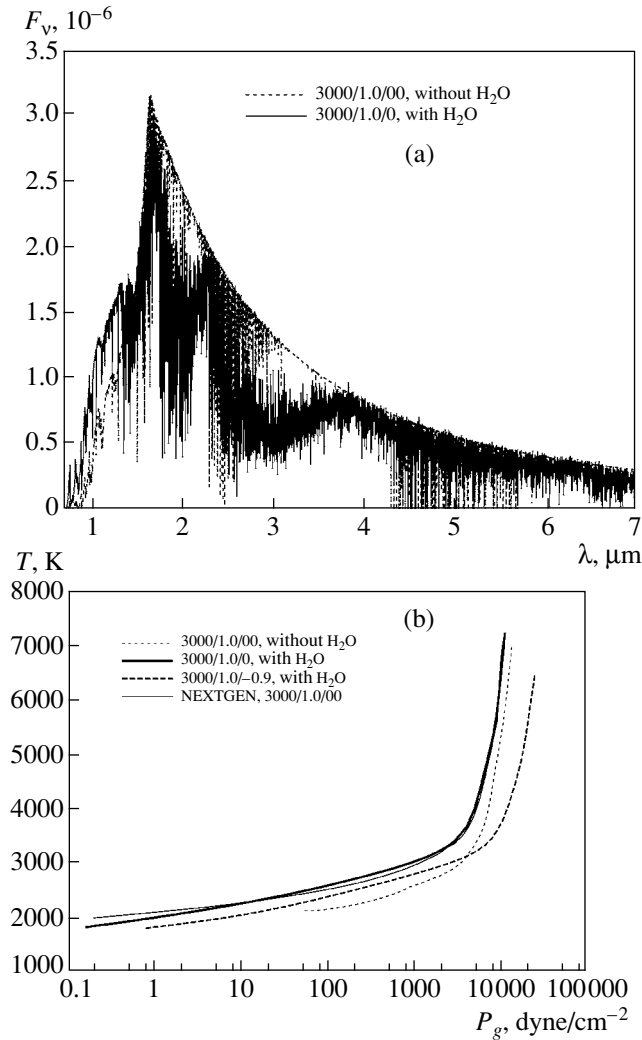Blanketing effects in the atmospheres of M giants are associated with absorption by the electron

Fig. 2. (a) Theoretical energy distributions for the model atmospheres of M giants computed with and without H_2O absorption. (b) The temperature distribution for these models. The thermal structures of the model atmospheres 3000/1.0/-0.9 and 3000/1.0/0 from the NEXTGEN [4] grid is also shown.

systems of VO and TiO bands in the optical and by rotational–vibrational H_2O bands, as well as by the fundamental-band systems of OH, CN, and CO molecules in the IR [30]. In particular, the inclusion of H_2O absorption is crucial when computing model atmospheres of M giants (Fig. 2a; see also [4]). The molecular H_2O bands dominate in the IR, where the SEDs of red giants reach their maxima.

We have computed a grid model atmospheres for M giants ($T_{eff} = 3000 \ldots 4000$ K, $\log g = 0 \ldots 2$, $[\mu] = 0 \cdots -2$) including absorption by H_2O and diatomic molecules. For a number of M-giant model atmospheres, we adopted elevated carbon abundances (see below). The calculations were done for a microturbulence velocity of $V_t = 2$ km/s and a mixing-length parameter of $l/H = 2$.

The M-giant model atmosphere for $T_{eff}/\log g/[\mu] =$ 3000/0.0/0 computed using the SAM12 code agrees well with the models of the NEXTGEN grid (Allard *et al.* [31]), which were also obtained under classic approximations (Fig. 2b). As the metallicity of the model atmosphere is reduced, its photosphere shifts to higher pressures (Fig. 2b) due to the reduction of the opacity of its material.

We investigated the effect of possible variations in the C/O ratio on the structure of the model atmospheres of M giants. This question is of interest in the context of refining our estimates of the evolutionary status of M giants in the bar of our Galaxy. This requires the resolution of the following well-known issue. The intensities of the TiO bands in the spectra of M giants exhibit a dependence on C/O [32], and this ratio can vary in the course of the evolution of M giants. On the other hand, vari-
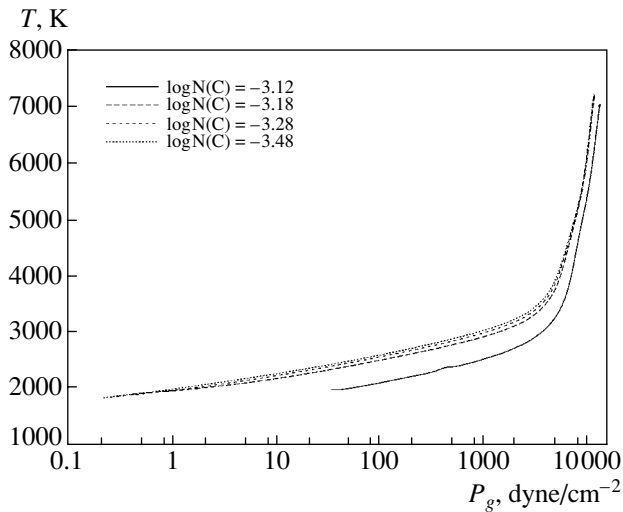
Fig. 3. Temperature differences between the model atmospheres for M giants with $T_{\rm eff}/\log g/[\mu] = 3000/0.0/0$ and various $\log N({\rm C})$. The oxygen content is $\log N({\rm O}) = -3.11$ in all cases.

ations in C/O can affect the structure of the model atmosphere of the star and, therefore, its spectrum. To study these effects, we computed a number of 3000/0.0 model atmospheres for an M giant with solar chemical composition and various carbon contents $\log N({\rm C}) = -3.48 \cdots -3.12$[3].

Our comparison of the computed model atmospheres shows that, for $\log N({\rm C}) = -3.48$ (the solar value) $\cdots -3.18$, the structure of the model atmosphere is fairly insensitive to variations in the carbon abundance. As already noted, blanketing effects in the atmospheres of M giants are mainly due to absorption by H_2O, which varies little with variations in C/O. However, as the C/O ratio is further increased and approaches unity, the molecular concentrations of H_2O substantially decrease. This reduces the blanketing effects, thereby influencing the structure of the model atmosphere (Fig. 3).

C Giants

It is characteristic of C giants that C/O > 1 in their atmospheres, i.e., they have more carbon atoms than oxygen atoms. When calculating our model atmospheres for C giants, we took into account the most abundant carbon-containing molecules, including the molecules whose band absorption is responsible for blanketing effects, i.e., C_2, CO, and CN (Fig. 4a). The opacity of the material in the atmospheres of C stars—and, therefore, their spectra

[3]We use here an abundance scale in which $\sum N_i = 1$ and the solar hydrogen abundance is $\log N({\rm O}) = -3.11$ [28].
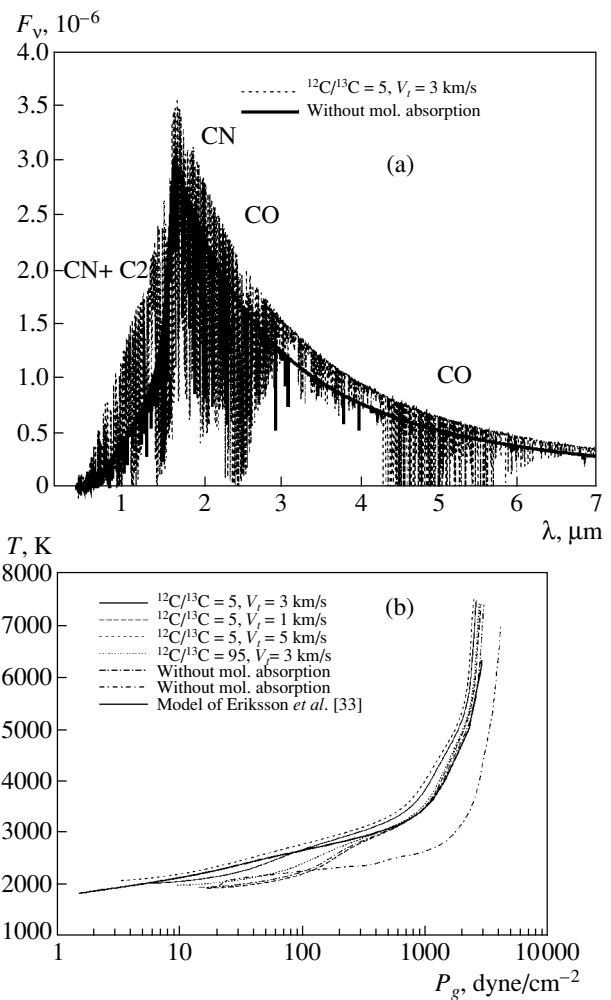
Fig. 4. (a) Theoretical energy distributions for the model atmospheres of C giants 3000/0.0/0/0.1 computed with and without molecular absorption. (b) Theoretical distributions of temperature as a function of gas pressure in several model atmospheres for C giants 3000/0.0/0/0.1 calculated for various sets of input parameters. The temperature distribution in the model atmosphere of Eriksson et al. [33] is also shown.

(and model atmospheres)—are highly sensitive to C/O, the isotopic ratio ^{12}C/^{13}C, the metallicity $[\mu]$, and the microturbulence velocity V_t [33] (see also Fig. 4b).

We computed a grid of model atmospheres for C giants with $T_{\rm eff} = 2800 \ldots 4500$ K, $\log g = 0.0$, ^{12}C/^{13}C = 3 \ldots 10, and $V_t = 3$ km/s. Figure 4b illustrates a comparison of the structure of the computed C-giant model atmosphere for $T_{\rm eff}/\log g/[\mu]/(C/O) = 3000/0.0/0/0.1$ with the model constructed by Eriksson et al. [33] using the MARKS code [1] and these same parameters. By and large, the two models agree satisfactorily in terms of the structure of the atmospheric layers where the
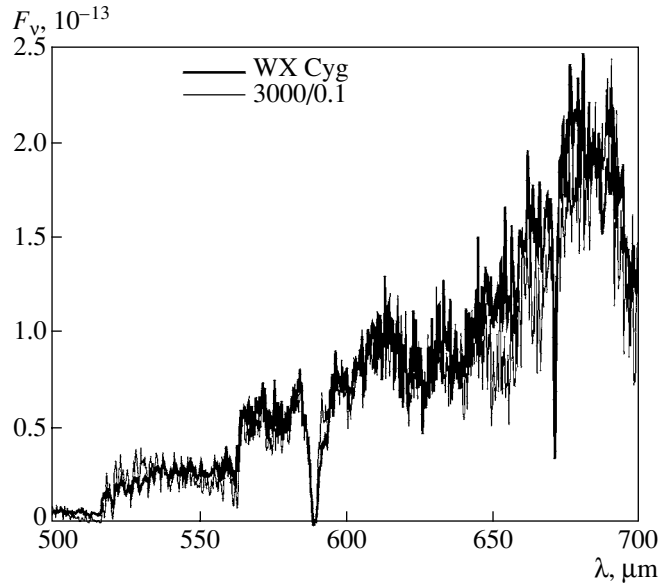
Fig. 5. Comparison of the observed SED for WX Cyg (C-J6) [34] with the SED computed for the model atmosphere 3000/0.0/0/0.1. The theoretical spectrum was convolved with a Gaussian function for $\Delta_\lambda = 0.2$ nm.
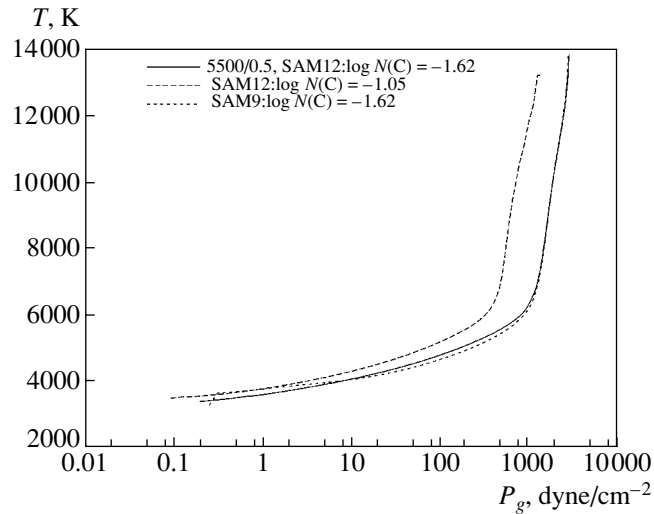

Fig. 6. Thermal structure of the model atmospheres of Sakurai's object computed using the SAM9 [12] and SAM12 codes. The temperature distribution in the atmosphere at an increased carbon abundance, $\log N(C) = -1.05$, is also shown.

atomic and molecular absorption lines are formed. Only small temperature differences (< 100 K) in the outer part of the model ($P_g < 6$ dyn/cm^2, $\tau_{\text{ross}} < 0.005$) can be noted, apparently due to differences in the techniques used to take into account opacity. In particular, we did not include absorption by polyatomic molecules, which may play an important role in the outer atmospheric layers of C giants. However, the structure of this part of the atmosphere strongly depends on the set of input parameters—the isotopic ratio ^{12}C/^{13}C and microturbulence velocity V_t (Fig. 4b).

In deeper atmospheric layers ($P_g > 500$ dyn/cm^2, $\tau_{\text{ross}} > 1/3$), discrepancies are mainly due to differences in the techniques employed in the MARKS and SAM12 codes to take into account convective energy transport and compute the continuum opacities.

A comparison between the SED of the giant WX Cyg [34] and the SED computed for the 3000/0.0/0/0.1 model atmosphere is given in Fig. 5. This star is among known C giants with elevated lithium abundances in their atmospheres ($\log N(\text{Li}) > 4$ [35]). Calculations were done for ^{12}C/^{13}C = 5 and $V_t = 3$ km/s [35]. The computed

and observed SEDs are basically in satisfactory agreement. The observed spectrum is better reproduced in the range $\lambda\lambda$ 500−650 nm; the differences at longer wavelengths are apparently due to specific features of the chemical composition of WX Cyg, which have not yet been determined. The theoretical spectral lines in this range are less intense than the observed lines. Thus, the noted differences cannot be attributed to incompleteness of the sets of molecular lines used. Unfortunately, a detailed discussion of this issue goes beyond the scope of this paper. However, we plan to investigate the spectrum of WX Cyg in the future.

Sakurai's Object

Sakurai's object (V4334 Sgr) provides an example of extremely rapid stellar evolution at the stage of the last helium flare [36]. This star, discovered in February 1996 as a nova-like object in Sagittarius ($V \sim 15^m$), exhibited a rapid growth in luminosity by 3^m within a few months. By 1997, the luminosity had grown by another 2^m, after which it started decreasing, with the appearance of some phenomena associated with the formation of dust [37]. Further, a rapid decline in luminosity was observed in 1998, and the object completely disappeared ($V > 22^m$ in the optical) in 1999.

Asplund et al. [38, 39] and Kipper and Klochkova [40] demonstrated that the object had a peculiar chemical composition, similar to that of R CrB stars. The abundances of hydrogen, helium, and carbon in the atmosphere of Sakurai's object are −2.42, −0.02, and −1.62, respectively, so that hydrogen is only the third element in terms of abundance [39]. These studies of the chemical composition of Sakurai's object were based on spectra obtained in 1996, which were similar to those of F supergiants but with missing or faint molecular bands. The further cooling of the photosphere of Sakurai's object rendered its optical spectrum similar to that of C giants, with absorption bands of CN and C_2 becoming visible. Naturally, the analysis of these spectra requires model-atmosphere computations for Sakurai's object, which we have done [13, 21, 41].

We computed a new grid of model atmospheres for Sakurai's object for $T_{eff} = 5000 \ldots 6000$ K and $\log g = 0 \ldots 1$. The abundances reported by Asplund et al. [39] were adopted; to calculate the opacities, we used the set of molecular lines of Kurucz [2] and the VALD [17] set of atomic lines.

Figure 6 compares the thermal structures of the model atmospheres we used previously [21] to analyze the optical spectra of Sakurai's object observed in 1997 and our new model atmospheres computed using the SAM12 code. The earlier models were
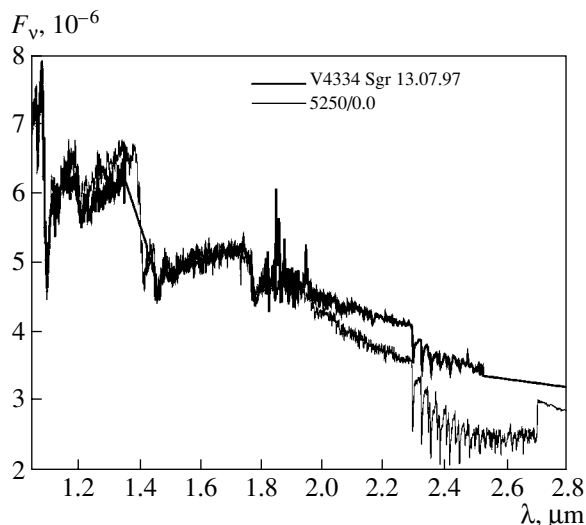

F_ν, 10^{-6}

Fig. 7. Comparison of the observed SED for Sakurai's object in the IR [37] and the computed SED for the 5500/0.0 model atmosphere obtained using the elemental abundances reported by Asplund et al. [39]. The theoretical spectrum was convolved with a Gaussian function $\Delta_\lambda = 1.2$ nm. For $\lambda > 2.7$ μm, fluxes in the theoretical continuum are shown.

computed using the JOLA technique to include the molecular opacity; in our new models, the opacity was calculated using the opacity-sampling approach. These models agree well, despite the substantial differences in the calculation techniques. However, this is not surprising, since the JOLA approximation is quite appropriate for descriptions of strong and saturated molecular bands [19, 43], which were typical of Sakurai's object in 1997−1988 [21, 41].

To illustrate the sensitivity of the model atmosphere for Sakurai's object to the input parameters, Figure 6 shows the variations in the thermal structure of the model as the carbon abundance is increased to $\log N(C) = −1.05$ (for a discussion of the "carbon paradox," see Asplund et al. [38]).

In spite of the intricate computations required for the model atmospheres of Sakurai's object, the model SEDs prove to be fairly realistic when compared to the observations (Fig. 7; see also [21, 41]). They reproduce the observed SED over a wide wavelength range using a self-consistent approach that includes the computation of both model atmospheres and SEDs for a unified set of abundances and opacity sources.

At the same time, the theoretical modeling reveals certain new effects in the observed spectrum. In particular, the IR excess observed at $\lambda\lambda > 2\mu$m (see Fig. 7) is, to all appearances, due to thermal emission of the dust envelope at these wavelengths; this envelope began forming around Sakurai's object

early in 1997. Such effects are considered at length in [42].

DISCUSSION

Our model atmospheres for red giants and the Sun are based on classic approximations. The opacity sources in the atmospheres of these stars are substantially different, which naturally affects their SEDs. Our main concern was with the computed model atmospheres of the stars in post-main-sequence evolutionary stages. Their chemical compositions can change substantially within relatively short intervals. The problem, however, is that absorption by H, C, N, O, and metals (as well as by molecules in which these atoms are present) largely determines the blanketing effects in the atmospheres of stars of late spectral types. Moreover, any change in the abundances of H, C, N, or O affects the structure of the model atmosphere of the star. A quantitative analysis of their spectra is possible only if it is based on self-consistent computations of model atmospheres and abundance determinations [44]. This is primarily true of analyses of the spectra of C stars, whose spectra respond to even slight (≤ 0.001 dex) variations in C/O.

Note that the computation of model atmospheres for red giants including both continuum and atomic and molecular line absorption can currently be done even on only moderately powerful personal computers, although the need to use large data arrays poses some problems. The opacity-sampling approach enables us to consider all characteristic features of the chemical composition of a particular star. Thus, we were able to compute a model atmosphere for Sakurai's object that is quite suitable for specific astrophysical studies, although the chemical composition of this object differs strongly from the solar composition.

Naturally, certain well-known factors can affect the reliability of the computed model atmospheres. Among these, the completeness of the set of opacity sources taken into account is particularly important.

Our current understanding of the sources of continuum absorption in stars with normal chemical compositions appears to be fairly adequate, although some investigators have indicated problems related to the UV spectra of stars [29, 45]. These can probably be resolved within a traditional approach, including numerous faint atomic and molecular lines [46] and taking into account free−bound absorption by a larger number of metals. Obviously, solving these problems is of special interest when modeling the atmospheres of stars with abundance anomalies, especially hydrogen-depleted stars, in whose atmospheres free−bound absorption by C, N, O, and metals can dominate over wide wavelength ranges [12].

The completeness of the set of atomic and molecular lines used remains an important factor. Our use of rather complete recent sets of lines of H_2O [8, 47] and diatomic molecules [2, 9, 18] made it possible to substantially improve the reliability of the model atmospheres for C and M giants. The calculation of improved sets of lines is ongoing (for a discussion, see [24]).

At the same time, evaluating the reliability of sets of lines used in computations is, in fact, a separate problem. Quantitative estimates can be obtained by comparing the computed and observed SEDs for stars whose chemical compositions can be determined with certainty. However, this requires that the model atmospheres be computed taking into account all known opacity sources, in particular, line absorption by a given atom or molecule. Obviously, this problem can be solved only through an iterative process.

There is no doubt that the correct calculation of convective energy transport in the stellar atmospheres has great importance in the construction of model atmospheres for red giants, since the photosphere of a red giant is essentially the top boundary of the convective envelope. We modeled convective-energy transport using the principles of mixing-length theory. However, this approximation is known to have insufficient accuracy in some cases, especially for high-luminosity giants [48]. Certain other issues are also encountered in this context, such as allowances for mass losses, chromospheric effects, and sphericity effects. A detailed analysis of these questions goes beyond the scope of this paper; various aspects of these problems are discussed in other studies [6, 38].

To conclude, we note that, despite some problems that remain to be resolved, the use of contemporary model atmosphere makes it possible to describe SEDs not only in relatively narrow spectral intervals, but also over a wide wavelength range from the UV to the IR, even for the spectra of peculiar objects such as Sakurai's object.

In principle, the SAM12 code can be used to model atmospheres over fairly broad ranges of luminosity, effective temperature, and metallicity. The code can be further improved to cover more peculiar stellar atmospheres. The collaboration of astrophysicists interested in the subject is welcome.

REFERENCES

1. R. A. Bell, K. Eriksson, B. Gustafsson, and A. Nordlung, Astron. Astrophys., Suppl. Ser. **23**, 37 (1976).
2. R. L. Kurucz, CD ROM No. 1-22 (Smithsonian Astrophysical Observatory, Cambridge, 1993).
3. F. Allard and P. H. Hauschildt, Astrophys. J. **445**, 433 (1995).
4. P. Hauschildt, F. Allard, J. Ferguson, *et al.*, Astrophys. J. **525**, 871 (1999).
5. R. L. Kurucz, *ATLAS: A Computer Program for Calculating Model Atmospheres* (Smithsonian Astrophysical Observatory, 1970), Spec. Report, No. 309, p. 1.
6. D. Michalas, *Stellar Atmospheres* (Freeman, San Francisco, 1978).
7. B. Plez, Astron. Astrophys. **337**, 495 (1998).
8. H. Partrige and D. Schwenke, J. Chem. Phys. **106**, 4618 (1997).
9. D. Goorvitch, Astrophys. J., Suppl. Ser. **95**, 535 (1994).
10. M. J. Seaton, Rev. Mex. Astron. Astrofis. **23**, 180 (1992).
11. R. Kurucz, http://cfaku5.harvard.edu/molecules/H2O/ (1999).
12. Ya. V. Pavlenko, Astron. Zh. **76**, 115 (1999) [Astron. Rep. **43**, 94 (1999)].
13. Ya. V. Pavlenko and L. A. Yakovina, Astron. Zh. **77**, 243 (2000) [Astron. Rep. **44**, 209 (2000)].
14. Ya. V. Pavlenko and C. Zhukovskaya, Kinematika Fiz. Nebesnykh Tel (2002).
15. C. Sneden, H. Johnson, and B. Krupp, Astrophys. J. **204**, 281 (1976).
16. A. Unsold, *Physics der Sternatmospharen* (Springer-Verlag, Berlin, 1995).
17. F. Kupka, N. Piskunov, T. A. Ryabchikova, *et al.*, Astron. Astrophys., Suppl. Ser. **138**, 119 (1999).
18. D. Schwenke, http://george.arc.nasa.gov/~dschwenke (1999)
19. S. E. Nersisyan, A. V. Shavrina, and A. A. Yaremchuk, Astrofizika **30**, 249 (1989).
20. Ya. V. Pavlenko, Astrophys. Space Sci. **253**, 43 (1997).
21. Ya. V. Pavlenko, L. A. Yakovina, and H. W. Duerbeck, Astron. Astrophys. **354**, 229 (2000).
22. T. Tsuji, Astron. Astrophys. **23**, 411 (1973).
23. Ya. V. Pavlenko, Astron. Zh. **76**, 847 (1999) [Astron. Rep. **43**, 748 (1999)].
24. Ya. V. Pavlenko, Astron. Zh. **79**, 627 (2002) [Astron. Rep. **46**, 567 (2002)].
25. F. Castelli, R. G. Graton, and R. L. Kurucz, Astron. Astrophys. **318**, 841 (1997).
26. Ya. V. Pavlenko, Astron. Zh. **77**, 254 (2000) [Astron. Rep. **44**, 219 (2000)].
27. A. S. Gadun and Ya. V. Pavlenko, Astron. Astrophys. **281**, 324 (1997).
28. E. Anders and N. Grevesse, Geochim. Cosmochim. Acta **53**, 197 (1989).
29. L. A. Yakovina and Ya. V. Pavlenko, Kinematika Fiz. Nebesnykh Tel **14**, 257 (1998).
30. T. Tsuji, Astrophys. J. **538**, 801 (2000).
31. F. Allard, P. Hauschildt, and D. W. Schwenke, Astrophys. J. **540**, 1005 (2000).
32. D. Kotnik-Karuza, R. Jurdana-Sepic, and Y. P. Pavlenko, New Astron. Rev. **45**, 573 (2001).
33. K. Eriksson, B. Gustafsson, U. G. Jorgensen, and A. Nordlund, Astron. Astrophys. **132**, 37 (1984).
34. C. Barnbaum, R. P. S. Stone, and P. C. Keenan, Astrophys. J., Suppl. Ser. **105**, 419 (1996).
35. C. Abia, Y. V. Pavlenko, and P. de Laverny, Astron. Astrophys. **351**, 273 (1999).
36. H. W. Duerbeck and S. Benetti, Astrophys. J. **468**, L111 (1996).
37. T. G. Geballe, A. Evans, B. Smalley, and S. P. S. Eyres, Astrophys. Space Sci. **279**, 39 (2002).
38. M. Asplund, B. Gustafsson, D. L. Lambert, and N. K. Rao, Astron. Astrophys. **321**, L17 (1997).
39. M. Asplund, D. L. Lambert, T. Kipper, *et al.*, Astron. Astrophys. **343**, 507 (1999).
40. T. Kipper and V. Klochkova, Astron. Astrophys. **324**, L65 (1997).
41. Ya. V. Pavlenko and H. W. Duerbeck, Astron. Astrophys. **367**, 933 (2001).
42. Ya. V. Pavlenko and T. R. Geballe, Astron. Astrophys. **390**, 621 (2002)).
43. T. Tsuji, *Molecules in the Stellar Environment,* Ed. by U. G. Jorgensen (Denmark, Copenhagen, 1993).
44. Ya. V. Pavlenko and L. A. Yakovina, Astron. Zh. **71**, 863 (1994) [Astron. Rep. **38**, 768 (1994)].
45. R. A. Bell and S. Balachanran, Nature **392**, 791 (1998).
46. R. L. Kurucz, *South American Tour. Summer 1991,* Preprint No. 3348, Harvard-Smithson. Cen. Astrophys. (1991).
47. U. G. Jorgensen, P. Jensen, G. O. Sorensen, and B. Aringer, Astron. Astrophys. **372**, 249 (2001).
48. M. Schwarzchild, Astrophys. J. **195**, 137 (1975).

Translated by A. Getling

Proper Motions of Open Star Clusters and the Rotation Rate of the Galaxy

A. V. Loktin and G. V. Beshenov

Astronomical Observatory, Ural State University, Yekaterinburg, Russia

Received November 30, 2001; in final form, June 26, 2002

Abstract—The mean proper motions of 167 Galactic open clusters with radial-velocity measurements are computed from the data of the Tycho-2 catalog using kinematic and photometric cluster membership criteria. The resulting catalog is compared to the results of other studies. The new proper motions are used to infer the Galactic rotation rate at the solar circle, which is found to be $\omega_0 = +24.6 \pm 0.8$ km s^{-1} kpc^{-1}. Analysis of the dependence of the dispersion of ω_0 estimates on heliocentric velocity showed that even the proper motions of clusters with distances $r > 3$ kpc contain enough useful information to be used in kinematic studies demonstrating that the determination of proper motions is quite justified even for very distant clusters. © *2003 MAIK "Nauka/Interperiodica".*

1. INTRODUCTION

The proper motions of Galactic objects carry important information about their kinematic properties. Until the last decade, proper motions of open star clusters (OCs) were of virtually no use for kinematic studies because of the presence of large random and systematic errors. This is especially true of clusters at large heliocentric distances. The situation changed considerably after the release of catalogs based on accurate measurements of stellar positions by the Hipparcos satellite. One such catalog is Tycho-2 [1], which gives proper motions computed using Hipparcos position measurements and the "Carte du Ciel" photographic positions as the first-epoch data. The large difference between epochs and high precision of the second-epoch positions, combined with the high completeness down to a limiting magnitude of about $V = 13^m$, make this catalog an excellent data source for the determination of mean proper motions of OCs. Two new extensive lists of mean proper motions of OCs have been published in recent years by Baumgardt *et al.* [2] and a group of Brazilian astronomers (Dias *et al.* [3]). Baumgardt *et al.* [2] determined the mean proper motions of 360 OCs using the proper motions of the Hipparcos catalog [4], whereas Dias *et al.* [3] determined the proper motions of 112 OCs within 1 kpc of the Sun using the data of the Tycho-2 catalog.

Our group began almost simultaneously with the above authors to determine the proper motions of OCs using the Tycho-2 data. Our primary aims were to obtain reliable data for the determination of the frequency of the Galactic rotation at the solar circle, having in mind the future determination of other kinematic parameters of the Galactic disk, and to collect data for verifying the cluster membership of particular individual stars. The above studies have certain drawbacks in this respect. For example, the proper-motion determinations of Baumgardt *et al.* [2] are based on the Hipparcos catalog, whereas the Tycho-2 catalog contains much more accurate proper motions as far as systematic errors are concerned, and has a somewhat deeper limiting magnitude, allowing more cluster members to be used to determine the mean proper motion. This last point is of greatest importance for distant and poor clusters. The Brazilian team [3] determined proper motions only for clusters located relatively close to the Sun, whereas the kinematic parameters of the Galactic disk should be better determined from the OCs that are most distant from the Sun.

It is of interest to analyze the repeatability of the determinations of the open-cluster proper motions. Together with the very large relative errors in proper motions due to the substantial heliocentric distances of most of the clusters, the use of different catalogs and different membership criteria has resulted in significant differences between the OC proper motions determined by different authors. It is therefore important to test to what extent the use of new data based on Hipparcos observations has improved the repeatability of results.

In view of the above, computing the mean proper motions of OCs is a task of vital importance. In this work, we discuss estimates of the mean proper motions of clusters with available radial-velocity measurements without imposing any restrictions on the heliocentric distances of clusters. We test the reliability of the proper-motion estimates for the most distant
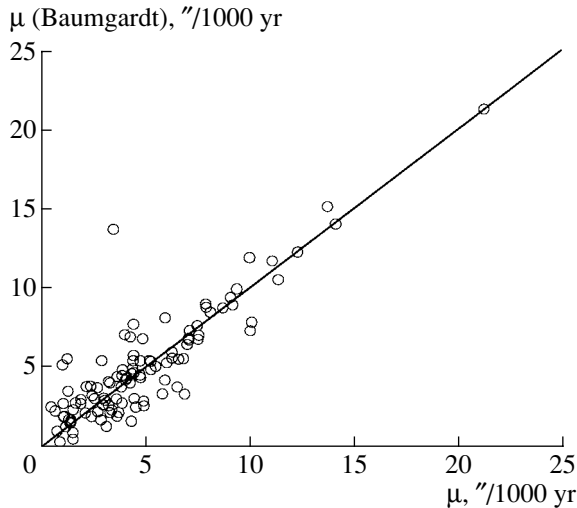
μ (Baumgardt), ″/1000 yr

Fig. 1. Comparison of the absolute values of proper-motion vectors of open clusters determined by Baumgardt *et al.* [2] (y axis) with the results of this work (x axis).
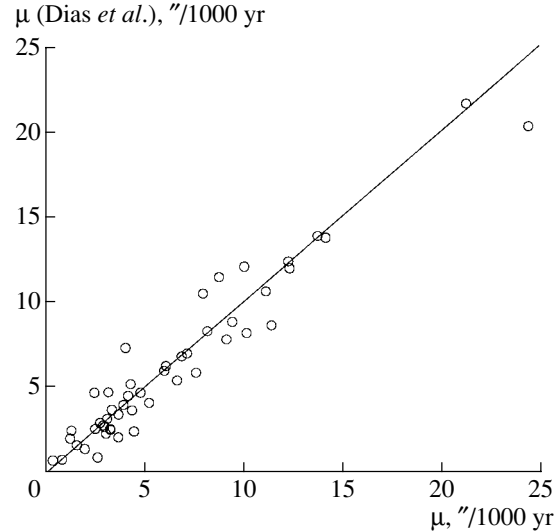
μ (Dias *et al.*), ″/1000 yr

Fig. 2. Same as Fig. 1 for the clusters from Dias *et al.* [3].

OCs by using them to estimate the frequency Ω_0 of the Galactic rotation at the solar circle, which is an extremely important parameter of the Galactic disk.

2. PROPER MOTIONS

We determined the proper motions of the clusters of our sample as follows. We selected from the Tycho-2 catalog all stars within a wide neighborhood of the cluster considered. We always chose a large area in order to include the greatest possible number of cluster members, including corona stars. We analyzed areas of sky of diameter 4° for the nearest clusters (Pleiades, Praesepe) and 2° for the most distant clusters. We excluded from the resulting sample stars with proper-motion components exceeding $0.1''$/yr, since such stars carry virtually no information about the distribution of proper motions in areas of sky containing distant clusters. We then applied a photometric criterion to select cluster members. We used our computer atlas of $V - (B-V)$ diagrams to determine the domain on this diagram occupied by the cluster stars and selected stars falling within this domain according to the Tycho-2 photometry. Stars lying outside this domain were excluded from the sample. Our analysis allowed for the fact that the errors of the Tycho-2 photometry increase substantially toward the limiting magnitude of the catalog.

Our next step was to determine the centers and dispersions of the distributions of proper motions of cluster members and Galactic field stars. To this end, we used a method similar to that of Sanders [5]. In particular, for the remaining sample stars, we constructed a histogram of the two-dimensional distribution of proper motions and fitted it to a sum of two

two-dimensional normal distributions by minimizing the sum of squared residuals. Unlike Sanders [5], we used a symmetric normal distribution described by a single dispersion for both cluster members and Galactic field stars. This simplification can be justified by the fact that, once fast-moving stars and stars that do not obey the photometric criterion are excluded, the remaining sample is free of most of the nearest Galactic foreground stars, and the distribution of the remaining stars with small proper motions is determined mostly by the proper-motion errors, which are symmetric to a first approximation.

We believe that adopting this approximation is no worse than either ignoring the deviation of the distribution of field-star proper motions from a two-dimensional Gaussian or ignoring nonzero covariances in the distribution of these stars. At the same time, we have one parameter less to determine, thereby simplifying the search for the parameters of the distribution, which we determine using a coordinate descent method. Since our aim was to infer the mean proper motions and not to identify cluster members, we applied the photometric membership criterion in its tightest form, leaving only stars that definitively lie in the domain of the $V - (B-V)$ diagram occupied by cluster members.

We were able to determine the proper motions for a total of 167 clusters for which we could find published radial velocities. Figures 1 and 2 compare the absolute values of the proper-motion vectors for the clusters of our sample (x axis) with those computed by Baumgardt *et al.* [2] and Dias *et al.* [3], respectively. In both cases, the proper-motion lists agree satisfactorily with each other. The somewhat larger dispersion of the data points in Fig. 1 is due to the
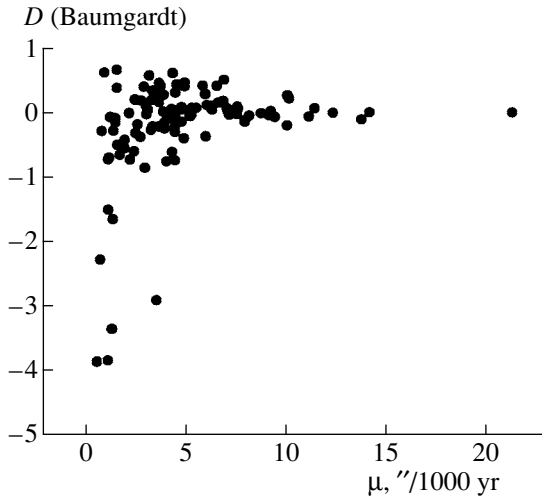
LOKTIN, BESHENOV

D (Baumgardt)

Fig. 3. Relative proper-motion differences for clusters from the list of Baumgardt *et al.* [2].
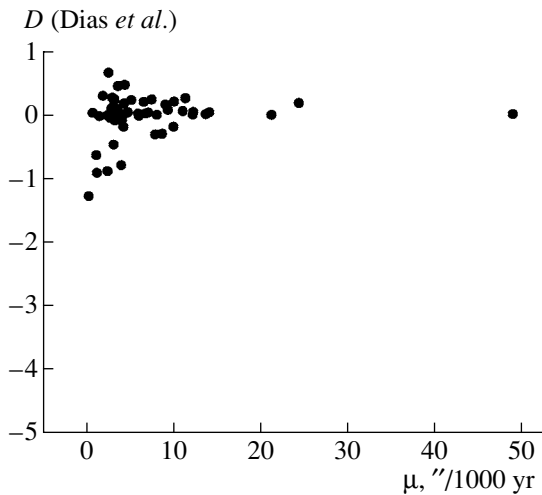
D (Dias *et al.*)

Fig. 4. Same as Fig. 3 for the clusters from Dias *et al.* [3].

greater heliocentric distances of the clusters considered by Baumgardt *et al.* [2] and the somewhat lower accuracy of proper motions in the Hipparcos catalog compared to those of Tycho-2. The list of Baumgardt *et al.* [2] contains quite a large number of clusters with mean proper motions determined from one to three stars. For the most deviant object in Fig. 1—the poor Lynga 6 cluster—the result of Baumgardt *et al.* [2] must be incorrect, because a proper motion of $14''/1000$ yr seems too high for such a distant object ($r \approx 1600$ pc), even for a cluster seen toward the Galactic center.

Another method for assessing the agreement between the results of different determinations of OC proper motions is to analyze the relative differences $D = (\mu - \mu_{\mathrm{ref}})/\mu$, where μ and μ_{ref} are the absolute

values of the proper-motion vectors computed in this paper and determined in other studies. Figures 3 and 4 show the dependences of the relative differences on μ for comparisons with the lists of Baumgardt *et al.* [2] and Dias *et al.* [3], respectively. Figure 3 shows that, of 107 OCs in common between our list and that of Baumgardt *et al.* [2], only seven exhibit large relative deviations. The relative deviations between our results and those of Dias *et al.* [3] shown in Fig. 4 are even smaller. The mean relative deviations when comparing with the lists of Baumgardt *et al.* [2] and Dias *et al.* [3] are $\bar{D} = -1.53 \pm 0.39$ and $\bar{D} = -0.04 \pm 0.05$, respectively. In the former case, the mean deviation is mostly determined by the effect of several strongly deviating clusters. Thus, the mean deviations demonstrate good repeatability of the proper-motion determinations based on somewhat different data and using different criteria for selecting OC members. Note that, for 49 out of 50 clusters in common between our list and that of Dias *et al.* [3] (Fig. 4), the relative deviations do not exceed unity, so that the proper motions, on average, exceed their errors.

3. FREQUENCY OF THE GALACTIC ROTATION AT THE SOLAR CIRCLE

The frequency ω_0 of the rotation of the Galactic disk at the solar circle is one of the principal parameters of our stellar system inferred from observations, since ω_0 determines the scale of the Galactic rotation curve. In most studies, this quantity has been determined as the difference of Oort's constants $\omega_0 = A - B$. Loktin and Gerasimenko [5] proposed to abandon the practice of expanding the velocity field into a power series of a small parameter—the heliocentric distance—in favor of estimating ω_0 directly from the formulas for a circular velocity field

$$\begin{cases} v_r = R_0 \left[\omega(R) - \omega_0\right] \sin l \cos b, \\ v_l = R_0 \left[\omega(R) - \omega_0\right] \cos l \cos b - \omega(R) r \cos b, \end{cases} \quad (1)$$

where v_r and v_l are the radial and tangential velocities of the object corrected for the solar space motion, R_0 is the distance of the Sun from the Galactic-rotation axis, r is the heliocentric distance of the object, and l and b are the Galactic longitude and latitude of the object. By solving the system (1) for ω_0, we obtain, by canceling the function $\omega(R)$,

$$\omega_0 = \frac{v_r(R_0 \cos l - r \cos b) - v_l R_0 \sin l \cos b}{R_0 r \sin l \cos^2 b}. \quad (2)$$

We used this formula to estimate the mean ω_0 from our sample of OCs for which both radial velocities and our mean proper motions were available. We adopted

the cluster distances from the current version of our "Homogeneous catalog" [6] with the distance scale matched to the system of the Hipparcos trigonometric parallaxes [7]. We adopted the components of the solar space motion from [8], where they are determined relative to stars with circular Galactic orbits. We adopted the solar Galactocentric distance of $R_0 = 8.3 \pm 0.3$ kpc of Geresimenko [9], who determined it from OC data given in the "Homogeneous catalog" on the same distance scale as we use in this paper.

Note that we did not correct the distribution of heliocentric distances of the clusters in our sample for the effect of random errors, since the average error in the OC distance moduli is small, and the corrections, which are also random quantities, are also small. Justified statistical corrections for such a small sample as ours are impossible to obtain when the distance accuracy varies strongly from cluster to cluster, as is the case in this work.

We derived individual estimates of the Galactic rotation frequency for each cluster of the sample. We excluded 26 OCs with the smallest denominators in formula (2). These clusters are seen at Galactic longitudes within $\pm 10°$ of the directions toward the Galactic center and anticenter, and objects at different Galactic longitudes contain different amounts of information about the rotation of the disk. Figure 5 shows the distribution of the individual estimates of ω_0. In the distribution of the accumulated weights SP, a weight for each OC is computed by multiplying quantities proportional to the quality of the observational data (heliocentric distances, radial velocities, and proper motions) and inversely proportional to the denominator in formula (2). The resulting distribution differs appreciably from a normal law and has a prominent central component, which contains the "mode" and wings made up of estimates obtained mainly for OCs located in the solar vicinity (see below) and those whose initial data are of poor quality.

The strong wings of the distribution of individual ω_0 values make the mean of this parameter unstable, making it necessary to obtain a robust estimate, which we choose in the form of the mode of the distribution. We estimated this quantity by computing a weighted mean of the five bins of the histogram (Fig. 5) located symmetrically about the interval containing the maximum value of the accumulated weight. To estimate the error of this quantity, we subdivided the entire sample into three nonoverlapping subsamples, estimated the mode for each subsample, and computed the dispersion s_1 of these estimates. We then estimated the dispersion of the mode of the entire distribution as $s_0 = s_1/\sqrt{3}$, since each subsample is a third the size of the entire sample. Our final estimate is $\omega_0 = +24.6 \pm 0.8$ km s^{-1} kpc^{-1}, close to the values of $\omega_0 = +26 \pm 2$ km s^{-1} kpc^{-1}
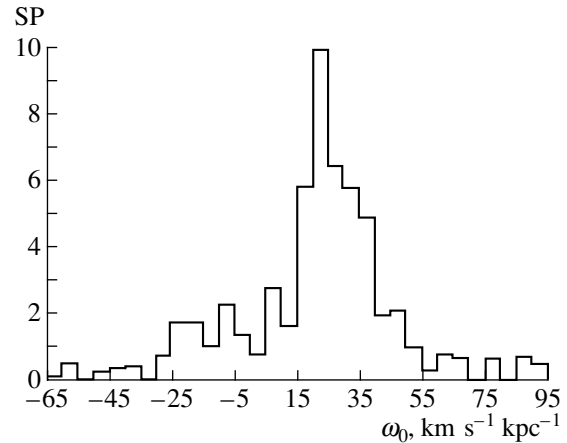
Fig. 5. Distribution of individual estimates of Galactic rotation frequency.

derived by Dambis *et al.* [10] and $\omega_0 = +27.2 \pm 0.9$ km s^{-1} kpc^{-1} obtained by Feast and Whitelock [11] based on the motions of classical Cepheids and different estimation techniques. We point out the somewhat smaller error of our estimate.

We found no significant correlation between our individual ω_0 estimates and the heliocentric distances or ages of the OCs, so that no corrections were needed in this connection.

To test the suitability of the proper motions of the most distant OCs for kinematic studies, we subdivided our sample into six subsamples containing OCs with different heliocentric distances. For each subsample, we computed the corresponding dispersions of the individual ω_0 estimates. The results are summarized in the table which gives (1) the mean heliocentric distance for the clusters of the given subsample, (2) the rms deviation from the mean ω_0 for the given subsample, and (3) the number of objects in the subsample.

The large dispersions of the individual estimates underline the unstable nature of the estimates of the mean—its strong dependence on the values in the

Table. Dependence of the dispersion of individual ω_0 estimates on heliocentric distance

$\bar{r}$, kpc	σ_x, km s^{-1} kpc^{-1}	N
0.3	74.81	17
0.8	40.87	26
1.3	43.42	37
1.7	29.87	28
2.4	11.61	28
4.3	13.55	15

wings of the distribution. Despite the small subsample sizes, the trend of the dispersion is immediately evident from the table: the dispersion of a single determination decreases with heliocentric distance and may increase only for the most distant OCs. The behavior of the dispersion with heliocentric distance mainly reflects the fact that the contribution of Galactic rotation to the proper motions increases with increasing heliocentric distance, while the contribution of the solar space motion and peculiar velocities decreases. Note, however, that this trend is not washed out by the proper-motion errors. We conclude that the accuracy of the mean OC proper motions based on the Tycho-2 catalog is high enough for information about the kinematics of the Galaxy to not be swamped by random errors, so that even the proper motions of the most distant OCs can be used for kinematic studies. Here, we naturally do not consider possible systematic errors of the catalog, although the effect of large systematic errors should increase with heliocentric distance and could have become appreciable in the data listed in the table. The Tycho-2 catalog is therefore unlikely to contain substantial systematic errors.

4. CONCLUSIONS

We have used data of the Tycho-2 catalog combined with photometric and kinematic criteria for cluster-member selection to compute the mean proper motions of 167 OCs with available radial-velocity measurements. The catalog of proper motions can be obtained by contacting the authors by e-mail at Alexhander.Loktin@usu.ru.

The new mean proper motions were used to derive the frequency of the Galactic rotation at the solar circle, which was found to be $\omega_0 = +24.6 \pm 0.8$ km s^{-1} kpc^{-1}. The linear velocity of rotation at the distance of R_0 from the Galactic-rotation axis is $V_{\rm rot}(R_0) = 201.7 \pm 9.9$ km/s. An analysis of the dependence of the dispersion of ω_0 estimates on heliocentric distance showed that, even for clusters with heliocentric distances $r > 3$ kpc, our proper motions contain enough useful information to be used in kinematic studies, indicating that determining the proper motions of very distant OCs is quite justified. Work on the determination of proper motions of OCs in the "Homogeneous catalog" [6] is ongoing.

REFERENCES

1. The Hipparcos and Tycho Catalogues, ESA-SP1200 (1997).
2. H. Baumgardt, C. Dettbarn, and R. Wielen, Astron. Astrophys., Suppl. Ser. **146**, 251 (2000).
3. W. S. Dias, J. R. D. Lepine, and B. S. Alessi, Astron. Astrophys. **376**, 441 (2001).
4. W. L. Sanders, Astron. Astrophys. **14**, 226 (1971).
5. A. V. Loktin and T. P. Gerasimenko, *Stellar Aggregates* [in Russian] (Sverdlovsk, 1980), p. 143.
6. A. V. Loktin, T. P. Gerasimenko, and L. K. Malysheva, Astron. Astrophys. Trans. **20**, 607 (2001).
7. A. V. Loktin and G. V. Beshenov, Pis'ma Astron. Zh. **27**, 450 (2001) [Astron. Lett. **27**, 386 (2001)].
8. A. V. Loktin, Astron. Tsirk., No. 1021, 1 (1978)
9. T. P. Gerasimenko, Pis'ma Astron. Zh. (2002) (in press) [Astron. Lett. (2002) (in press)].
10. A. K. Dambis, A. M. Mel'nik, and A. S. Rastorguev, Pis'ma Astron. Zh. **21**, 331 (1995) [Astron. Lett. **21**, 291 (1995)].
11. M. Feast and P. Whitelock, Mon. Not. R. Astron. Soc. **291**, 683 (1997).

Translated by A. Dambis

Radial Pulsations of Helium Stars and a Model for BX CIR

Yu. A. Fadeev and M. F. Novikova

Institute of Astronomy, Russian Academy of Sciences, Pyatnitskaya ul. 48, Moscow, 109017 Russia
Received February 18, 2002; in final form, June 26, 2002

Abstract—The results of hydrodynamical calculations of radially pulsating helium stars with masses $0.5M_\odot \leq M \leq 0.9M_\odot$, bolometric luminosities $600L_\odot \leq L \leq 5 \times 10^3 L_\odot$, and effective temperatures $1.5 \times 10^4 \text{ K} \leq T_{\text{eff}} \leq 3.5 \times 10^4 \text{ K}$ are presented. The pulsation instability of these stars is due to the effects of ionization of iron-group elements in layers with temperatures $T \sim 2 \times 10^5 \text{ K}$. The calculations were carried out using opacities for the relative mass abundances of hydrogen and heavy elements $X = 0$ and $Z = 0.01, 0.015$, and 0.02. Approximate formulas for the pulsation constant Q over the entire range of pulsation instability of the hot helium stars in terms of the mass M, radius R, effective temperature T_{eff}, and heavy-element abundance Z are derived. The instability of BX Cir to radial pulsations with the observed period $\Pi = 0.1066 \text{ d}$ occurs only for a mass $M \geq 0.55M_\odot$, effective temperature $T_{\text{eff}} \geq 23\,000 \text{ K}$, and heavy-element abundance $Z \geq 0.015$. The allowed mass of BX Cir is in the range $0.55M_\odot \leq M \leq 0.8M_\odot$, which corresponds to luminosities $800L_\odot \leq L \leq 1400L_\odot$ and mean radii $1.7R_\odot \lesssim R \lesssim 2.1R_\odot$.
© *2003 MAIK "Nauka/Interperiodica".*

1. INTRODUCTION

Stars with low hydrogen abundances ($X < 10^{-2}$) and effective temperatures in the range $1.5 \times 10^4 \text{ K} \lesssim T_{\text{eff}} \lesssim 4 \times 10^4 \text{ K}$ belong to a small group of hot helium stars. According to our current understanding, helium stars are in a short stage of evolution corresponding to the transition from the asymptotic giant branch to the white-dwarf stage. Their masses appear to be no greater than $1M_\odot$, with bolometric luminosities of $L \gtrsim 10^3 L_\odot$ [1]. The detection of photometric variability due to pulsation instability has great importance, since stellar-pulsation theory can then be applied to derive the mass and luminosity of the helium star, which are extremely important for verifying basic expectations of stellar-evolution theory. Until recently, V652 Her (BD + 13°3224) was the only hot helium star whose light and radial-velocity curves could be confidently interpreted in terms of radial pulsations. The observational estimates of the effective temperature averaged over a cycle $T_{\text{eff}} = 23\,500 \text{ K}$ [2] and the pulsation period $\Pi = 0.108 \text{ d}$ [3] could be used to determine the mass $M = 0.72M_\odot$ and luminosity $L = 1060L_\odot$ of this star based on stellar-pulsation theory [5].

A few years ago, radial pulsations were detected in the helium star LS S 3184 [6], later called BX Cir. The average effective temperature ($T_{\text{eff}} = 23\,300 \text{ K}$ [7]) and variability period ($\Pi = 0.1066 \text{ d}$ [8]) suggest that this star is similar to V652 Her. Unfortunately, the brightness of BX Cir is 2^m lower than that of V652 Her ($m_v \approx 12.5$). As a result, the determination

of its fundamental parameters is much more difficult. In particular, the only estimate of the gravitational acceleration at the stellar surface $\log g = 3.35$ has been obtained by Drilling *et al.* [7], by calculating the absorption profiles of neutral helium lines, and the relatively low reliability of data on helium-line broadening results in substantial uncertainty. Unfortunately, even if this value for the surface gravity is adopted, estimates of the mass of BX Cir are ambiguous, and vary from $M \approx 0.15M_\odot$ [8] to $M \approx 0.42M_\odot$ [9].

Therefore, estimates of the mass of BX Cir available thus far not only differ considerably from current estimates of the mass of the helium star V652 Her, but also turn out to be substantially lower than the masses allowed by stellar-evolution theory. We aim here to remove this discrepancy by determining the mass and luminosity of BX Cir on the basis of hydrodynamical calculations of the stellar pulsations.

In total, we computed over 300 hydrodynamical models. The method used to solve the equations of radiative gas dynamics for the case of radial stellar pulsations is described in detail in [4]. We analyzed the self-excited radial pulsations of helium stars using the approach described previously in [5, 10]. The calculations were carried out using the OP opacities [11] for mixtures s92.214, s92.215, and s92.216, which correspond to the relative mass abundances of hydrogen and heavy elements $X = 0$, $Z = 0.01, 0.015$, and 0.02. Given the high effective temperatures of the helium stars under consideration, we assumed that the role of convective heat transport through the stellar

envelope is negligible, so that the transport of energy is due only to radiation. Further, we assumed that the amplitude of the pulsations was negligible, i.e., $\partial r_0/\partial t = 0$, at the inner boundary $r_0 \approx 0.1R$ (where R is the radius of the outer boundary of the model). In addition, we assumed that the luminosity at the inner boundary did not vary with time: $\partial L_0/\partial t = 0$. Hydrodynamical calculations were carried out for time intervals covering $\sim 10^3$ to $\sim 10^4$ pulsation cycles, with the number of Lagrangian intervals being $150 \leq N \leq 250$. The equations of continuity and conservation of momentum were solved using explicit second-order difference schemes. Therefore, in accordance with the Courant stability criterion, up to $\sim 10^4$ integration steps should be used to compute one pulsation cycle. We considered primarily models in which the solution of the equations of radiative gas dynamics can be described in terms of oscillations for a limiting cycle. Due to the small temporal integration steps, the main hydrodynamical quantities in all Lagrangian nodes of the model at the limiting-cycle stage were repeatable to within $\sim 10^{-4}$. We analyzed the limiting-cycle hydrodynamical models by expanding solutions of the equations of radiative gas dynamics into Fourier series [12].

2. THE REGION OF PULSATION INSTABILITY

The region of partial ionization He$^+$ in helium stars of early spectral types is located near the photosphere. Due to their small extent, these layers do not appreciably affect the stability of the star to radial pulsations. This feature can be traced by considering the mechanical work $\Delta M_j \oint PdV$ produced by the jth Lagrangian layer with mass ΔM_j during a pulsation cycle. Here, P is the total pressure and $V = 1/\rho$ is the specific volume of the gas. An example of this dependence is presented in the upper part of Fig. 1, where the values of $\log T$ are plotted along the horizontal axis instead of the number of the Lagrangian interval $1 \leq j \leq 200$. For convenience in the graphical representation, we show the quantity $w_j = W^{-1}\Delta M_j \oint PdV$, where $W = \int_0^M \left|\oint PdV\right| dM_r$ is a normalization factor and $dM_r = 4\pi r^2 \rho dr$ is a mass element in the spherical layer with radius r. This plot demonstrates that the pulsation instability is due to the κ mechanism in the zone of ionization of iron-group elements in layers with temperatures $T \sim 2 \times 10^5$ K.

Since the oscillations are excited in a narrow zone located in the layers of fully ionized helium that represent a region of radiative suppression of the pulsation instability ($\oint PdV < 0$), the amplitude of the flux variations is largest near the maximum of
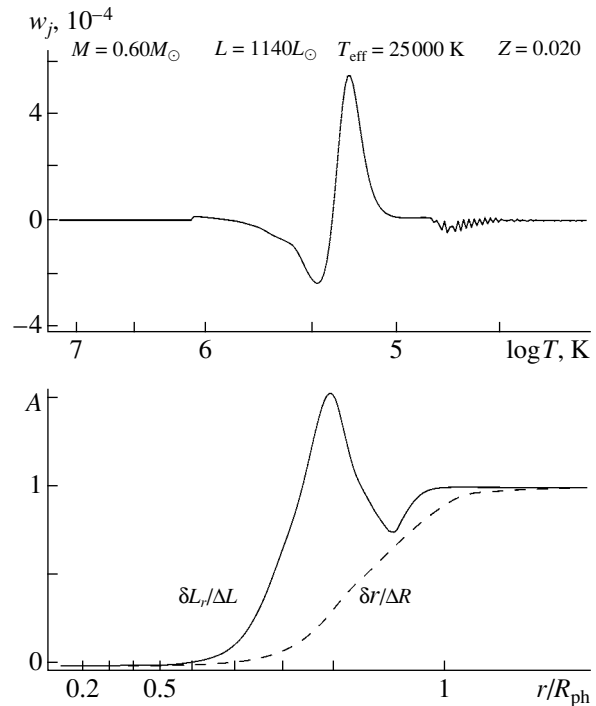

Fig. 1. The normalized work w_j produced by the jth Lagrangian interval during a pulsation cycle (top panel) and the amplitudes of variations in the luminosity $\delta L_r/\Delta L$ and radial displacement $\delta r/\Delta R$ (bottom panel, solid and dashed curves, respectively). The temperature scale $\log T$ and relative distance from the star's center r in units of the equilibrium radius of the photosphere R_{ph} are presented along the horizontal axis instead of the number of the Lagrangian interval $1 \leq j \leq 200$.
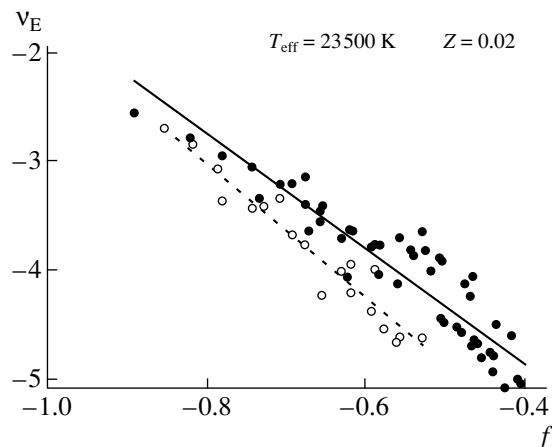

Fig. 2. The spectral index of the kinetic energy ν_E in the function $f = \log\left[(M/M_\odot)/(R/R_\odot)\right]$ for models with effective temperature $T_{eff} = 23\,500$ K and heavy-element abundances $Z = 0.02$ (filled circles) and $Z = 0.01$ (hollow circles).

$\Delta M_j \oint PdV$ and decreases toward the surface. This is an important characteristic of radially pulsating

hot helium stars that distinguishes them from other pulsating variables. This is illustrated in the lower part of Fig. 1, which presents plots of the amplitudes of the variations in luminosity $\delta L_r / \Delta L$ and radial displacement $\delta r / \Delta R$ normalized to the corresponding values at the surface. The average distance from the center of the star r in units of the equilibrium radius of the photosphere $R_{\rm ph}$ is shown along the horizontal axis. The outer boundary of the model corresponds to $r/R_{\rm ph} = 1.02$. The ratio of the luminosity-variation amplitudes in the region of excitation of the instability δL_* and at the outer boundary ΔL increases with the luminosity and is $1.1 \lesssim \delta L_*/\Delta L \lesssim 3$ for $10^3 L_\odot \lesssim L \lesssim 3 \times 10^3 L_\odot$.

The nonmonotonic variation in δL_r with radius results in certain characteristic features that can be detected in observations. The first is small amplitudes (a few tenths of a magnitude) for the variations in bolometric luminosity in the presence of considerable radial-velocity variations ($\Delta V_{\rm r} \lesssim 100$ km/s). Second, since the zone of partial ionization of hydrogen is absent, the maximum luminosity occurs before the maximum speed of expansion of the outer layers by amounts from $\delta\phi \approx 0.1\Pi$ for $L \approx 10^3 L_\odot$ to $\delta\phi \approx 0.25\Pi$ for $L \approx 3 \times 10^3 L_\odot$. We emphasize that, in classical pulsating variables possessing a zone of partial ionization of hydrogen near the photosphere, the maximum brightness coincides with the maximum expansion velocity to within a few hundredths of the period.

Radial pulsations of hot helium stars are associated with instability of the fundamental mode, since the zone of excitation of the oscillations is located deeper than the outer nodes of the overtones. Moreover, the variations in the phase of the radial displacement as a function of distance from the center are quite small, and are only a few hundredths of a radian in $\approx 98\%$ of the envelope radius. This implies that deviations from adiabaticity of the pulsations are small. In general, such deviations in the layer with radius r are characterized by the ratio of the thermal and dynamical time scales [13]:

$$\alpha = \frac{\tau_{\rm th}}{\tau_{\rm dyn}} = \frac{4\pi r^3 \rho C_{\rm p} T/L_r}{(R^3/GM)^{1/2}}, \qquad (1)$$

where $C_{\rm p}$ is the specific heat capacity at constant pressure. This ratio is $\alpha \gtrsim 10^2$ in the zone of excitation of the pulsation instability in hot helium stars. The small deviation from adiabatic behavior in hot helium stars is their main difference from later-type helium stars. This is due to the fact that the source of the pulsation instability at effective temperatures $T_{\rm eff} \lesssim 1.2 \times 10^4$ K is layers of partial ionization of He$^+$ located near the photosphere, above the outer nodes

of overtones of order $3 \le k \le 6$. Therefore, the radial pulsations in colder helium stars are represented by overtones. Due to the considerable deviations from adiabaticity in the layers of excitation of the instability ($\alpha \sim 1$), the phase of the displacement varies continuously along the radius, so that the radial pulsations cannot be described by a standing wave [14, 15].

The spectrum of the kinetic energy of the radial pulsations is described by the power law $E_{{\rm K}k} = E_{{\rm K}1} k^{\nu_{\rm E}}$, where $E_{{\rm K}k}$ is the kinetic energy of the Fourier harmonic of order $k \ge 1$ and $\nu_{\rm E} < 0$ is the spectral index [16]. When the luminosity of the helium stars increases, the amplitude of the pulsations increases, and the kinetic-energy spectrum becomes gently sloping. This behavior suggests a redistribution of the pulsation energy among higher-order Fourier harmonics. This is illustrated in Fig. 2, which presents the spectral index of the kinetic energy of Fourier harmonics $\nu_{\rm E}$ as a function of the quantity $f = \log\left[(M/M_\odot)/(R/R_\odot)\right]$ for models with masses $0.5 M_\odot \le M \le 0.8 M_\odot$ and bolometric luminosities $800 L_\odot \le L \le 5000 L_\odot$ with $T_{\rm eff} = 23\,500$ K and $Z = 0.01$ and 0.02. As in the case of Cepheid variables, the contribution of Fourier harmonics of order $k > 1$ to the kinetic energy of the pulsating envelope increases with increasing luminosity or decreasing effective temperature of the star. As a result, the luminosity and radial-velocity curves become more asymmetric.

The ability of the star to experience radial pulsations via the κ mechanism depends both on the amplitude of the displacement in the layers of partial ionization and on the relative mass of these layers. For hot helium stars with masses $M = 0.6 M_\odot$ and a heavy-element abundance $Z = 0.02$, the work done by the layers amplifying the radial oscillations exceeds the magnitude of the negative work done by the layers suppressing the oscillations if $L \gtrsim 600 L_\odot$. When the luminosity increases, the interval of effective temperatures in which the star is unstable to radial oscillations expands to both lower and higher values of $T_{\rm eff}$. For example, the region of radial pulsations is limited to effective temperatures $21\,400$ K $\lesssim T_{\rm eff} \lesssim 29\,000$ K when the luminosity is $L = 10^3 L_\odot$, while the corresponding interval for $L = 2 \times 10^3 L_\odot$ is $18\,000$ K $\lesssim T_{\rm eff} \lesssim 33\,000$ K. The boundary of the region of pulsation instability can be defined in the Hertzsprung–Russell diagram as the line of zero increment of the instability, $\eta = \Pi d \ln E_{\rm K}/dt = 0$, where $E_{\rm K}$ is the kinetic energy of the pulsating envelope. We defined the position of the boundary $\eta = 0$ by interpolating in $\log L$ between two models with equal effective temperatures, one showing attenuation of the oscillations ($\eta < 0$) and the other showing amplification of the instability ($\eta > 0$) preceding the limiting-cycle stage.

The boundaries of the region of instability for helium stars with mass $M = 0.6M_{\odot}$ and heavy-element abundances $Z = 0.02$ and 0.01 are drawn in Fig. 3. Contours corresponding to radial pulsations with periods $\Pi = 0.1$, 0.2, and 0.5 d are presented in the same figure. As follows from our calculations, the shortest radial-pulsation period for hot helium stars is $\Pi \approx 0.05$ d. This period increases with increasing luminosity and decreasing effective temperature, but the radial pulsations become quasiregular at $L > 3000L_{\odot}$ due to nonlinear effects, so that exactly periodic radial pulsations are possible only for periods shorter than 2 d.

The locations of the solid and dashed curves in Fig. 3 representing the boundaries of the pulsation instability for $Z = 0.02$ and $Z = 0.01$ illustrate the sensitivity of the boundaries to the heavy-element abundance. These boundaries are also shifted (but by a much smaller amount) when the stellar mass changes. In particular, the region of pulsation instability shrinks with increasing stellar mass, while the threshold luminosity corresponding to the lower boundary of the instability region at $Z = 0.02$ increases from $L \approx 600L_{\odot}$ for $M = 0.55M_{\odot}$ to $L \approx 1200L_{\odot}$ for $M = 0.8M_{\odot}$.

The region of pulsation instability of the hot helium stars can also be estimated by considering the amplitude of the pulsations of the outer layers of the star as a function of the effective temperature at fixed values of the mass M and luminosity L. Figure 4 presents the corresponding dependences of the amplitude of the velocity of the outer layers ΔU for helium stars with mass $M = 0.6M_{\odot}$, heavy-element abundance $Z = 0.02$, and bolometric luminosities $L = 10^3$, 2×10^3, and $3 \times 10^3 L_{\odot}$. For ease of comparison with the Hertzsprung–Russell diagram, the effective temperatures T_{eff} decrease along the horizontal axis from left to right.

The increment of the pulsation instability at a fixed luminosity increases with the effective temperature, reaches a maximum at $T_{\text{eff}} \approx 27\,000$ K, and then decreases with further increase in T_{eff}. Figure 4 shows that this effective temperature corresponds to the largest amplitude of the radial pulsations. The instability is also amplified with increases in the luminosity of the star, and the pulsation motions are no longer exactly periodic at $L > 3 \times 10^3 L_{\odot}$ due to nonlinear effects. Further, at luminosities $L \gtrsim 10^4 L_{\odot}$, the velocity of the outer layers of the stellar atmosphere approaches the local escape velocity, so that mass loss will take place. Our method for solving the gas-dynamics equations is based on a Lagrangian description of the gas motion, and cannot be directly applied to describe the effects of mass loss. Therefore, we shall not discuss nonlinear hydrodynamical models involving outflows of material from the star.
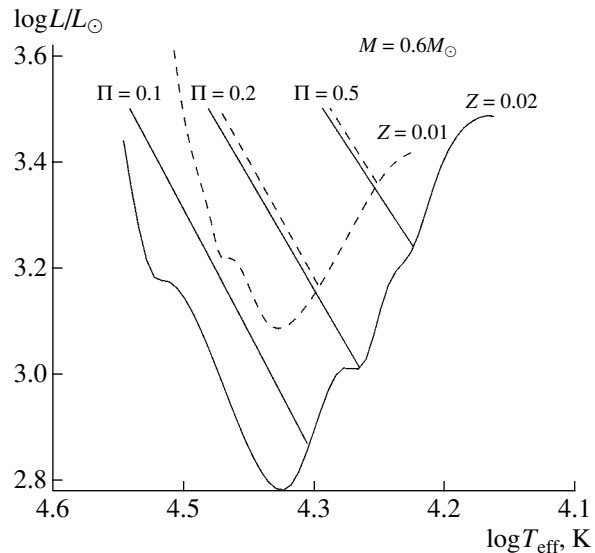
Fig. 3. Boundaries of the pulsation instability and lines of constant period of the fundamental mode in the Hertzsprung–Russell diagram for hot helium stars with mass $M = 0.6M_{\odot}$ and heavy-element abundances $Z = 0.02$ (solid curves) and $Z = 0.01$ (dashed curves).

3. PULSATION CONSTANTS

Analysis of the hydrodynamical models enables us to impose strong constraints on the intervals of admissible mass M and bolometric luminosity L of the pulsating star if we have observational values of the pulsation period Π and effective temperature T_{eff} averaged over a cycle. For this, we must determine the pulsation constant as a function of the mass of the star, its mean radius, and its heavy-element abundance: $Q = Q(M, R, Z)$. Substituting approximate expressions for Q obtained by calculating the stellar pulsations into the dependence relating the period and mean density,

$$\Pi = Q\,(M, R, Z)\,(R/R_{\odot})^{3/2}\,(M/M_{\odot})^{-1/2}, \quad (2)$$

transforms this expression into a nonlinear algebraic relation between the mass and bolometric luminosity of the star. Equation (2) can be solved for M if observational estimates of the mean radius are available (obtained, for example, using the Baade–Wesselink method).

We derived approximations of the pulsation constant for helium stars with masses $0.5M_{\odot} \leq M \leq 0.8M_{\odot}$, bolometric luminosities $650L_{\odot} \leq L \leq 3000L_{\odot}$, effective temperatures $20\,000$ K $\leq T_{\text{eff}} \leq 30\,000$ K, and heavy-element abundances $Z = 0.01$, 0.015, and 0.02. To avoid a loss in accuracy in the process of approximating the function of several variables, we searched for an approximation formula of independent variables $f = \log\left[(M/M_{\odot})\,(R/R_{\odot})\right]$ and $M/M_{\odot}$,
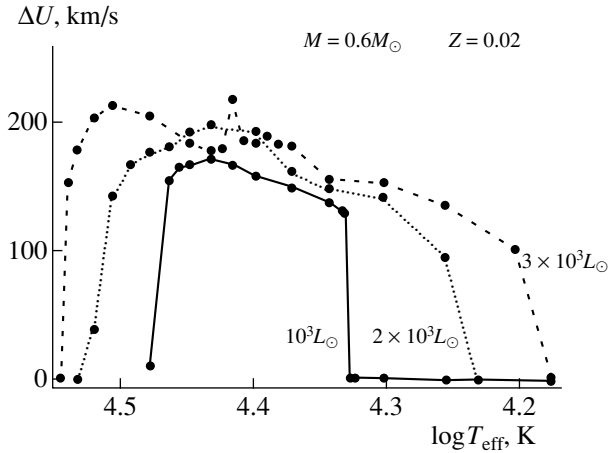
Fig. 4. Amplitude of the velocity of the pulsation motions in the outer layers of hot helium stars as a function of the effective temperature for $M = 0.6M_\odot$ and $Z = 0.02$. The individual models are presented by the filled circles and joined by the solid, dotted, and dashed lines for $L = 10^3$, 2×10^3, and $3 \times 10^3 L_\odot$, respectively.
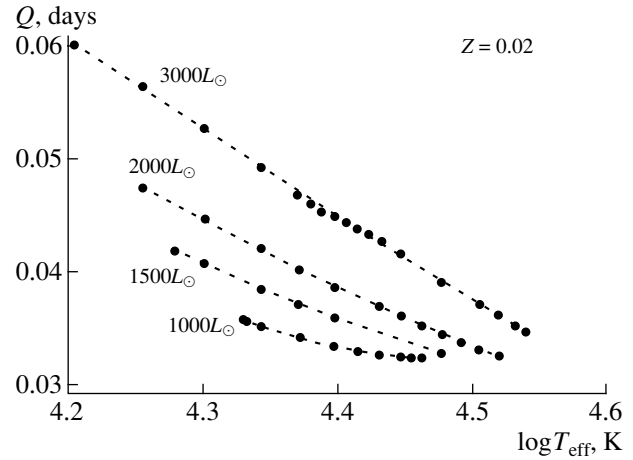

Fig. 5. Pulsation constants (filled circles) and their approximation by the algebraic polynomial (4) (dashed curves).

with $T_{\rm eff}$ and Z treated as parameters. The approximate expression of the pulsation constant for each pair of $T_{\rm eff}$ and Z values was taken in the form

$$Q(M, f) = a_0 + a_1 f + a_2 f^2 + b_1 \left(M/M_\odot\right), \quad (3)$$

where the coefficients a_0, a_1, a_2, and b_1 were determined by the least-squares method using the results of computing several dozen hydrodynamical models. The values of the corresponding coefficients are presented in Table 1. The rms error of (3) for each pair of $T_{\rm eff}$ and Z values within the above intervals of M and L is below 1%.

To take into account the dependence of the pulsation constant on the effective temperature at fixed f and $M/M_\odot$, it is sufficient to use a second-order

Table 1. Coefficients of approximation formula (3)

Z	$T_{\rm eff}$	a_0	a_1	a_2	b_1
0.01	20000	0.0790	0.182	0.155	0.0147
0.02	20000	0.0702	0.163	0.152	0.0140
0.01	23500	0.0531	0.113	0.127	0.00913
0.015	23500	0.0480	0.0890	0.110	0.00460
0.02	23500	0.0328	0.0375	0.0684	0.00511
0.01	25000	0.0553	0.123	0.140	0.00902
0.02	25000	0.0506	0.0992	0.131	0.00134
0.02	30000	0.0470	0.121	0.184	0.00897

algebraic polynomial:

$$Q = c_0 + c_1 \log T_{\rm eff} + c_2 \left(\log T_{\rm eff}\right)^2. \quad (4)$$

The results of this approximation are illustrated in Fig. 5. Therefore, using (3) and (4) and the polynomial coefficients presented in Table 1, the pulsation constant can be found for almost the entire instability region for hot helium stars, with relative errors below 1%.

4. THE MODEL FOR BX CIR

Using the blackbody radiation law, the dependence between the period and mean density (2) can be transformed to the form

$$L = 4\pi\sigma R_\odot^2 T_{\rm eff}^4 \left(\Pi/Q\right)^{4/3} \left(M/M_\odot\right)^{2/3}, \quad (5)$$

where σ is the Stefan–Boltzmann constant. Formulas (3) and (5) enable us to express the bolometric luminosity as a function of the stellar mass for specified values of pulsation period Π, effective temperature $T_{\rm eff}$, and heavy-element abundance Z. Unfortunately, because of the nonlinear character of the initial relations, the resulting dependence between the mass and luminosity cannot be presented in analytical form. Therefore, we determined this dependence by iteratively solving (3) and (5) for L for a given set of masses M. We found that, when the heavy-element abundance is $Z < 0.015$, the line of constant period $\Pi = 0.1066$ d lies beyond the pulsation-instability region for all values of $T_{\rm eff}$. Therefore, to explain the observed variability of BX Cir, we must assume that the relative mass abundance of heavy elements in this star is $Z \geq 0.015$.

Two dependences between the mass and luminosity of a helium star for a radial-pulsation period
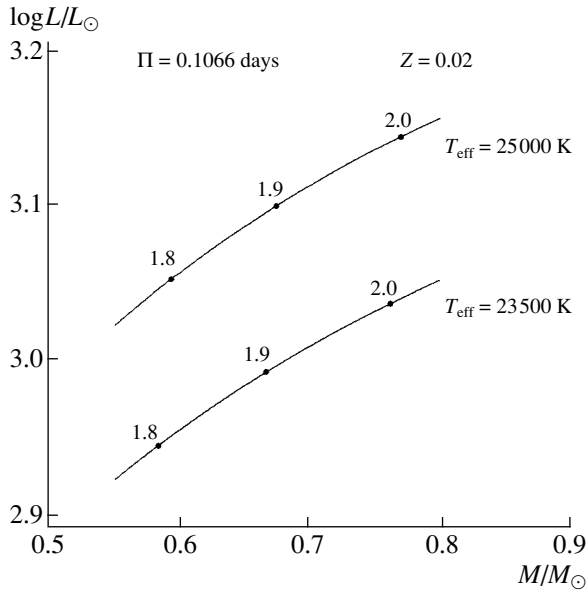
Fig. 6. Mass−luminosity dependence for helium stars pulsating with the period $\Pi = 0.1066$ d for $Z = 0.02$. The numbers near the curves denote the stellar radii $R/R_\odot$ averaged over a cycle.
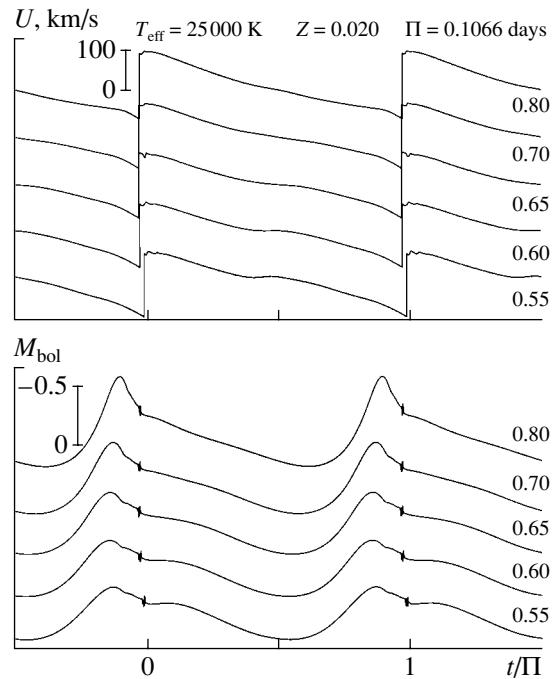

Fig. 7. Curves of the velocity of the outer boundary (top panel) and bolometric luminosity (bottom panel) for the hydrodynamical models of BX Cir with $T_{\text{eff}} = 25\,000$ K and $Z = 0.02$. The numbers near the curves denote the values of $M/M_\odot$.

$\Pi = 0.1066$ d and $Z = 0.02$ are presented in Fig. 6 for $T_{\text{eff}} = 23\,500$ K and $T_{\text{eff}} = 25\,000$ K. If the radial pulsation period is fixed, the luminosity should increase with increasing effective temperature and mass. Therefore, in order for the radially pulsating helium star BX Cir to be in the pulsation-instability region, its mass and effective temperature must satisfy the conditions $M \geq 0.55 M_\odot$ and $T_{\text{eff}} \gtrsim 23\,000$ K. Firmer conclusions about the mass and luminosity of BX Cir can be derived if observational estimates of its mean radius (obtained, for example, using the Baade−Wesselink method) are available. Accordingly, the corresponding mean radii of the star (in units of the solar radius) are given in the mass−velocity dependences presented in Fig. 6.

Constraints can also be placed on the intervals of allowed mass and luminosity of BX Cir by comparing the observed and theoretical luminosity and radial-velocity curves. The effectiveness of this approach was demonstrated by Fadeev and Lynas−Gray [5] for the case of V652 Her. We calculated several sequences of hydrodynamical models with fundamental-mode periods $\Pi = 0.1066$ d. The basic characteristics of these models are summarized in Table 2, and the corresponding curves for the velocity of the outer boundary and the absolute bolometric luminosity are presented in Fig. 7. The small variations in U near the maximum expansion speed and simultaneous luminosity oscillations are due to the limited spatial resolution of the hydrodynamical models.

A common feature in the luminosity and radial-velocity curves is a delay of the maximum velocity with respect to the maximum luminosity by amounts from $\delta\varphi \approx 0.13$ when $M = 0.55 M_\odot$ to $\delta\varphi \approx 0.08$ when $M = 0.8 M_\odot$. This is the main difference of the hot helium stars from classical pulsating variables (such as Cepheids and RR Lyrae stars). This delay is due to the deeper location of the pulsation-

Table 2. Hydrodynamical models of the radially pulsating helium stars for the fundamental period $\Pi = 0.1066$ d

Z	T_{eff}, K	$M/M_\odot$	$L/L_\odot$	Q, d	ΔU, km/s	ΔM_{bol}
0.02	23500	0.55	835	0.03406	147	0.49
0.02	23500	0.6	900	0.03372	149	0.53
0.02	23500	0.65	957	0.03342	154	0.59
0.02	23500	0.7	1015	0.03319	154	0.65
0.02	23500	0.8	1125	0.03288	159	0.81
0.02	25000	0.55	1060	0.03439	162	0.45
0.02	25000	0.6	1140	0.03400	161	0.48
0.02	25000	0.65	1220	0.03366	161	0.53
0.02	25000	0.7	1296	0.03338	162	0.59

excitation region in the stellar envelope compared to the case of classical pulsating variables. Another interesting feature is the presence of a bulge in the decreasing branches of the luminosity and velocity curves at stellar masses $M < 0.7 M_{\odot}$. This feature can also be used to determine the mass of BX Cir if more accurate luminosity and radial-velocity curves become available.

5. CONCLUSION

The small number of early-type radially pulsating helium stars known up to the present time is apparently the result not only of the short duration of the corresponding evolutionary stage, but also of observational selection effects. In fact, as was shown in Section 2, the most important photometric feature of these stars is the small amplitude of their luminosity variations (below a few tenths of a magnitude), due to the localization of the instability-excitation zone deeper than the layers of fully ionized helium that suppress this instability. In addition, since the instability-excitation zone is localized inside the region of radiative damping of the pulsations, the luminosity maximum occurs well before the expansion-velocity maximum (by $0.1 \leq \delta\phi \leq 0.25$). This feature, along with an early spectral type and a considerable radial-velocity amplitude in the presence of small variations in the observed luminosity, can be used as criteria that a variable is a helium star. The characteristic periods of the luminosity variations are in the range $0.05\,\mathrm{d} \lesssim \Pi \lesssim 2\,$ d, and the luminosity variations with periods over two days are no longer exactly periodic due to nonlinear effects.

As was shown in Section 4, the radial pulsations of BX Cir are possible if the mass and luminosity of the star are $M \geq 0.55 M_{\odot}$ and $L \geq 850 L_{\odot}$. If the effective temperatures are in the range $23\,000\,\mathrm{K} \leq T_{\mathrm{eff}} \leq 25\,000$ K, this corresponds to mean radii $1.7 R_{\odot} \lesssim R \lesssim 2.1 R_{\odot}$. Therefore, there is a clear inconsistency in the estimates of the mass $M = 0.42 M_{\odot}$ and mean radius $R = 2.3 R_{\odot}$ given by Woolf and Jeffery [9],

since the mass of a star pulsating with a period of 0.1066 d and a radius of $R = 2.3 R_{\odot}$ should be $M \approx 1.1 M_{\odot}$, while the line of constant period $\Pi = 0.1066$ d for $M \approx 0.4 M_{\odot}$ is beyond the region of pulsation instability. New photometric and spectral observations of BX Cir are needed to resolve this discrepancy.

Additional information on the hydrodynamical models of helium stars can be obtained from the authors.

REFERENCES

1. I. Iben, A. V. Tutukov, and L. R. Yungelson, Astrophys. J. **456**, 750 (1996).
2. A. E. Lynas-Gray, D. Schönberner, P. W. Hill, and U. Heber, Mon. Not. R. Astron. Soc. **209**, 387 (1984).
3. A. U. Landolt, Astrophys. J. **196**, 789 (1975).
4. Yu. A. Fadeev, Nauchn. Inf. Astron. Soveta Akad. Nauk SSSR **52**, 3 (1983).
5. Yu. A. Fadeyev and A. E. Lynas-Gray, Mon. Not. R. Astron. Soc. **280**, 427 (1996).
6. D. Kilkenny and C. Koen, Mon. Not. R. Astron. Soc. **275**, 327 (1995).
7. J. S. Drilling, C. S. Jeffery, and U. Heber, Astron. Astrophys. **329**, 1019 (1998).
8. D. Kilkenny, C. Koen, C. S. Jeffery, *et al.*, Mon. Not. R. Astron. Soc. **310**, 1119 (1999).
9. V. M. Woolf and C. S. Jeffery, Astron. Astrophys. **358**, 1001 (2000).
10. Yu. A. Fadeyev, Astron. Soc. Pac. Conf. Ser. **96**, 375 (1996).
11. M. J. Seaton, Y. Yan, D. Mihalas, and A. K. Pradhan, Mon. Not. R. Astron. Soc. **266**, 805 (1994).
12. Yu. A. Fadeev, Astron. Zh. **74**, 720 (1997) [Astron. Rep. **41**, 639 (1997)].
13. H. Saio, J. C. Wheeler, and J. P. Cox, Astrophys. J. **281**, 318 (1984).
14. Yu. A. Fadeyev, Mon. Not. R. Astron. Soc. **244**, 225 (1990).
15. Yu. A. Fadeyev, Mon. Not. R. Astron. Soc. **262**, 119 (1993).
16. Yu. A. Fadeyev and H. Muthsam, Astron. Astrophys. **260**, 195 (1992).

Translated by Yu. Dumin

Observations of Cyanoacetylene Sources

A. V. Alakoz, S. V. Kalenskiĭ, M. A. Voronkov, and V. I. Slysh

Astro Space Center, Lebedev Physical Institute, Russian Academy of Sciences, Profsoyuznaya ul. 84/32, Moscow, 117997 Russia
Received March 18, 2002; in final form, June 26, 2002

Abstract—Thirty-four Galactic star-forming regions have been observed in the $J = 4-3$ line of cyanoacetylene (HC_3N) at 36.4 GHz. Emission was detected toward 17 sources. The HC_3N column density was determined in the detected sources, and in eight of them (NGC 2264, L379, W51E1/E2, DR 21West, DR 21(OH), DR 21, S140, and Cep A), the relative cyanoacetylene abundance was estimated. The HC_3N abundance in these objects is about $1-70 \times 10^{-10}$. © *2003 MAIK "Nauka/Interperiodica".*

1. INTRODUCTION

Cyanoacetylene in the interstellar medium was first detected in 1970 by Turner [1], who recorded the emission in the $J = 1-0$ line toward the giant molecular cloud Sgr B2. Since then, HC_3N has been frequently observed in molecular clouds [2–4]. The cyanoacetylene column densities in warm and cool clouds are on the order of 10^{13} cm^{-2}, and its abundance is about $10^{-9}-10^{-10}$. Blake [5] derived a column density of 1.8×10^{14} cm^{-2} and abundance of 4×10^{-9} for the high-velocity gas (the "plateau" in OMC-1). In addition, HC_3N emission has been observed in the envelopes of C giant stars [6].

The cyanoacetylene molecule has a number of properties making it convenient for deriving the parameters of molecular clouds. First, because of its large dipole moment (3.72 D), densities no lower than 10^4 cm^{-3} are required for the collisional excitation of even the lowest levels. Moreover, cyanoacetylene is a heavy linear molecule with a small rotational constant ($B_0 \sim 4.50$ GHz), so that the lines are spaced more closely than in the spectra of lighter molecules, such as HCN, and a greater number of HC_3N lines fall into the radio range. The HC_3N column densities in molecular clouds are sufficiently high for the lines to be detectable but at the same time too low for them to be optically thick [7–10].

These properties make cyanoacetylene observations an indispensable tool in analyses of molecular clouds. In spite of this, there have been no systematic cyanoacetyline surveys of regions of massive-star formation. We accordingly have observed a number of sources in the 4–3 HC_3N line, most of them warm clouds associated with regions of formation of massive stars. In this article, we report the results of this survey.

2. OBSERVATIONS AND RESULTS

The observations were carried out in October 1997 and March 1998 on the 22-m radio telescope of the Pushchino Radio Astronomy Observatory. The line frequency, 36392.332 MHz, was taken from the database of Lovas (http://physics.nist.gov/PhysRef-Data/micro/html/Contents.html). The observations were carried out in a beam-switching mode with a beam separation of 29'. The beamwidth was 2', and the main beam efficiency 0.36. The system noise temperature was about 250–300 K. The spectrum analyzer used was a 32-channel spectrometer with a resolution of 125 kHz (~ 1 km/s). The bandwidth of the spectral channels far exceeded the linewidths in dark clouds; therefore, the line intensity we recorded for TMC-1 is considerably inferior to that given in [4]. Seventeen sources were detected in the observations. Their spectra are presented in the figure, and the parameters of the detected lines fitted with Gaussians are given in Table 1.

## 3. ANALYSIS OF THE OBSERVATIONAL DATA

We approximated the spectra of the detected sources with Gaussian profiles. We did not take into account hyperfine splitting because of the insufficient spectral resolution and considerable linewidths in most of the sources. The results are given in Table 1.

The resulting antenna temperatures averaged over the main beam (T_{mb}) are low: as a rule, lower than 0.5 K. In view of probable dilution (see below), we find that the brightness temperatures of the sources do not exceed 2–4 K. Such low temperatures are consistent with earlier findings that the HC_3N lines are optically thin. Assuming thermalized level populations, we can

Table 1. Results of the HC$_3$N observations

Source	RA (1950)	DEC (1950)	V_{LSR}, km/s	T_{mb}, K	ΔV, km/s
00338+6312	00 33 53.0	63 12 32	−17.9	<0.31	
00494+5617	00 49 29.0	56 17 36	−31.3	<0.38	
03035+5819	03 03 33.0	58 19 21	−21.6	<0.30	
B1	03 30 06.0	30 57 36	7.4(0.4)	0.24(0.61)	2.8(0.8)
B5	03 44 29.0	32 44 33	10.3(0.2)	0.35(0.28)	1.6(0.5)
TMC-1	04 38 38.0	25 35 00	6.8(0.1)	1.97(0.13)	1.9(0.1)
05274+3345	05 27 28.0	33 45 37	−3.1	<0.25	
ORI-KL	05 32 47.0	−05 24 23	11.0(0.2)	1.06(0.17)	2.5(0.5)
OMC-2	05 32 59.9	−05 11 29	10.5	<0.30	
S231	05 35 51.3	35 44 16	−16.5	<0.25	
S235	05 37 31.8	35 40 18	−17.5	<0.21	
NGC 2024	05 39 11.4	−01 55 59	10.6(0.3)	0.35(0.08)	2.3(0.6)
NGC 2071	05 44 31.3	00 20 48	14.5	<0.26	
S252A	06 05 36.5	20 39 34	4.5	<0.33	
S252	06 05 53.7	21 39 09	9.5	<0.25	
S255	06 10 01.0	18 00 44	10.5	<0.35	
S269	06 11 46.5	13 50 39	16.5	<0.21	
NGC 2264	06 38 24.0	09 32 00	8.8(0.2)	0.49(0.06)	2.9(0.4)
NGC 2264N	06 38 23.0	09 38 30	6.0(0.4)	0.24(0.06)	2.8(0.9)
G1.6-0.025	17 46 12.0	−27 33 15	51.4(2.1)	0.85(0.19)	18.5(5.3)
L379	18 26 32.9	−15 17 51	18.8(0.2)	0.49(0.08)	2.7(0.6)
G30.8-0.1	18 45 11.0	−01 57 57	95.6(0.4)	<0.35	
W51E1/E2	19 21 26.2	14 24 43	55.6(0.3)	0.38(0.07)	3.6(0.7)
19410+2336	19 41 04.0	23 36 42	22.6(0.3)	0.17(0.04)	2.7(0.7)
Onsala 1	20 08 09.9	31 22 42	11.5	<0.36	
20188+3928	20 18 51.0	39 28 18	1.3(0.4)	0.28(0.07)	3.0(0.9)
Onsala 2	20 19 50.0	37 16 30	−2.5	<0.42	
W75N	20 36 50.4	42 27 01	8.5	<0.21	
DR 21 West	20 37 07.6	42 08 46	−2.6(0.2)	0.72(0.13)	2.2(0.5)
DR 21 OH	20 37 13.8	42 12 13	−1.4(0.7)	0.75(0.21)	4.9(1.6)
DR 21	20 37 14.3	42 09 14	−2.6(0.3)	0.65(0.15)	2.8(0.8)
S140	22 17 41.2	63 03 43	−6.8(0.2)	0.56(0.07)	2.4(0.4)
Cep A	22 54 21.0	61 45 30	−4.4(0.2)	0.32(0.06)	2.8(0.6)
NGC 7538	22 11 36.6	61 11 50	−57.5	<0.28	

Note: Upper limits for the antenna temperatures of the undetected sources are given at the 3σ level.
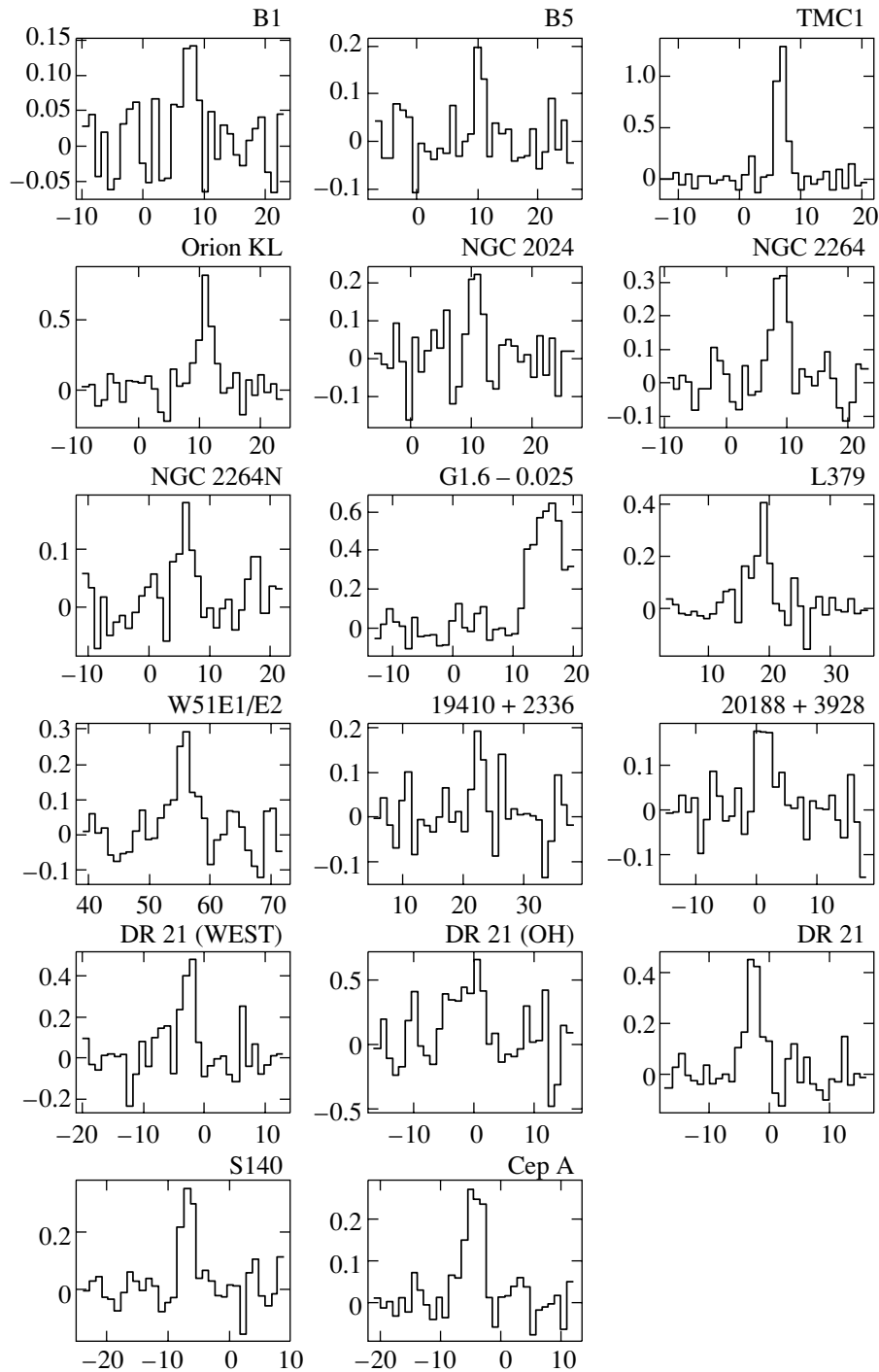
Spectra of the cyanoacetylene sources. The horizontal axis is the LSR velocity of the 4−3 line in km/s, and the vertical axis is the main-beam-averaged antenna temperature in Kelvins.

estimate the cyanoacetylene column density using the simple formula

$$N_{\mathrm{mol}} = \frac{3k \times 10^5 \int T_{\mathrm{br}} dV \times Q_{\mathrm{rot}} \exp(E_{\mathrm{u}}/kT)}{8\pi^3 \mu^2 \nu S}, \quad (1)$$

where E_{u} is the upper-level energy, $Q_{\mathrm{rot}} = kT/hB_0$ is the rotational statistical sum, μ is the electric dipole moment, ν is the frequency, S is the line strength, $\int T_{\mathrm{br}} dV$ is the integrated line intensity [K km/s], and T is the gas temperature. Including numerical constants yields

$$N_{\mathrm{mol}} = 3.79 \times 10^{11} T \int T_{\mathrm{br}} dV \exp(4.37/T). \quad (2)$$

Table 2. HC_3N column densities and abundances

Source	N_{HC_3N}, 10^{13}	HC$_3$N abundance		T_{kin}, K
		extended source	pointlike source	
B1	0.46			12 [17]
B5	0.45			15 [18]
NGC 2024	1.6			45 [19]
NGC 2264	1.4	3.7×10^{-10}	4.6×10^{-9}	20 [11]
NGC 2264N	0.72			22 [13]
G1.6-0.025	35			50 [15]
L379	1.5	2.5×10^{-10} [h]	3.2×10^{-9} [h]	24 [14]
W51E1E2	2.9	8.8×10^{-11}	1.1×10^{-9}	49 [11]
19410+2336	0.81			40 [11]
20188+3928	0.77			18 [16]
DR 21WEST	2.0	4.4×10^{-10}	5.5×10^{-9}	26 [11]
DR 21OH	6.5	5.4×10^{-10}	6.7×10^{-9}	39 [11]
DR 21	2.0	2.6×10^{-10}	3.3×10^{-9}	22 [20]
S140	1.7	2.7×10^{-10}	3.3×10^{-9}	26 [11]
Cep A	1.4	1.7×10^{-10}	2.1×10^{-9}	33 [11]

We took the kinetic temperatures for these calculations from observations of methyl acetylene, ammonia, and other molecules [11−16]. In addition, using the H_2 column densities obtained from ^{13}CO observations at 110 GHz [11], we derived the cyanoacetylene abundances in seven sources (NGC 2264, W51E1/E2, DR 21 (West), DR 21 (OH), DR 21, S140, and Cep A). The cyanoacetylene abundance of L379 was determined using the H_2 column density and temperature from [14]. The results are given in Table 2. Our HC_3N observations were carried out with a 2′ beam, whereas the beam for the ^{13}CO observations was considerably narrower (34″). Therefore, accurate calculation of the abundances requires that we know the source sizes. As these sizes are unknown, Table 2 lists two extreme cases: a pointlike source and a source larger than 2′ (an "extended source"). As we can see from Table 2, the extended-source column densities are in the range $0.4−6.5 \times 10^{13}$, consistent with the data of other authors (see Introduction). The HC_3N abundances are $(1−6) \times 10^{-10}$ for the extended case and $(1−7) \times 10^{-9}$ for the pointlike case.

L.E. Pirogov (private communication) has mapped some regions of massive-star formation in the 10−9 and 12−11 HC_3N lines and found that the source sizes are, as a rule, in the interval 15″−75″.

Therefore, we suppose that the HC_3N abundances calculated for the pointlike sources are closer to the abundances in the real objects.

Various authors [11, 21−23] have modeled the chemical evolution of molecular clouds; in particular, they have studied the time dependence of the HC_3N abundance. The maximum cyanoacetylene abundances are precisely of the order of $10^{-8}−10^{-10}$. These abundances are achieved at cloud ages from 10^5 to 10^7 years, and fall by several orders of magnitude outside this age interval. Thus, we conclude that the chemical ages of the observed clouds are $10^5−10^7$ years. This estimate agrees with the ages of warm clouds derived from observations of other molecules, such as CH_3CCH [11].

4. CONCLUSION

Our survey of galactic star-forming regions in the 4−3 line of cyanoacetylene at 36.4 GHz has detected 17 sources.

The HC_3N abundances are $10^{-8}−10^{-10}$. These abundances suggest molecular-cloud ages of $10^5−10^7$ years.

ACKNOWLEDGMENTS

REFERENCES

1. B. E. Turner, Astrophys. J. **163**, L35 (1971).
2. C. M. Walmsley, G. Winnewisser, and F. Toelle, Astron. Astrophys. **81**, 245 (1980).
3. R. L. Snell, F. P. Schloerb, and J. S. Young, Astrophys. J. **244**, 45 (1981).
4. S. A. Kolotovkina, R. L. Sorochenko, and A. M. Tolmachev, Pis'ma Astron. Zh. **12**, 903 (1986) [Sov. Astron. Lett. **12**, 377 (1986)].
5. G. A. Blake, E. C. Sutton, C. R. Masson, and T. G. Phillips, Astrophys. J. **315**, 621 (1987).
6. J. Chernicharo, M. Guelin, and C. Kahane, Astron. Astrophys. **142**, 181 (2000).
7. M. Morris, R. L. Snell, and P. A. Vanden Bout, Astrophys. J. **216**, 738 (1977).
8. M. Morris, B. E. Turner, P. Palmer, and B. Zuckerman, Astrophys. J. **205**, 82 (1976).
9. P. Vanden Bout, R. B. Loren, R. L. Snell, and A. Wootten, Astrophys. J. **271**, 161 (1983).
10. E. A. Bergin, R. L. Snell, and P. F. Goldsmith, Astrophys. J. **460**, 343 (1996).
11. A. V. Alakoz, S. V. Kalenskiĭ, V. G. Promyslov, *et al.*, Astron. Zh. **79**, 610 (2002) [Astron. Rep. **46**, 551 (2002)].
12. J. Askne, B. Höglund, Å. Hjalmarson, and W. M. Irvine, Astron. Astrophys. **130**, 311 (1984).
13. C. Walker, A. Schulz, E. Krügel, and A. Gillespie, Astron. Astrophys. **205**, 243 (1988).
14. M. L. Kelly and G. H. Macdonald, Mon. Not. R. Astron. Soc. **282**, 401 (1996).
15. A. D. Haschick and W. A. Baan, Astrophys. J. **410**, 663 (1993).
16. G. Anglada, I. Sepúlveda, and J. F. Gómez, Astron. Astrophys. **121**, 255 (1997).
17. R. Bachiller and J. Cernicharo, Astron. Astrophys. **140**, 414 (1984).
18. J. S. Young, P. F. Goldsmith, W. D. Langer, *et al.*, Astrophys. J. **261**, 513 (1982).
19. A. Shulz, R. Güsten, R. Zylka, and E. Serabyn, Astron. Astrophys. **246**, 570 (1991).
20. P. R. Schwartz, J. H. Bologna, and J. A. Waak, Astrophys. J. **226**, 469 (1978).
21. C. Gwenlan, D. P. Ruffle, S. Viti, *et al.*, Astron. Astrophys. **354**, 1127 (2000).
22. M. S. El-Nawawy, D. A. Howe, and T. J. Millar, Mon. Not. R. Astron. Soc. **292**, 481 (1997).
23. D. P. Ruffle, T. W. Hartquist, S. D. Taylor, and D. A. Williams, Mon. Not. R. Astron. Soc. **291**, 235 (1997).

Translated by G. Rudnitskiĭ